Universität Rostock

Traditio et Innovatio

Electronic transport properties inside Earth and gas giant planets

Kumulative Dissertation
zur Erlangung des akademischen Grades
doctor rerum naturalium (Dr. rer. nat.)
der Mathematisch-Naturwissenschaftlichen Fakultät
der Universität Rostock

vorgelegt von
Uwe Kleinschmidt
geb. am 25. September 1997 in Anklam

Rostock, den 16.05.2025

https://doi.org/10.18453/rosdok_id00005672

Mathematisch-Naturwissenschaftliche Fakultät

Gutachter:

Prof. Dr. Ronald Redmer, Univ. Rostock, Institut Physik
Prof. Dr. Suxing Hu, Univ. of Rochester, USA

Jahr der Einreichung: 2025
Jahr der Verteidigung: 2025

Adresse: Universität Rostock
Institut für Physik
18059 Rostock
http://www.physik.uni-rostock.de

Abstract

Understanding the transport properties of light elements like hydrogen and heavy elements such as iron plays an important role in astrophysics in the dynamo processes in planets and stars. While the material properties of hydrogen and iron are very well known under normal conditions, they are mainly unknown under conditions in gas giant planets, stars, or even in the center of our Earth. This work investigates the electrical and thermal conductivity of hydrogen and iron under these extreme conditions using ab initio methods and analytical conductivity models. The behavior of the conductivity of solid iron under conditions of the Earth's core is calculated with ab initio simulations. These results can be used to get information about the internal dynamo processes. In the case of hydrogen, even more extreme temperatures and pressures are necessary to investigate the behavior of gas giant planets and stars. In this work, ab initio simulations are used to calculate the conductivity of hydrogen and to adapt the conductivity model of Lee & More to planetary conditions. Furthermore, the Lee & More model is used to calculate the conductivity in the thin outer layers of hot Jupiters with the help of mass action laws to investigate the influence of Ohmic heat.

Zusammenfassung

Das Verständnis der Transporteigenschaften von leichten Elementen wie Wasserstoff, aber auch schweren Elementen wie Eisen spielt eine wichtige Rolle in der Astrophysik bei den Dynamoprozessen in Planeten und Sternen. Während die Materialeigenschaften von Wasserstoff und Eisen unter Normalbedingungen sehr gut verstanden sind, sind diese unter Bedingungen in Gasriesen, Sternen oder selbst im Zentrum unserer Erde größtenteils unbekannt. Diese Arbeit beschäftigt sich mit der elektrischen und thermischen Leitfähigkeit von Wasserstoff und Eisen unter diesen extremen Bedingungen unter Verwendung von Ab-initio-Methoden und analytischen Leitfähigkeitsmodellen. Das Verhalten der Leitfähigkeit von festem Eisen wird unter Bedingungen des Erdkerns mit Ab-initio-Simulationen berechnet und kann genutzt werden um Rückschlüsse auf die inneren Dynamoprozesse zu erhalten. Im Falle von Wasserstoff sind noch extremere Druck- und Temperaturbedingungen notwendig um das Verhalten in Gasplaneten und Sternen zu untersuchen. In dieser Arbeit werden mit Ab-initio-Simulationen Leichtfähigkeiten für Wasserstoff berechnet und genutzt um das Leitfähigkeitsmodell von Lee & More für planetare Bedingungen anzupassen. Weiterhin wird mit diesem Modell unter Zuhilfenahme von Massenwirkungsgesetzen die Leitfähigkeit in den dünnen äußeren Schichten von heißen Jupitern berechnet, um den Einfluss von Ohm'scher Wärme zu untersuchen.

Contents

Chapter 1.

1 Introduction

Understanding the processes and the evolution in our Solar system and the universe is of great interest to astronomy and plasma physics. In recent decades, many studies about material properties in the Warm Dense Matter regime have increased our knowledge about astrophysical objects [1–12]. Also, the results from space missions, like Voyager and Cassini [13–19], and space telescopes, like Hubble, James-Web, and GAIA [20–22] help us to understand the objects in the universe and give us the possibility to benchmark theoretical results in a regime where no experiments are possible on Earth.
One big challenge in astrophysics is understanding the magnetic fields of planets and stars. Magnetic fields of stars can be measured with the spectropolarimetry method [23, 24], while direct measurement of planetary magnetic fields is impossible from Earth. Gravitational moments must be known to calculate the magnetic field of planets. With the help of space probes, the gravitational moments can be measured. Today, we know what the magnetic fields of the planets of our solar system look like [25] , but we have no exact knowledge about how these fields are generated. Magnetohydrodynamic (MDH) simulations help us understand the magnetic processes inside these planets [25–30]. In the case of rocky planets like our Earth, the most significant part of the magnetic field is generated in the core region caused by dynamo effects [29–31]. In gas giant planets like Jupiter and Saturn, where we expect no or just a diluted core, the magnetic field is mainly generated in the conductive layers of the atmosphere [27, 28]. A conductive material is needed to drive a dynamo [32]. Therefore, transport properties like electrical and thermal conductivity are essential in this research field. Over the last decades, many studies [4, 5, 33–44] have investigated the transport properties under planetary conditions, especially for the planets of our Solar system.
Iron is the main element of interest for the inner terrestrial planets because the core of these planets consists primarily of iron [45, 46]. The gas giant planets Jupiter and Saturn consist of hydrogen and helium, with minor contributions from metals [47]. The outer ice giants Uranus and Neptune consist of hydrogen, water, and methane mixtures [48]. Calculating and measuring material properties for these elements and mixtures, like the equation of state (EOS) [1] and transport properties [4, 5, 33], are essential to understand the internal structure, magnetic field generation, and thermal evolution of planets.
The elements of interest in this thesis are iron and hydrogen. Measuring material properties for these elements is very challenging under extreme conditions. The first experiments to measure conductivities in nonideal plasmas were done in the 70th by Ivanov *et al.* [49] for noble gases and air. In the mid-80s, Ichimaru and Tanaka [50] provided a conductivity model by solving the Ziman formula for arbitrary degeneracy in a quantum statistical approach. Meanwhile, Lee and More [51] provide a method for solving the Boltzmann equation in relaxation time approximation (RTA) for arbitrary degeneracy. They provide a complete set of transport coefficients for plasmas in electrical and magnetic fields. The whole formalism works for all possible ionization states and provides the known Spitzer limit of a Lorentz plasma [52, 53]. Desjarlais improved this approach in 2001, including electron-electron scattering and partial

ionization effects [54]. At the end of the 90th, the first experiments on the conductivity of warm dense hydrogen were conducted with gas guns [55, 56]. TThese experiments agree with later theoretical data from density functional theory. One example is the work of Holst *et al.* [8] , which provides conductivity data for warm dense hydrogen over a wide range of densities and temperatures in the conductive and non-conductive regions.
Nevertheless, it was recently shown that the Lee-More model deviates significantly from DFT-MD data in the WDM regime [10]. The existing conductivity data from DFT-MD, which agree well with the experiments, show the need for further improvements in the conductivity models for the conditions in WDM.
The electrical and thermal conductivity of iron under core conditions of rocky planets like our Earth is measured in experiments via diamond anvil cells (DACs). A considerable controversial discussion started in 2016 after two groups provided different conclusions over the thermal conductivity of iron in the Earth. The electrical conductivity measurements of Ohta *et al.* [36] and using the Wiedemann-Franz law [57] for metals to calculate the thermal conductivity do not agree with direct measurements by Konôpková *et al.* [35]. Whether a dynamo process like it is expected in the inner core is possible with lower thermal conductivity or not because of too high thermal conductivity, and how the dynamo in the Earth's core has developed in the past, cannot be solved with these two experiments. Furthermore, Pozzo *et al.* [40–42] provide theoretical results with DFT-MD that show deviations from both experiments. This leads to the need for further investigation from both the experimental and theoretical sides. Recently published results by Hasegawa *et al.* [38] provide quite promising results for the measured thermal conductivity in the range of theoretical predictions.

1.1 What is Warm Dense Matter?

The investigation of the behavior of matter under extreme conditions is a topic of primary interest in plasma physics, especially when classical models fail to describe strongly correlated matter. This region is called Warm Dense Matter (WDM) and represents dense plasmas up to solid-like or superionic states of matter [58–62]. Two important plasma parameters define the region of WDM. The first is the degeneracy parameter, which describes whether the plasma is classical or if quantum effects must be considered. It is given by

$$\Theta_s = \frac{2m_s k_B T}{\hbar^2}\left(\frac{g_s}{6\pi^2 n_s}\right)^{2/3} \gtrless 1 \begin{cases} \text{classical} \\ \text{degenerate} \end{cases}, \tag{1}$$

with the Boltzmann constant k_B and the reduced Planck constant $\hbar$. The mass, temperature, spin factor, and particle density are the quantities m_s, T, g_s, and n_s. Here, s denotes the sort of particle. Looking into a Fermi system of electrons, the spin factor $g_e = 2s_e + 1 = 2$. The parameter Θ_e compares the thermal energy $k_B T$ of the system to the Fermi energy E_F. It provides information about how strongly the system is degenerate and whether quantum effects have to be considered. For $k_B T >> E_F$, the degeneracy parameter is much greater than one. The system can be described classically because the high temperature broadens the edge of the Fermi distribution function. This broadening leads to occupation of high energy levels with only one electron. In the other case where $k_B T << E_F$, the system is strongly degenerate

because the energy distribution, described by the Fermi function, is not or only slightly broadened, and most of the energy states are occupied with two electrons. The system has to be described quantum mechanically (QM) now. As shown in Eq. (1), the system is defined as classical plasma if $\Theta_e > 1$ and degenerate if $\Theta_e < 1$. The second important plasma parameter is the coupling parameter

$$\Gamma_s = \frac{(Z_s e)^2}{4\pi\epsilon_0 k_B T}\left(\frac{4\pi n_s}{3}\right)^{1/3} \gtrless 1 \begin{cases} \text{strongly coupled (nonideal)} \\ \text{weakly coupled (ideal)} \end{cases}, \tag{2}$$

with the elementary charge e, the vacuum permittivity ϵ_0, and the charge of the particle Z_s. Assuming a hydrogen plasma leads to $Z = 1$ and $n_H = n_e$. The parameter Gamma describes how strongly the particles are coupled to each other, which means how strongly they interact with their neighbors. Therefore, the Coulomb energy E_C is compared to the thermal energy $k_B T$. In the same way as above, the system is defined as strongly or weakly coupled due to the values of Γ. If $\Gamma > 1$, the Coulomb force between the ions is stronger than the thermal energy, and nonideal effects must be considered. For the case that $\Gamma < 1$, the thermal energy overcomes the Coulomb forces, and the system becomes ideal due to weak coupling between the ions. For both parameters, the value of one decides whether additional effects (like QM or nonideal) have to be considered. The lines $\Theta_e = 1$ for electrons and $\Gamma = 1$ for the ions through the plasma plane are shown in Fig. 1. Here, the parameters for a hydrogen plasma are considered

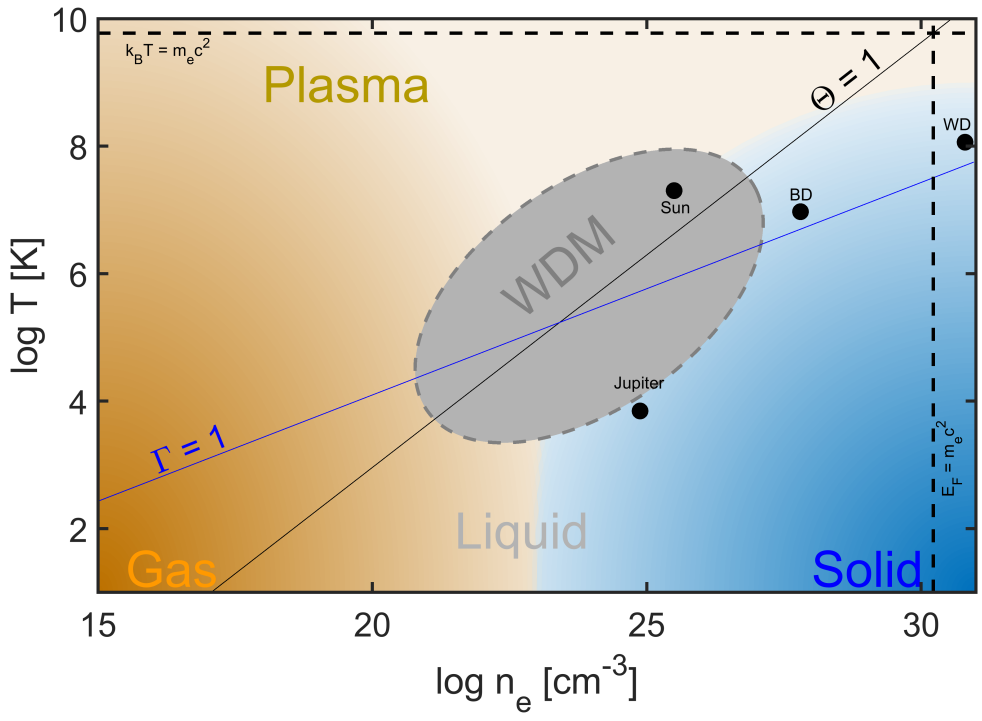

Figure 1: Plasma plane (density-temperature): Shown are the lines for $\Theta = 1$ (black) and $\Gamma = 1$ (blue), the regions were relativistic effects have to be taken into account (black dashed lines) and the conditions in the center of some astrophysical objects [63] (BD: Brown Dwarf, WD: White Dwarf). The region of Warm Dense Matter (WDM) is shown in grey.

($Z = 1$ and $n_H = n_e$). The region of WDM is defined around the region where both parameters are approximately one, where the matter has a high temperature but is too cold to neglect QM effects, and is so dense that the system is strongly coupled. The temperature region goes from

several thousand to millions of Kelvin at particle densities of 10^{21} to 10^{27} $1/\mathrm{cm}^3$. Even though the conditions are that extreme, they are still orders of magnitude away from the relativistic regions marked by the black dashed lines. The core conditions of some astrophysical objects, like our Sun or Jupiter, are also presented to show the importance of WDM for our understanding of astrophysics.
Calculating transport properties in WDM is one key to understanding the magnetic processes in astrophysical objects like gas giant planets, stars, and the centers of rocky planets. Therefore, understanding transport processes is very important.

1.2 Transport properties

As mentioned above, the transport properties in WDM are an important input parameter for MHD simulations to better understand the generation of magnetic fields in planets and stars [25–30]. The most common transport properties are the electrical conductivity σ and the thermal conductivity λ. Empirical relations of the current densities can define both quantities. Ohm's law defines the electrical conductivity:

$$\boldsymbol{j}_{el} = -\sigma \nabla \Phi, \tag{3}$$

where σ is the proportional constant between the electrical current density $\boldsymbol{j}_{el}$ and electric field $\boldsymbol{E} = -\nabla\Phi$. The thermal conductivity is defined similarly using Fourier's law:

$$\boldsymbol{j}_{Q} = -\lambda \nabla T, \tag{4}$$

where λ is the proportionality constant between the heat flux density $\boldsymbol{j}_Q$ and the temperature gradient ∇T. The investigation of these two transport properties for metals by Gustav Wiedemann and Rudolph Franz shows a constant electrical and thermal conductivity ratio. This ratio is described with the Wiedemann-Franz law [57]:

$$L = \left(\frac{e}{k_B}\right)^2 \frac{\lambda}{T\sigma}, \tag{5}$$

where L is the Lorenz number. In the Drude-Sommerfeld limit, the value of L is $\pi^2/3$ [64]. The thermal conductivity of this system can be calculated directly from the electrical conductivity and vice versa. However, this value for L is only correct for strongly degenerate systems, which is not accurate in the whole field of WDM. Therefore, both quantities have to be measured or calculated.
Measuring conductivities under extreme conditions, like in the WDM regime, is challenging due to the high temperatures and pressures. Standard methods are conductivity measurements in, e.g., diamond anvil cells (DACs) [35, 36] or gas guns [55, 56].
Theoretical approaches are based on transport theories of multicomponent systems, where each component contributes to the transport property due to scattering effects. The first theoretical approach to calculate transport properties was the kinetic theory. The central part of this theory is to solve the Boltzmann equation [65], which can be done using relaxation time approximation (RTA) [51] or with the Chapman-Enskog method [66]. Instead of solving the Boltzmann equation, it is also possible to use a quantum statistical approach by solving the

Ziman formula [67] as was done by Ichimaru and Tanaka [50]. Another way to calculate transport properties is using perturbation theory with Green's function or the description with a chemical picture. The particle densities of the multicomponent systems are calculated using mass action laws (MALs). The conductivity is then derived with linear response theory (LRT) [68, 69] using the Kubo theory [70] and the Zubarev formalism [71, 72]. With the growth of computing power and the development of high-performing supercomputers, new methods to calculate transport properties have emerged in recent decades. The most prominent one, which is also used in this work, is density functional theory (DFT) [73–77] combined with molecular dynamics (MDs) [78, 79] where a systems of several hundred up to thousand atoms is simulated over a few picoseconds. The central approximation in this method, due to the choice of the Exchange-Correlation-Functional (XC-Functional), is very well under control and tuneable for the underlying physical problem by using well-known reference systems, e.g., the uniform electron gas [80, 81].
The DFT-MD method is generally usable for any material, so many application areas exist. Regarding transport properties and MHD simulations, the investigation of warm dense hydrogen plasmas in stars and gas giant planets is just as possible as the simulation of metals like iron or nickel inside rocky planets like Earth.

1.3 Phase diagrams

Materials can change their structure on the lattice scale by increasing temperature and pressure. These changes can significantly influence the material properties, e.g., decide whether a material is conductive. A phase of a material is defined as a region where the system has no drastic changes in chemical and physical properties. The most commonly known phases of materials are the solid, liquid, gas, and plasma phases. Nevertheless, especially in the solid regime of a material, there can be several different structural phases with different properties. The existing phases of a material can be shown in the temperature-pressure plane as a phase diagram. In this thesis, the primary materials of interest are iron for the rocky planets and hydrogen for gas giant planets and stars.

1.3.1 Iron phase diagram

The iron phase diagram was intensely investigated in experiments and theory because iron makes up most of Earth's core. One example of the iron phase diagram is given in Fig. 2, proposed by S. Anzellini [82], with results from [83–90]. Under normal conditions, iron is a ferromagnetic metal in a body-centered cubic (bcc) structure. By increasing temperature, this structure goes through a phase transition into a paramagnetic face-centered cubic (fcc) phase and, for even higher temperatures, into a second bcc phase at ambient pressure. Increasing the pressure on iron at ambient temperature transforms the structure from the ferromagnetic bcc phase into a diamagnetic hexagonal close-packed (hcp) phase. This change in magnetism is the same for the liquid phase, where the transition from paramagnetic to diamagnetic takes place at pressures around 20-50 GPa [44]. Several studies proposed a third bcc phase under high temperature and pressure [86, 91] but were never verified by experiments. The most interesting phase for the interior of the Earth is the hcp phase for the inner solid core and the liquid phase for the outer liquid core. The differences in transport properties at the inner core boundary

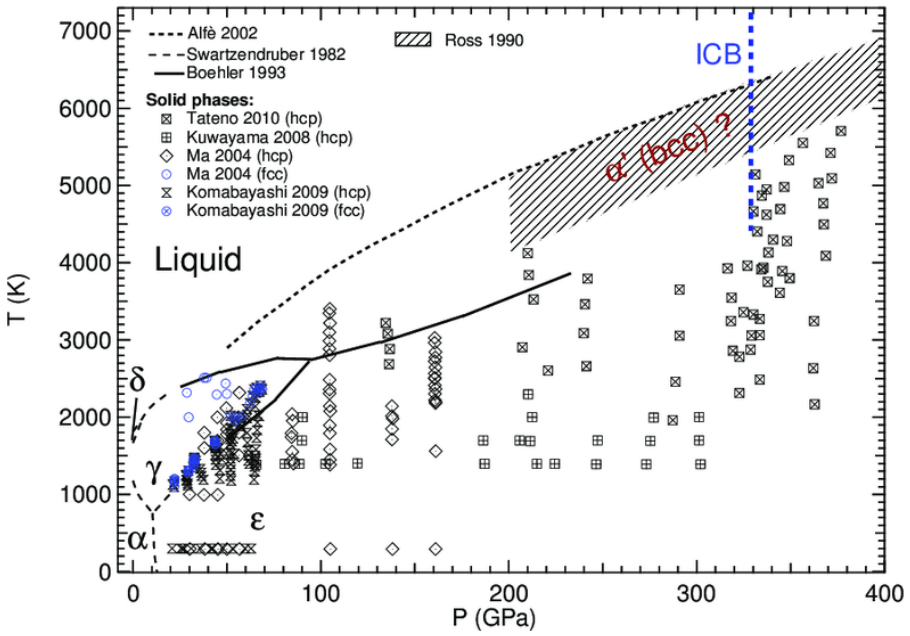

Figure 2: Iron phase diagram taken from S. Anzellini [82].

(ICB) of the liquid and solid phases are of great interest for understanding dynamo processes in the Earth's core. The conditions of 330 GPa and temperatures around 6000 K [34] are very challenging for experimental measurements. While a setup with DACs is used to provide high pressures [92], the heating in such experiments is done by direct laser heating [93]. The temperature of the sample is calculated from the measured black body radiation of the sample via a streak camera [35, 93]. While the pressure measurement with a well-known reference material is very exact [92], the temperature measurement is not that accurate. Temperature gradients in the sample due to the position of the sample in the laser focus induce nonequilibrium states and lead to temperature differences up to several hundred Kelvin between the center and the edge of the sample [82].

1.3.2 Hydrogen phase diagram

The phase diagram of hydrogen under extreme conditions is very complex and still a frequent topic in WDM. A current phase diagram is shown in Fig. 3 given by Gregoryanz *et al.* [94]. Shown are five solid phases based on results from experiments on solid hydrogen [95–99] and two fluid phases based on experiments with fluid deuterium [100, 101]. In the solid regime, hydrogen undergoes many structural transitions with pressure up to a solid metallic phase. The more interesting transition takes place in the liquid phase from the WDM point of view. The transition from a molecular non-conducting fluid to a metallic fluid occurs as a first-order phase transition at temperatures around 1000 K and pressures of 200-300 GPa. Above a critical point of roughly 1500 K, the transition is continuous. This transition plays an important role in generating a magnetic field in gas planets like Jupiter and Saturn and decides whether the magnetic field can be generated in these parts of the atmosphere [27, 28]. Magnetic fields can only be generated in conductive regions, making it necessary to know where the non-metal-to-metal transition occurs. The exact transition point was also investigated in

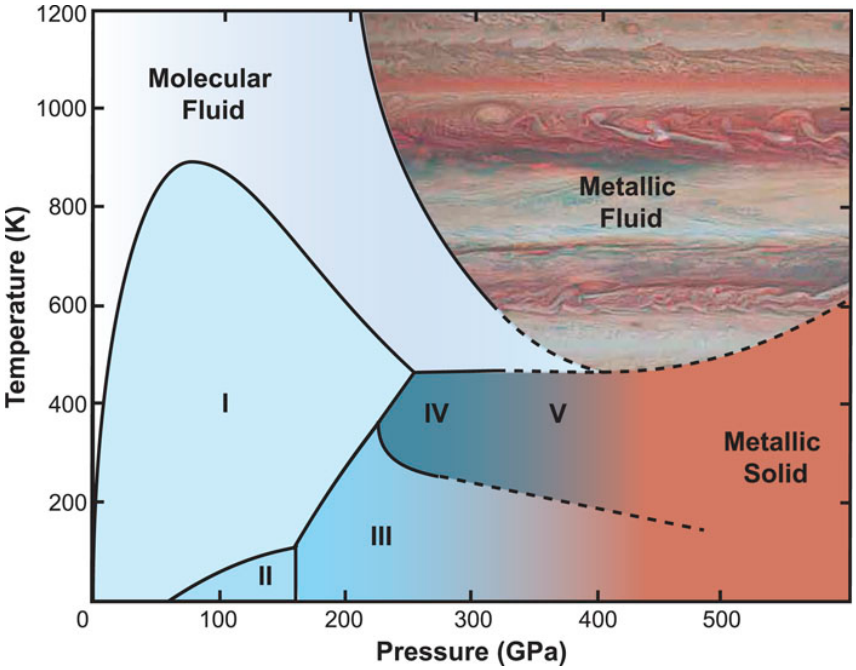

Figure 3: Hydrogen phase diagram taken from Gregoryanz *et al.* [94].

theory, recently with DFT-MD [102]. The possible existence of a conductive region in a gas planet can be extracted from DFT-MD results for hydrogen-helium mixtures, which are the main components of these planets along typical planetary profiles [4, 5].

1.4 Outline of this thesis

This cumulative thesis aims to give the reader a better understanding of transport properties in WDM and how these properties are calculated in practice. Especially, a wide range conductivity model for warm dense hydrogen is developed with the improvement of the Lee-More model [51] based on DFT-MD data. The original LM model is used to calculate conductivities of multicomponent systems in hot Jupiters. Further, the conductivities for iron under Earth's core conditions are calculated to clarify the controversial discussion about the thermal conductivity of iron under extreme conditions and the discrepancy between experiments and theory. Therefore, an understanding of transport theory and density functional theory is essential.
The thesis is structured as follows: Sec. 2.2 and Sec. 2.3 deal with density functional theory and molecular dynamics. The basics of the formalism of finite temperature density functional theory, the Kohn-Sham formalism, and the equation of motion in molecular dynamics are explained in more detail. Sec. 2.4 discusses the implementation of these algorithms in the program VASP (Vienna Ab initio Simulation Package). Sec. 2.5 describes the transport theories of linear response to calculate transport properties from density functional theory and relaxation time approximation to calculate transport properties from an analytical model as done by Lee and More [51]. Sec. 2.6 explains the theory of mass action laws to extract particle densities for the Lee-More model. Sec. 3 discusses the results, especially for iron under Earth's core conditions, hydrogen in WDM, and multicomponent systems in the outer atmosphere of hot Jupiters. Sec. 4 provides a final discussion of the main results and an outlook on possible

future developments. The publications used for this thesis are given in Chapter 5. Further papers [3, 103] were published but are not part of this thesis. In addition, the appendix provides convergence tests for the electrical conductivity of iron and hydrogen and the extrapolation of the new conductivity model to extremely high densities.

Chapter 2.

2 Theory

n quantum mechanics, a non-relativistic many-particle system is described by the wave function Ψ and a Hamiltonian or Hamilton operator $\hat{H}$. This Hamiltonian acts on the wave function described by the Schrödinger equation [104–107]

$$i\hbar\frac{\partial}{\partial t}\Psi(\boldsymbol{r},\boldsymbol{R},t) = \hat{H}\Psi(\boldsymbol{r},\boldsymbol{R},t), \tag{6}$$

where $\hbar$ is the reduced Planck constant, $\boldsymbol{r}$ describes the positions of the electrons, $\boldsymbol{R}$ describes the positions of the ions, and t is the time. In general, the wave function and the Hamilton operator are time-dependent. If the operator is time-independent, the equation (6) transforms into the stationary Schrödinger equation

$$\hat{H}\Psi(\boldsymbol{r},\boldsymbol{R}) = E\Psi(\boldsymbol{r},\boldsymbol{R}). \tag{7}$$

The Hamilton operator can be expressed as a sum of an ionic and electronic part describing the interaction of the particles in the system:

$$\hat{H} = \hat{H}_i + \hat{H}_e = \hat{T}_i + \hat{V}_{ii} + \hat{T}_e + \hat{V}_{ee} + \hat{V}_{ei}, \tag{8}$$

with the kinetic operators $\hat{T}_i$ and $\hat{T}_e$ for ions and electrons, and the potential operators $\hat{V}_{ii}$, $\hat{V}_{ee}$ and $\hat{V}_{ei}$ that describe the potential energy between ions and ions, electrons and electrons and electrons and ions. Analytically solving the Schrödinger equation is challenging and only possible for two particles. To solve this equation for more significant particle numbers, other approaches like Quantum-Monte-Carlo (QMC) [108, 109], density functional theory (DFT), coupled cluster theory, or configuration interaction method [110]. The method used in this work is DFT because it is very efficient and has relatively low computational costs.

2.1 Born-Oppenheimer approximation

The starting point to describe the many-particle system is the Born-Oppenheimer (BO) approximation [111]. This approximation decouples the ionic and electronic systems due to the assumption that the electrons are much lighter than the ions and move much faster. In other words, the electrons and ions move on different time scales. Electrons see fixed ion positions, while the ions see electrons that follow their movements instantaneously. The whole wave function can be written as a product of the ionic part Ψ_i and the electronic part Ψ_e

$$\Psi(\boldsymbol{r_i},\boldsymbol{R_j}) = \Psi_i(\boldsymbol{R_j})\Psi_e(\boldsymbol{r_i},\boldsymbol{R_j}), \tag{9}$$

where $\boldsymbol{r_i}$ and $\boldsymbol{R_j}$ are the electron and ion positions. Inserting Eq. (9) into the Schrödinger equation (7) leads to the following equations

$$\hat{H}_e\Psi_e(\boldsymbol{r_i},\boldsymbol{R}_j) = E(\boldsymbol{R_j})\Psi_e(\boldsymbol{r}_j,\boldsymbol{R}_i), \tag{10}$$

$$(\hat{H}_i + E(\boldsymbol{R_j}))\Psi_i(\boldsymbol{R}_j) = E\Psi_i(\boldsymbol{R}_i). \tag{11}$$

In this approximation, there is one component where the two systems are coupled. This component is the potential energy between electrons and ions $\hat{V}_{ei}$ in Eq. (8), where the electrons interact with fixed ions. That is why the electronic wave function is still dependent parametrically on the ion positions $\boldsymbol{R}$. The electronic and ionic systems are coupled with the Born-Oppenheimer energy surface $E(\boldsymbol{R}_j)$. The energy of the electron system can be calculated quantum mechanically using DFT, while the heavier ions can be moved classically in the charge field of the electrons with MD. In the following section, the idea of DFT-MD will be explained briefly. For a deeper look into this field, there are a lot of books and articles about DFT and MD [76, 77, 112–121].

2.2 Density Functional Theory

In this chapter, the basics of DFT will be discussed. The main idea of this approach is to solve the quantum mechanical problem for the electrons by going from the wave function that includes all positions $\boldsymbol{r}_i$ of the electrons to a charge density $n_e(\boldsymbol{r})$ that only depends on the location $\boldsymbol{r}$. This charge density is given by

$$n_e(\boldsymbol{r}) = N_e \int d^3r_2 ... d^3r_N |\Psi(\boldsymbol{r_1}, ..., \boldsymbol{r_N})|^2 \tag{12}$$

and is normalized to the electron number N_e

$$N_e = \int n_e(\boldsymbol{r}) d^3r. \tag{13}$$

The theory is based on the theorems of Hohenberg and Kohn [73]:

1. The external potential $V_{ext}(\boldsymbol{r})$ is (to within a constant) a unique functional of $n(\boldsymbol{r})$; since, in turn, $V_{ext}(\boldsymbol{r})$ fixes $\hat{H}$ we see that the full many particle ground state is a unique functional of $n(\boldsymbol{r})$.

2. The functional $E[n(\boldsymbol{r})]$ that delivers the ground state energy of the system delivers the lowest energy if and only if the input density is the true ground state density, $n_0(\boldsymbol{r})$.

The resulting energy functional can be written as

$$E[n(\boldsymbol{r})] = T_e[n(\boldsymbol{r})] + V_{ee}[n(\boldsymbol{r})] + V_{ei}[n(\boldsymbol{r})]. \tag{14}$$

Because the mapping of potential and density is unique, the minimum or ground state energy is directly connected to the ground state density. This results in a significant effort to solve the many-particle systems, but two big problems remain. First, the electron-electron interaction in the functional $V_{ee}[n(\boldsymbol{r})]$ is not precisely known, which leads to the fact that it is impossible to minimize the energy. Second, the current formalism describes systems at $T = 0$ K, but temperatures rise to thousands of Kelvin in the WDM regime. In the following, the Kohn-Sham formalism [74] developed in 1965 by Walter Kohn and Lu Jeu Sham to solve the interaction problem and the Mermin approach [75] to include temperature will be discussed.

2.2.1 Finite Temperature DFT and Kohn-Sham formalism

Kohn and Sham provided the practical formalism to solve DFT computationally by transforming the interacting system into a noninteracting system. All these end up in the widely known Kohn-Sham equations [74]. The formalism of finite temperature density functional theory (FT-DFT) will be explained in this section. Mermin included finite temperatures in DFT in 1965 [75]. In the case of finite temperature, the free energy F is minimized instead of the energy E. In thermodynamics, the free energy is calculated by

$$F_e(T, V, N_e) = U_e - TS_e, \tag{15}$$

where T is the temperature, V is the volume, U_e is the internal energy, and S_e is the entropy of the electron system. In the next step, a noninteracting system is introduced as a reference. The main idea behind this approach is that the reference system should provide the same electron density. The electron density in the Kohn-Sham (KS) reference system is defined as

$$n_e(\boldsymbol{r}) = \sum_{i=1}^{\infty} f(\epsilon_i)|\phi_i(\boldsymbol{r})|^2, \tag{16}$$

with the single-particle wave functions $\phi_i(\boldsymbol{r})$, also known as the Kohn-Sham orbitals and the weighting factors $f(\epsilon_i)$ which describe the occupation of the electrons via the Fermi-function. In a noninteracting system, the total wave function can be written as a Slater determinant of single-particle wave functions with the eigenenergies ϵ_i. The N noninteracting electrons are described with N individual noncorrelated single-particle Schrödinger equations. How these equations look will be discussed at the end of this section. The Fermi function is calculated via

$$f_i = \frac{1}{\exp\left(\frac{\epsilon_i - \mu_e}{k_B T}\right) + 1}, \tag{17}$$

where μ_e is the chemical potential and k_B is the Boltzmann constant. The free energy functional in the KS system can be written as

$$F[n(\boldsymbol{r})] = T_{KS}[n(\boldsymbol{r})] + J[n(\boldsymbol{r})] + E_{ei}[n(\boldsymbol{r})] - TS_{KS}[n(\boldsymbol{r})] + F_{XC}[n(\boldsymbol{r})], \tag{18}$$

with the kinetic energy T_{KS} and the entropy S_{KS} of the noninteracting system, the Hartree energy term J, the external energy E_{ei} and the exchange-correlation free energy term F_{XC} that describes the difference between the real system and the KS system, explicitly between T_e and T_{KS}, S and S_{KS} and corrections to the nonclassical part of V_{ee}. The kinetic energy of the KS system can be calculated with

$$T_{KS} = -\frac{\hbar^2}{2m_e} \sum_{i=1}^{\infty} f(\epsilon_i) \int d^3r \phi_i^*(\boldsymbol{r}) \nabla_i^2 \phi_i(\boldsymbol{r}). \tag{19}$$

The Fermi function is used to calculate the entropy via

$$S_{KS} = -k_B \sum_{i=1}^{\infty} [f(\epsilon_i) \ln(f(\epsilon_i)) + (1 - f(\epsilon_i)) \ln(1 - f(\epsilon_i))]. \tag{20}$$

The Hartree energy describes the Coulomb interaction between the electrons. It is given by

$$J[n(\boldsymbol{r})] = \frac{1}{2}\frac{e^2}{4\pi\epsilon_0}\iint d^3r d^3r' \frac{n(\boldsymbol{r})n(\boldsymbol{r'})}{|r-r'|}, \tag{21}$$

while the external energy term describes the Coulomb interaction with the field of the ions and is defined as

$$E_{ei}[n(\boldsymbol{r})] = -\sum_{j=1}^{N_i}\frac{Z_i e^2}{4\pi\epsilon_0}\int d^3r \frac{n(\boldsymbol{r})}{|\boldsymbol{r}-\boldsymbol{R_j}|}, \tag{22}$$

with the elementary charge e, the vacuum permittivity ϵ_0, and the charge number of the ions Z_i. The exchange-correlation free energy is defined as follows:

$$F_{XC}[n(\boldsymbol{r})] = (T_e[n(\boldsymbol{r})] - T_{KS}[n(\boldsymbol{r})]) + E_{ee}[n(\boldsymbol{r})] - J[n(\boldsymbol{r})] - T\left(S_e[n(\boldsymbol{r})] + S_{KS}[n(\boldsymbol{r})]\right). \tag{23}$$

The exact expression of the exchange-correlation functional is not known, which leads to the need for good approximations. In the next step, the Kohn-Sham equations are derived from the variational principle to find the wave functions that minimize the energy functional by using the normalization Eq. (13). This leads to an expression of an effective potential that acts on the noninteracting electrons. This effective potential $v_{eff}(\boldsymbol{r})$ is given by

$$v_{eff}(\boldsymbol{r}) = \frac{e^2}{4\pi\epsilon_0}\int d^3r' \frac{n(\boldsymbol{r'})}{|\boldsymbol{r}-\boldsymbol{r'}|} - \sum_{j=1}^{N_i}\frac{Z_i e^2}{4\pi\epsilon_0}\frac{n(\boldsymbol{r})}{|\boldsymbol{r}-\boldsymbol{R_j}|} + \frac{\delta F_{XC}[n(\boldsymbol{r})]}{\delta n(\boldsymbol{r'})} \tag{24}$$

and includes the Coulomb interactions between electrons and electrons, electrons and ions, and the variation of the exchange-correlation functional. The single-particle Kohn-Sham equations to find the eigenenergies ϵ_i are then given by

$$\left[-\frac{\hbar^2}{2m_e}\nabla^2 + v_{eff}(\boldsymbol{r})\right]\phi_i(\boldsymbol{r}) = \epsilon_i\phi_i(\boldsymbol{r}), \tag{25}$$

with the Kohn-Sham orbitals that define the electron density by Eq. (16). The three equations (16),(24), and (25) are solved self-consistently until the free energy (18) is minimized. This KS approach makes a computational calculation of DFT suitable if one finds a good approximation for the exchange-correlation functional. This theory is exact if all exchange and correlation effects are known and described in the XC-functional.

2.2.2 Exchange-correlation functional

The unknown variable in the whole formalism of KS-DFT is the exact exchange-correlation functional. Since the electron system's exact exchange and correlation effects are unknown, one needs good approximations to describe the main physical effects of exchange and correlation. Depending on the complexity of the system, many XC-functionals have been developed over the last decades [122–124]. Most of these functionals are based on ground-state DFT, which leads to the approximation $F_{XC} = E_{XC}$. The development of temperature-dependent XC-functionals [125–129] came up during the last years and were developed for FT-DFT in WDM. Nevertheless, the most used XC-functionals in the WDM regime, like PBE [122], SCAN [123], and HSE [124], are ground state approximations but provide reasonable agreement

with other computational methods and experiments [2, 3]. The different XC-functionals can be specified in different classes due to their complexity. They can be classified in a five-rung ladder ("Jacob's Ladder"). An overview can be found in the work of Perdew *et al.* [130]. On the ground stands the Hartree-Fock formalism, and the full chemical accuracy is on top.
The first rung describes the easiest way to approximate the exchange and correlation effects with the local-density approximation (LDA) given by

$$E_{XC}^{LDA}[n(\boldsymbol{r})] = \int d\boldsymbol{r} n(\boldsymbol{r}) \epsilon_{XC}[n(\boldsymbol{r})]. \tag{26}$$

The ϵ_{XC} describes the exchange and correlation effects per particle of a uniform electron gas. By including gradients or higher order derivatives of the electron density, inhomogeneities and deviation from the uniform electron gas are considered. The next higher order of XC-functionals is based on the generalized gradient approximation (GGA). Here, deviations from the electron gas are included by using the gradient $\nabla\rho$, which leads to the following expression:

$$E_{XC}^{GGA}[n(\boldsymbol{r})] = \int d\boldsymbol{r} n(\boldsymbol{r}) \epsilon_{XC}[n(\boldsymbol{r}), \nabla n(\boldsymbol{r})]. \tag{27}$$

In this work, the PBE functional [122], developed by Perdew, Burke, and Ernzerhof, is used to run the DFT simulations. The PBE functional

$$E_{XC}^{PBE}[n(\boldsymbol{r})] = E_{X}^{PBE}[n(\boldsymbol{r})] + E_{C}^{PBE}[n(\boldsymbol{r})] \tag{28}$$

calculates the exchange and correlation terms separately, as done in LDA by adding additional terms in the integral that include the electron density gradient. Including explicit dependence on the kinetic energy density leads to meta-GGA functionals. The most used candidate in WDM is the SCAN (Strongly Constrained and Appropriately Normed) functional [123]. To get one step further and include exact exchange from Hartree-Fock theory in a short distance, one can use the hybrid functional HSE (Heyd–Scuseria–Ernzerhof) [124]. This functional is designed to provide a better description of the band gap [131, 132]. The HSE functional describes, e.g., the liquid-liquid phase transition in hydrogen much more accurately as PBE [102]. Hybrid functionals, in general, include explicit dependence on occupied orbitals. A fully nonlocal XC-functional includes, in addition, the dependence on unoccupied orbitals. Nevertheless, more complex XC-functionals are computationally expensive and not always more accurate than more straightforward approaches [133].

2.2.3 Plane waves and pseudo potentials

There are many different DFT codes; some use plane wave sets, and other codes use local orbitals (like FHI-aims [134] or SIESTA [135]) to describe the Kohn-Sham orbitals. Plane-wave codes are ,e.g., Quantum Expresso [136], CASTEP [137], VASP [138–140], or Abinit [141]. In this work, the approach of plane waves is used in VASP, which will be explained in more detail now. The Kohn-Sham orbitals can be expanded as Bloch functions [142] in a periodic system

$$\Phi_i(\boldsymbol{r}, \boldsymbol{k}) = u_i(\boldsymbol{r}, \boldsymbol{k}) \exp(i\boldsymbol{r} \cdot \boldsymbol{k}), \tag{29}$$

where $u_i(\boldsymbol{r}, \boldsymbol{k})$ is the Bloch function. This function is periodic and can be expressed in the reciprocal lattice vector $\boldsymbol{G}$ dependence using the Bloch theorem [142]

$$\Phi_i(\boldsymbol{r}) = \frac{1}{\sqrt{V}} u_i(\boldsymbol{r}, \boldsymbol{k}) \exp(i\boldsymbol{r}\boldsymbol{k}) = \frac{1}{\sqrt{V}} \sum_{\boldsymbol{G}=0}^{\infty} C_i(\boldsymbol{G}, \boldsymbol{k}) \exp(i\boldsymbol{r}(\boldsymbol{k} + \boldsymbol{G})). \tag{30}$$

Here $C_i(\boldsymbol{G}, \boldsymbol{k})$ are Fourier expansion coefficients which have, in most cases, complex values [143, 144]. This expansion of the orbitals is beneficial, but in practice, it is unsuitable with a sum over all lattice vectors to infinity. Therefore, a predefined cutoff is set

$$E_{cut} > \frac{\hbar^2}{2m_e} |\boldsymbol{k} + \boldsymbol{G}|^2. \tag{31}$$

Normally, properties in the reciprocal space are extracted by integrating over the whole $\boldsymbol{k}$ space or at least the whole Brillouin zone. Nevertheless, it is possible to achieve good converged results using a weighted sum over a discrete set of $\boldsymbol{k}$ points [143, 144]. The Baldereschi mean value point [145] is often used in DFT-MD simulation to calculate EOS data. At the same time, a special scheme of Monkhorst-Pack sets [146] is used to calculate transport properties accurately [8, 147, 148].
Expanding the Kohn-Sham orbitals in plane waves with a specific cutoff is a good description for low oscillating wave functions, but not for the core region where the wave function strongly oscillates due to the diverging Coulomb potential. This leads to a description with more plane waves and a higher cutoff, drastically increasing computational time and costs. The solution to this problem is to use pseudopotentials [76]. The idea of this approach is that the inner electrons are closely bound to the core and have no influence on the chemical bonding, which is known as the frozen core approximation. These electrons form an effective potential around the core, which leads to a smoother wave function. The smooth wave function reduces the cutoff energy drastically. Projector Augmented-Wave (PAW) pseudopotentials are used, e.g., in VASP [149–151]. Many of these PAW potentials are already designed for different elements and different numbers of valence electrons and can be used in VASP.

2.3 Molecular Dynamics

Molecular dynamics (MD) simulations are a commonly used computational tool to calculate the behavior and trajectories of atoms and molecules [78, 79]. Several books give more details about the numerical description of MD [143, 152–154]. While the electronic system is solved, quantum mechanically, the ionic system is described classically with Newton's equation of motion

$$M_j \frac{d^2}{dt^2} \boldsymbol{R_j} = -\nabla_j E_{ii}(\boldsymbol{R_j}) - \nabla_j E_e(\boldsymbol{R_j}) - M_j \dot{\boldsymbol{R}}_j \frac{\dot{s}}{s}, \tag{32}$$

where the first term on the right side describes the Coulomb forces on the ions and the second term the forces on the ions from the background charge of the electrons. Therefore, the energy of the electron system is needed, which can be calculated with DFT, as mentioned before. The forces on the ions due to the electrons can be calculated via the Hellmann-Feynman theorem [155, 156]. The theorem says that the derivative of the energy with respect to the nuclei' coordinates provides the forces acting on the nuclei. The third term describes the forces on the ions from an external heat bath. This heat bath is coupled to the MD simulations to achieve a constant temperature. In this work, the Nosé-Hoover thermostat [157, 158] is used. The thermostat controls the temperature by holding the time-averaged kinetic energy constant.

2.4 DFT-MD simulation implemented in VASP

In the previous sections, the basics of DFT and MD were explained. This scheme is implemented in the Vienna Ab-initio Simulation Package (VASP) [138–140]. In the program, a set of plane waves and PAW potentials is used to develop the KS orbitals. The general workflow of a DFT-MD simulation is shown in Fig. 4. The work scheme starts with setting up the

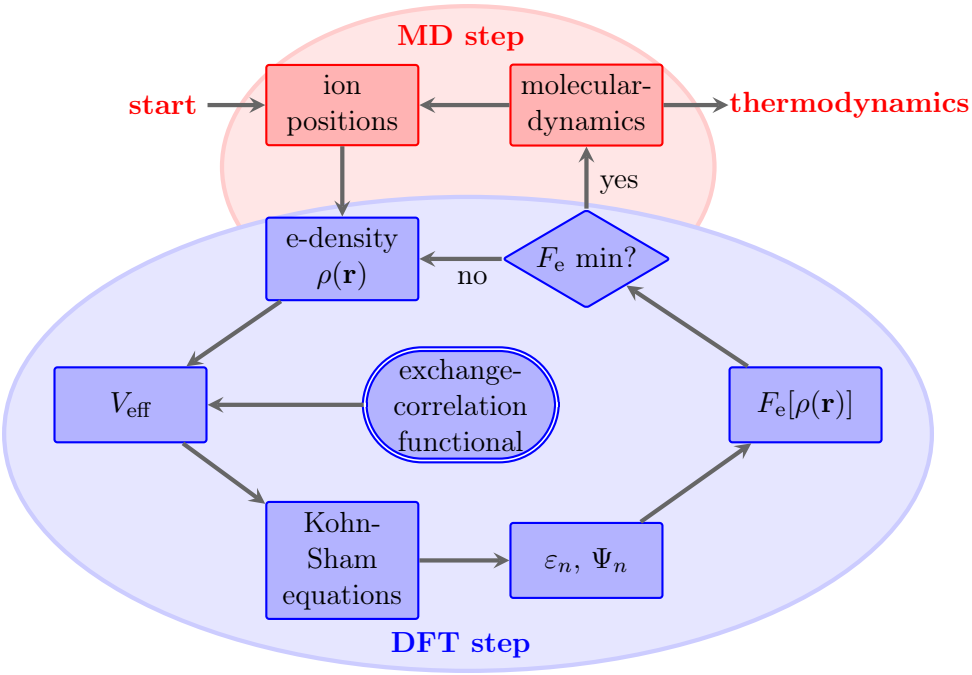

Figure 4: Workflow of DFT-MD simulations in VASP: The figure is taken from W. Lorenzen [159].

simulation box. There, the system's structure and density are given with the volume of the box and the total number of atoms inside. Periodic boundary conditions in the simulation neglect the effects on the edges of the box. A guessed electron density is taken for the given positions of the ions, and the effective potential is calculated using the given density and the XC-functional. This potential is used to solve the Kohn-Sham equations to get the eigenenergies and eigenfunctions, or Kohn-Sham orbitals. The orbitals define a new electron density and free energy. The same procedure is done for the new electron density until the free energy is minimized. In this case, minimized means that the difference to the free energy before is lower than a given threshold value (generally set to 10^{-4} or 10^{-5} eV). With the free energy of the electrons, the Hellmann-Feynman force on the ions is calculated, and the equation of motion for the ions is solved within the Verlet algorithm [152, 153]. After each MD step, thermodynamic properties like the system's energy and pressure can be extracted. Several convergence parameters have to be tested to get reasonable results. The most important ones are the number of particles in the box, the time step for the MD part to capture all physics on the right time scale, and the energy cutoff for expanding the plane waves as discussed in Sec. 2.2.3. Each parameter's convergence must be tested separately for every material considered in the simulation. This was done in this work for hydrogen and iron, as shown in the appendix.

2.5 Transport properties

As the introduction mentions, transport properties are proportionality constants and describe the movement or transfer of different quantities, such as matter, momentum, electrical charge, or energy, through a medium [160]. They can be calculated using kinetic theory by solving the Boltzmann equation [65] in relaxation time approximation (RTA) [51], using linear Response theory (LRT) [68, 161, 162] or the Zubarev formalism [71, 72]. Also, the quantum-statistical approach by solving the Ziman formula [67] by Ichimaru and Tanaka [50] provides reasonable results. For all theoretical models, it is important to include several limiting cases, e.g., the high-temperature plasma limit of Spitzer or Lorentz [53, 163] for weakly coupled systems and the low-temperature Ziman case [67] for dense plasmas.
While thermodynamic properties can be extracted directly from the simulations in VASP, additional steps must be used to extract transport properties like electrical and thermal conductivity. In the following parts, the linear response theory [68, 69, 164] for extracting conductivities from VASP and the relaxation time approximation [51] to find an analytical solution to the Boltzmann equation [65] will be discussed briefly.

2.5.1 Linear response theory (LRT)

As the name suggests, the linear response theory (LRT) describes a system's linear response due to a small perturbation from the outside. The transport equations are solved by disturbing the system gently and getting a linear response from the system [68]. This can be done for charge and heat transport. The solutions of these equations are dependent on the Onsager coefficients L_n [147], which are described by generalized Kubo-Greenwood formulas [70, 147, 165]:

$$\begin{aligned} L_n(\omega) =& \frac{2\pi(-1)^n}{V\omega} \sum_{\boldsymbol{k}\nu\mu} \mathrm{Re}(\langle \boldsymbol{k}\nu| \hat{\boldsymbol{v}} |\boldsymbol{k}\mu\rangle \otimes \langle \boldsymbol{k}\mu| \hat{\boldsymbol{v}} |\boldsymbol{k}\nu\rangle) \\ & \times (f_{\boldsymbol{k}\nu} - f_{\boldsymbol{k}\mu}) \left(\frac{E_{\boldsymbol{k}\mu} + E_{\boldsymbol{k}\nu}}{2} - h_e \right)^n \delta(E_{\boldsymbol{k}\mu} - E_{\boldsymbol{k}\nu} - \hbar\omega), \end{aligned} \tag{33}$$

with frequency ω, the reduced Planck constant $\hbar$, the volume of the simulation box V, the matrix elements $\langle \mathbf{k}\nu|\hat{\mathbf{v}}|\mathbf{k}\mu\rangle$ with the velocity operator $\hat{\mathbf{v}}$ and Bloch states $|\mathbf{k}\mu\rangle$, energy eigenvalue $E_{\mathbf{k}\mu}$, Fermi occupation number $f_{\mathbf{k}\mu}$ and the enthalpy per electron h_e. All these parameters can be extracted directly from the optical routines of VASP [9, 166]. The summation over $\boldsymbol{k}$ is a discrete sum over a given $\boldsymbol{k}$-point set. This additional convergence parameter must be tested for each material and condition. A more detailed look into LRT and the transport equations can be found in the habilitation thesis by Martin French [167]. By inserting the Onsager coefficients into the transport equations one can find that the dynamic electrical conductivity $\sigma_e(\omega)$ and the dynamic thermal conductivity of the electrons $\lambda_e(\omega)$ are directly connected to the Onsager coefficients (33) via

$$\sigma_e(\omega) = e^2 L_0(\omega), \tag{34}$$

$$\lambda_e(\omega) = \frac{1}{T} \left(L_2(\omega) - L_1(\omega) L_0^{-1}(\omega) L_1(\omega) \right), \tag{35}$$

where the coefficient $L_0(\omega)$ describes the original Kubo-Greenwood formula [70, 165]. This work calculates the DC (direct current) limits, taking the limit for $\omega \to 0$ with a linear extrapolation of the dynamic properties for small ω. In practice, the δ function is broadened by a Gaussian function. This broadening is another convergence parameter and should be small enough that the conductivity is independent of that parameter, but not too small so that the fluctuations in the dynamic conductivity are not too high, and a linear extrapolation is still possible.

2.5.2 Relaxation time approximation (RTA)

In practice, DFT-MD simulations can be computationally very challenging and time-consuming. That is why accurate conductivity models can save a lot of time. This part discusses the relaxation time approximation (RTA) by Lee and More [51] from 1984. They solved the Boltzmann transport equation [65], which describes the statistical behavior of the system, including force, diffusion, and collision terms in linear response. The main parameter in this formalism is the relaxation time, which describes how fast a system runs into equilibrium when perturbed. The relaxation time is closely related to the transport cross section. Lee and More got the following solution for the Onsager coefficients K_n [9, 51]:

$$K_n = -\frac{2m_e}{3\pi^2\hbar^3}\int_0^\infty dE \frac{E^{n+1}}{\sum_s n_s Q_{es}(E)}\frac{\partial f_e^0}{\partial E}, \tag{36}$$

with the transport cross-section $Q_{es}(E)$ and density n_s of the scattering partner s of the electrons and the derivative of the Fermi distribution f_e^0. The electrical and thermal conductivity calculation in the DC limit is done by the direct dependence on these Onsager coefficients, as before,

$$\sigma_e = e^2 K_0, \tag{37}$$

$$\lambda_e = \frac{1}{T}\left(K_2 - \frac{K_1^2}{K_0}\right). \tag{38}$$

Investigating an electron system that scatters on different scattering partners s, one can define the specific Onsager coefficient $K_{n,es}$ [9]:

$$K_{n,es} = -\frac{2m_e}{3\pi^2\hbar^3 n_s}\int_0^\infty dE \frac{E^{n+1}}{Q_{es}(E)}\frac{\partial f_e^0}{\partial E}, \tag{39}$$

which depends again on the transport cross section $Q_{es}(E)$, the density n_s and the derivative of the Fermi distribution f_e^0. The transport cross-section describes the probability of a scattering event at a given energy. Instead of using the transport cross-section, the Onsager coefficients can be defined with the relaxation time τ as follows [10]:

$$K_{n,es} = -\frac{2^{3/2}m_e^{1/2}}{3\pi^2\hbar^3}\int_0^\infty dE \frac{E^{n+3/2}}{\tau_{es}(E)}\frac{\partial f_e^0}{\partial E}. \tag{40}$$

The relaxation time is often expressed in Born approximation [9, 10, 168]

$$\tau(E) = \frac{2^{7/2}\pi\epsilon_0^2 m_e 1/2}{n_i Z_i e^4}\frac{E^{3/2}}{\ln\Lambda(E)}, \tag{41}$$

which considers only weak collisions. At the same time, the transport cross section is evaluated with a screened Coulomb potential where the key parameter is the screening parameter [169]. One can extract specific transport properties $\sigma_{e,s}$ and $\lambda_{e,s}$ by calculating the specific Onsager coefficients. In this work, the total conductivity of the system is calculated by

$$\frac{1}{\sigma_e} = \sum_s \frac{1}{\sigma_{e,s}}, \tag{42}$$

$$\frac{1}{\lambda_e} = \sum_s \frac{1}{\lambda_{e,s}}. \tag{43}$$

This approach for total conductivity values is known as the Matthiessen rule [170] and is widely known for the electrical conductivity. This ansatz for the thermal conductivity is motivated by theories from liquid mixtures [171] and an approach to include electron-electron scattering to DFT results [172]. In this work, results from DFT-MD simulation with LRT are used to define a relaxation time for strongly coupled matter in the case of hydrogen, and a chemical picture is used to extract particle densities of multicomponent systems to calculate transport properties in the outer atmosphere of hot gas giant planets in RTA.

2.6 Particle densities from Mass Action Laws

Knowledge of the number of scattering partners and their particle density n_i is important for scattering processes. The use of mass action laws (MALs) helps to calculate this. MALs describe the equilibrium position of a chemical reaction and can be written for non-interacting systems as [173]

$$\prod_i n_i^{\nu_i} = \prod_i \frac{(z_i^{int}(T))^{\nu_i}}{(\lambda_{th,i}^3)^{\nu_i}} = K(T), \tag{44}$$

where ν_i are the stoichiometric coefficients in the reaction, $\lambda_{th,i}$ is the thermal wavelength and z_i^{int} is the internal partition function of the particle i. $K(T)$ is the reaction constant and is derived from the total one-particle partition function

$$z_i(N_i, V, T) = z_i^{trans}(N_i, V, T)[z_i^{int}(T)]^{N_i} = \frac{V^{N_i}}{N_i! \lambda_{th,i}^{3N_i}}[z_i^{int}(T)]^{N_i}, \tag{45}$$

where Z_i^{trans} describes the translation effects and Z_i^{int} the internal modes. By assuming that the modes are independent of each other, the internal partition function can be written as [174]

$$z_i^{int}(T) = z_i^{nuc} z_i^{el} z_i^{vib} z_i^{rot}, \tag{46}$$

where z_i^{nuc} describes the nuclear, z_i^{el} the electronic, z_i^{vib} the vibrational and z_i^{rot} the rotational partition function. The nuclear partition function is calculated via

$$z_i^{nuc} = 2I_i^{ns} + 1, \tag{47}$$

where I_i^{ns} is the spin quantum number of the nucleus. The electronic part is given by

$$z_i^{el} = (2J + 1)\exp(-E_i^0/k_B T), \tag{48}$$

where E_i^0 is the ionization energy and J is the electronic angular momentum quantum number in the ground state. To consider molecules, one has to define the vibrational and rotational parts. In this work, only H_2 molecules are taken into account. One can use the high-temperature approximation and get the following results:

$$z_{H_2}^{vib} = \frac{1}{1 - \exp(-\theta_v/T)}, \tag{49}$$

$$z_{H_2}^{rot} = \frac{T}{2\theta_r}, \tag{50}$$

where $\theta_v = \hbar\omega/k_B$ is the vibrational and $\theta_r = \hbar^2/8\pi^2 I k_B$ is the rotational temperature. I is here the moment of inertia of the H_2 molecule. With the MALs, the number of free electrons in the system and the ionization degree are calculated. The ionization degree is given by

$$\alpha = \frac{n_e}{n_{total}}. \tag{51}$$

A monoatomic hydrogen plasma leads to the well-known Saha equation [175, 176] for temperature ionization:

$$\frac{n_{H^+} n_e}{n_H} = \frac{2}{\lambda_{th,e}^3} \exp\left(\frac{-\epsilon}{k_B T}\right), \tag{52}$$

with the ionization energy ϵ=13.6 eV of the hydrogen atom. Notice that the whole approach only holds for non-interacting systems, which is not the case in WDM, where matter is strongly correlated. Nevertheless, this approach can be used for the outer thin atmosphere of gas giant planets and as a low-density connection to the DFT-MD data.

Chapter 3.

3 Results

This chapter focuses on conductivity results from DFT-MD simulations and analytical models for solid iron under Earth's core conditions, hydrogen plasma in the region of WDM, and a multicomponent system of hydrogen, helium, and metals in the outer atmosphere of a hot Jupiter. The results presented here are published in peer-reviewed journals [177–179] and will be discussed so the reader will understand the relevant results.

3.1 Electrical and thermal conductivity of Iron in Earth's core

Transport properties like electrical and thermal conductivity of iron under extreme conditions, like in Earth's core, are heavily discussed because they play an important role in the evolution and stability of magnetic fields [29] as mentioned in the introduction. Many experimental and computational studies have been made to investigate the behavior of iron conductivity under those extreme conditions [34–37, 40–42, 180–182]. The differences in the results of the studies are significant, which makes further investigations necessary.
We investigate solid iron in two different phases, fcc (face-centered cubic) and hcp (hexagonal close-packed), between 9.0-13.55 g/cm^3 at temperatures from 1850 K up to 6350 K by using DFT-MD simulations and try to fit the data to simple formulas which were used to parameterize the conductivity for molybdenum [148]. First, we looked into the behavior along the different axes in hcp iron. Because this structure is isotropic in the x and y directions but not in the z direction, the geometry should affect the results along this axis. Figure 5 presents the electrical and thermal conductivity results for hcp iron along the axes. Results from the fit formulas [178] for the z direction and the basal plane (x-y plane) are also shown. The results

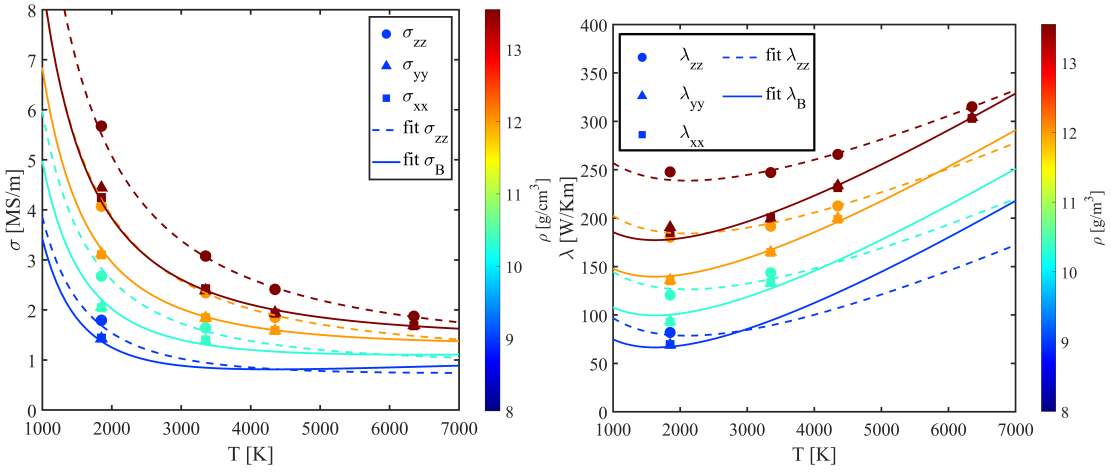

Figure 5: Conductivity anisotropy in hcp iron: left: Components of the electrical conductivity tensor, σ_{xx} (squares), σ_{yy} (triangles) and σ_{zz} (circles), for different temperature and densities from simulations with 288 atoms. Also shown are fits for σ_{zz} (dashed line) and σ_B (solid line). right: Components of the thermal conductivity tensor for hcp Fe, λ_{xx} (squares), λ_{yy} (triangles), and λ_{zz} (circles), for different temperatures and densities from simulations with 288 atoms. Also shown are fits for λ_{zz} (dashed line) and λ_B (solid line) [178].

are systematic for all three directions. While the electrical conductivity decreases with

temperature, the thermal conductivity increases. Higher densities lead to higher conductivity values in both cases due to higher electron density. We found a strong anisotropy due to the geometry by comparing the three directions. While the x and y components are nearly the same, the z component differs strongly and shows up to 30 % higher conductivity values. This effect was also investigated in experiments before [7, 180]. The effect is most substantial, especially for lower temperatures, where the crystal is nearly perfect. At higher temperatures, the atoms move increasingly, and the structure becomes more disordered until it melts. At this point, all components should be the same because there is no longer an anisotropy in the structure. As discussed in the introduction (Sec. 1.3), the typical phase in the Earth's core is the hcp phase, while fcc exists at much lower pressures. Nevertheless, we calculated the conductivities for the fcc structure to investigate the influence of structures and higher isotropy on the conductivity. Therefore, we take the average of the three hexagonal components and compare this value with the fcc conductivity. Fig. 6 shows the electrical and thermal conductivity results. By comparing the results for the two structures, one can see that the fcc

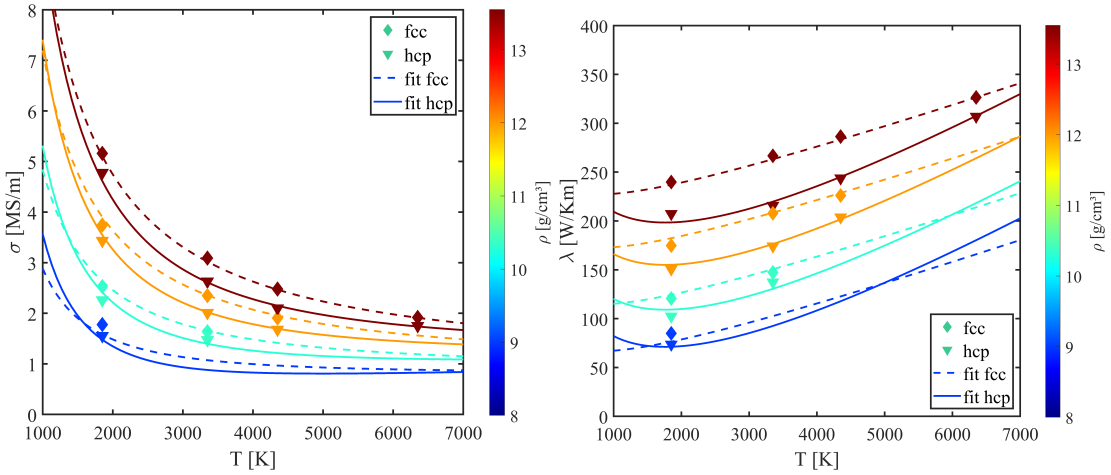

Figure 6: Conductivity comparison of fcc and hcp iron: left: Dependence of the electrical conductivity on temperature for given densities. Results for hcp Fe (triangles) are compared to those of the fcc phase (diamonds). Fits are shown as solid lines for hcp and dashed lines for fcc. right: Dependence of thermal conductivity on temperature for given densities. Results for hcp Fe (triangles) are compared to those of the fcc phase (diamonds). Fits are shown as solid lines for hcp and dashed lines for fcc [178].

conductivities are slightly higher than the hcp values but show the same behavior with temperature and density as described for the hcp components before. We also provide the results by fitting the results to a simple analytical formula. The agreement between calculated values and the fit is quite good, as we can predict conductivity values in between and compare these values to other computations and experimental results. First, we compare our hcp results for the electrical conductivity with experimental results. We translate our density-temperature points into pressure-temperature points by using the Birch-Murnaghan equation of state for hcp iron by Belonoshko [183] and plot our fit $\sigma(P,T)$ in comparison to the experiments by Zhang *et al.* [184], Ohta *et al.* [36], and a model by Gomi *et al.* [34] which is based on conductivity measurements at room temperature. The results are shown in Fig. 7. First, we find the same trends as in the experiments: the conductivity increases with pressure and decreases with temperature. The predictions of our fit in the lower pressure regime agree very well with the results by Zhang *et al.* [184] and Gomi *et al.* [34], while the experiments diverge

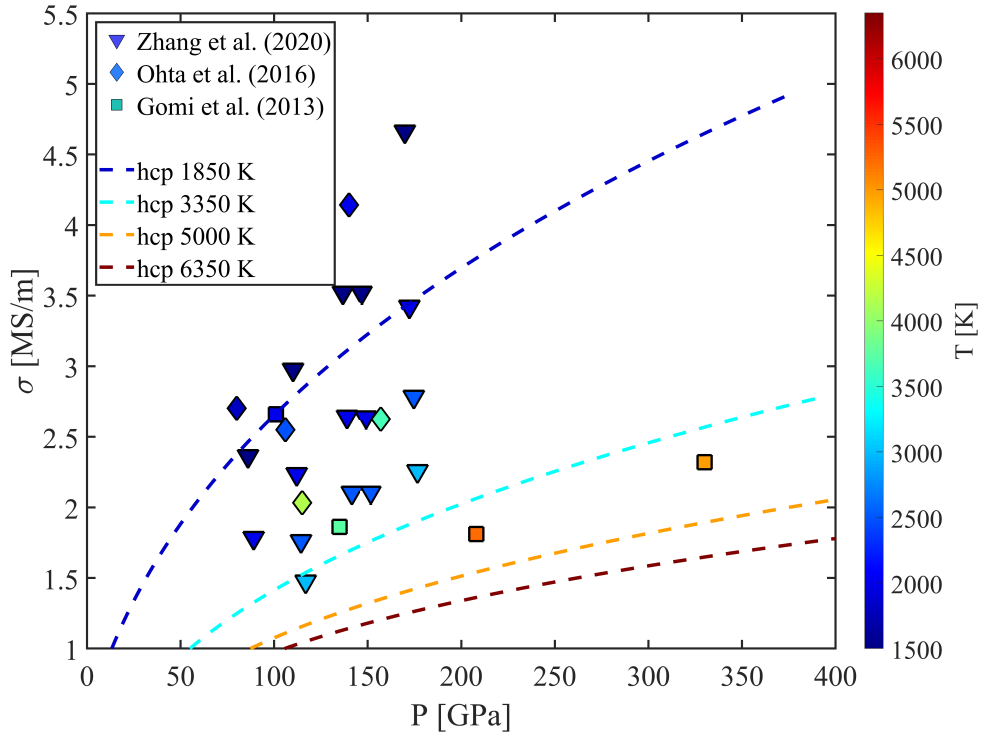

Figure 7: Electrical conductivity of hcp iron as a function of pressure for given temperatures. Our fit [178] is shown as dashed lines for four isotherms and compared to experimental data of Zhang *et al.* [184] (triangles), Ohta *et al.* [36] (diamonds), and Gomi *et al.* [34] (squares).

from our curves for higher pressures. The results by Ohta *et al.* [36] are significantly higher than our predictions over the entire P-T space. Lobanov and Geballe explain these deviations, especially the more substantial increase with pressure [185]. They suggest that the significant discrepancies between the experimental results may originate from P-induced changes in sample geometry. They reanalyzed the data by Ohta *et al.* [36] and Zhang *et al.* [184] and found that the discrepancy between the measurements decreases. This also influences the differences between the measurements and our results and brings them closer together.
We make the same comparison for thermal conductivity. We show our predictions of hcp iron compared to experiments by Konôpková *et al.* [35], Saha *et al.* [181] and Hasegawa *et al.* [37] in Fig. 8. We find a good overlap with the results by Saha *et al.* [181] for low pressures. Strangely, the experiment shows constant thermal conductivity over the entire pressure region. This is also shown in the results by Konôpková *et al.* [35], which are much lower than our predictions. The results by Hasegawa *et al.* [37] at one pressure condition are in the same region as the other two experiments. An increasing electrical conductivity and a decreasing thermal conductivity with pressure would lead to a pressure-dependent Lorenz number (see Eq. (5)). Due to the Wiedemann-Franz law [57], this Lorenz number should be a constant value for metals like iron when the electrons are strongly degenerate. This is the case for higher pressure, which makes a deviation from the Wiedemann-Franz law unphysical and the results of the thermal conductivity measurement more questionable. Recent measurements [38] of the thermal conductivity have shown much better agreement with theoretical results and show a clear trend for increasing thermal conductivity with pressure. The new results and the reanalyzed electrical conductivity data show a clear trend that the significant deviation in former experiments and theoretical results will become much closer with increasing computer

power and new experimental setups.

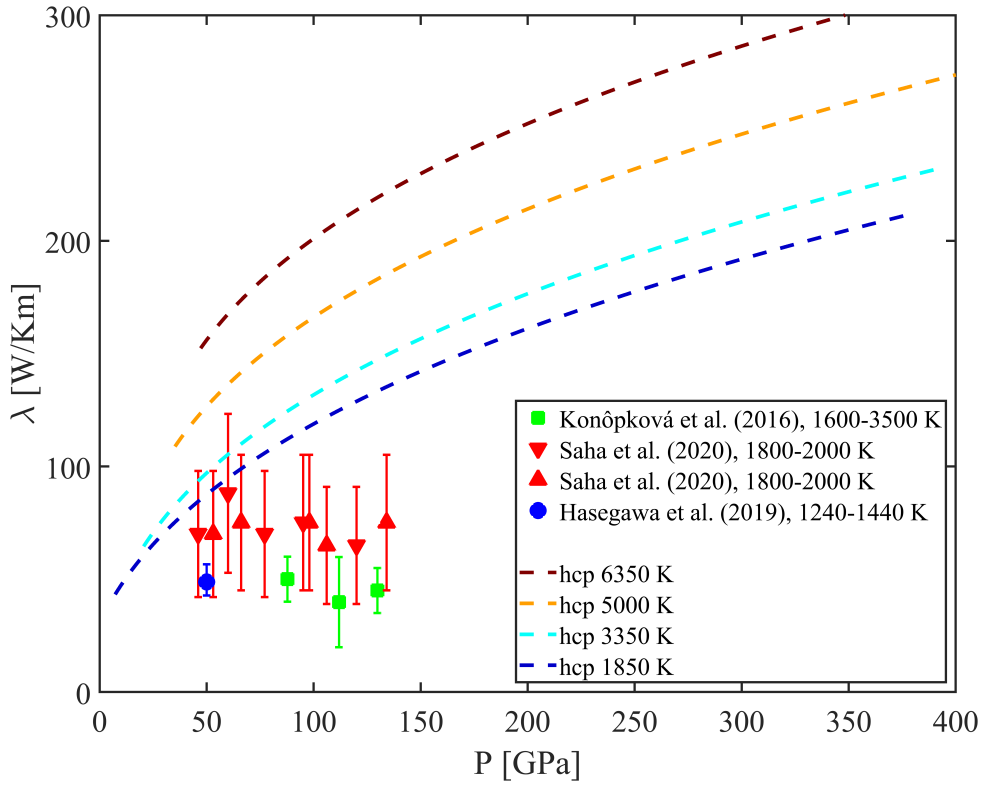

Figure 8: Thermal conductivity of hcp iron as a function of pressure: Experimental data from Konôpková *et al.* [35] (green squares), Saha *et al.* [181] (red triangles: upward for pressure transmitting medium NaCl and downward for pressure transmitting medium Al_2O_3), and Hasegawa *et al.* [37] (blue circle) are compared to the fit of our DFT-MD results for hcp iron evaluated along four isotherms [178].

3.2 Conductivity modeling for warm dense hydrogen

The importance of good conductivity data for hydrogen under extreme conditions is very high. Hydrogen is the most abounded element in our universe, and the investigation of hydrogen in WDM or hot dense matter is important for planetary physics [186], stellar physics [6], and the field of inertial confinement fusion (ICF) [1, 187, 188]. During the last decades, many studies on hydrogen or hydrogen mixtures have been published [1–6, 8–11, 55, 56, 189] from the experimental and theoretical side. Many results from ab initio methods like DFT-MD exist for various temperatures and densities. However, no analytical model has captured the result from these calculations. One example is the famous Lee-More model [51] from 1984. The Boltzmann equation is solved in relaxation time approximation (RTA) as mentioned in Sec. 2.5.2. It was shown that the differences between DFT-MD and this Lee-More model are significant also if one includes degeneracy in the model [10]. The main problem is to find the right relaxation time in this analytical model. Usually, the relaxation time is calculated in the Born approximation [9, 10, 168], which leads to this big difference. In our work, we used a new ansatz for the relaxation time

$$\tau_{eI}(E) = \frac{E^{3/2} P(T, \rho_I)}{n_I Z_I^2}, \tag{53}$$

where the dependence on the energy E, the particle density of the ions n_I, and the charge of the ions Z_I, is the same as in the Born approximation. The new fitting parameter $P(T, \rho_I)$ is used to tune the model on our DFT-MD data set. This leads to the new expression of Eq.(40):

$$K_{n,eI} = -\frac{2^{3/2} m_e^{1/2} P(T, \rho_I)}{3\pi^2 \hbar^3 n_I Z_I^2} \int_0^\infty dE\, E^{n+3} \frac{\partial f_e^0}{\partial E}. \tag{54}$$

If the hydrogen plasma is partially ionized, additional scattering processes on atoms or molecules can occur. Here, we only investigate the regime where the plasma mainly consists of electrons, ions, and atoms. Therefore, we added the electron-atom scattering as provided by French and Redmer [9] for water plasmas:

$$K_{n,eN} = \frac{2^{11/2} \pi^{1/2} (n+3)! \epsilon_0^2 (k_B T)^{n+3/2} n_e}{3 e^4 m_e^{1/2} n_N \sum_i Z_{N,i}^2 \ln AN, i(x_{n,N,i})}. \tag{55}$$

All parameters in this equation are taken from their work. To define the amount of scattering partners, we built an analytical fit formula to calculate the plasma ionization degree α. A detailed explanation of the methods to extract $P(T, \rho_I)$ and α can be found in the publication [179] in Sec. 5.

The main result of our work is shown in Fig. 9. We calculated conductivities for densities from 0.1 g/cm^3 up to 8 g/cm^3 and temperatures from 2000 K to 500000 K with up to more than 1000 atoms in the simulation box. With this data set and the high-temperature limit of the Lee-More model that describes the correct limit of a Lorentz plasma [53], we fit $P(T, \rho_i)$ and α in a way that describes fully and partially ionized hydrogen plasmas very accurately. The solid lines in the two figures show results from our new model, and the points are the accurate DFT-MD data set. The agreement is significantly better than the former comparisons between DFT-MD and analytical models. In most regions of our data set, the deviation of DFT-MD data and model is less than 10 %. Our model deviates only for very low densities and

temperatures. This is because we neglect molecules as scattering partners, which are important under those conditions. Further, we compare our model with high-density calculation from

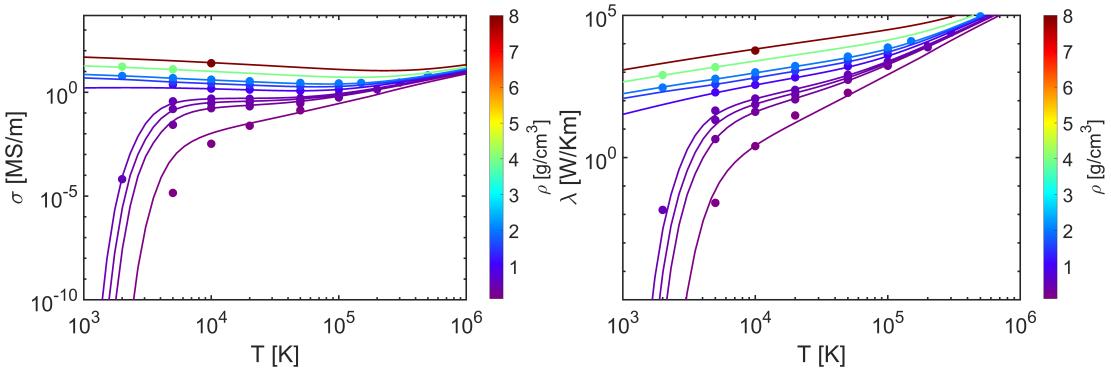

Figure 9: Conductivity in partially ionized hydrogen plasma: left: Electrical conductivity as a function of temperature and density (color coded). The direct results from DFT simulations are shown with dots, and the conductivity model is displayed with lines. right: Thermal conductivity as a function of temperature and density (color coded). The direct results from DFT simulations are shown with dots, and the conductivity model is displayed with lines [179].

Lambert *et al.* [189] in Fig. 10 and find good agreement for the lowest density of 10 g/cm^3 but more substantial deviation for the high densities at lower temperatures, which leads to the method of finding the limit $\omega \to 0$ for the dynamical conductivity in Eq. (34) where we used a linear fit instead of a Drude-like behavior and the accuracy of our model for very high densities. The results using a Drude fit are always slightly lower than our method, and our model overestimates the conductivity value in the high-density, low-temperature regime (see App. B). Nevertheless, we are confident in our model for higher densities at higher temperatures and find the correct high-temperature limit from the Lee-More model for all densities. Another approach

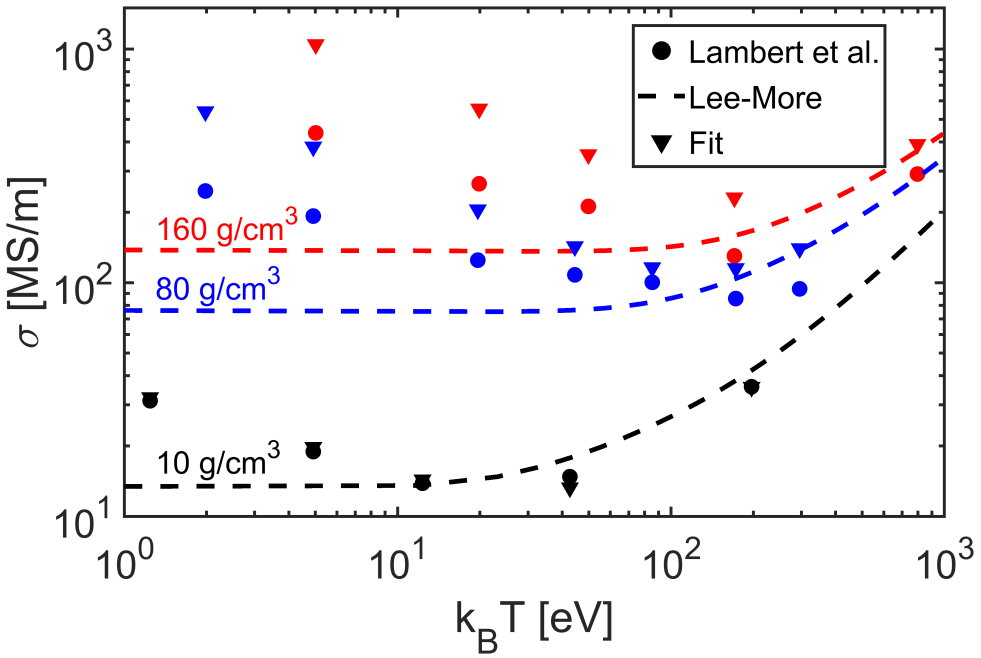

Figure 10: Electrical conductivity as a function of temperature for three different densities from our model [179] (triangles) in comparison to results of Lambert *et al.* [189] (dots) and the Lee-More model [10, 51] (dashed lines).

to calculating conductivities in the high-temperature and low-density limit for DFT-MD is the

virial expansion by Röpke *et al.* [168, 190]. The high-temperature limit is shown in Fig. 11. Again, we see a perfect agreement regarding high-temperature DFT-MD-based results with the

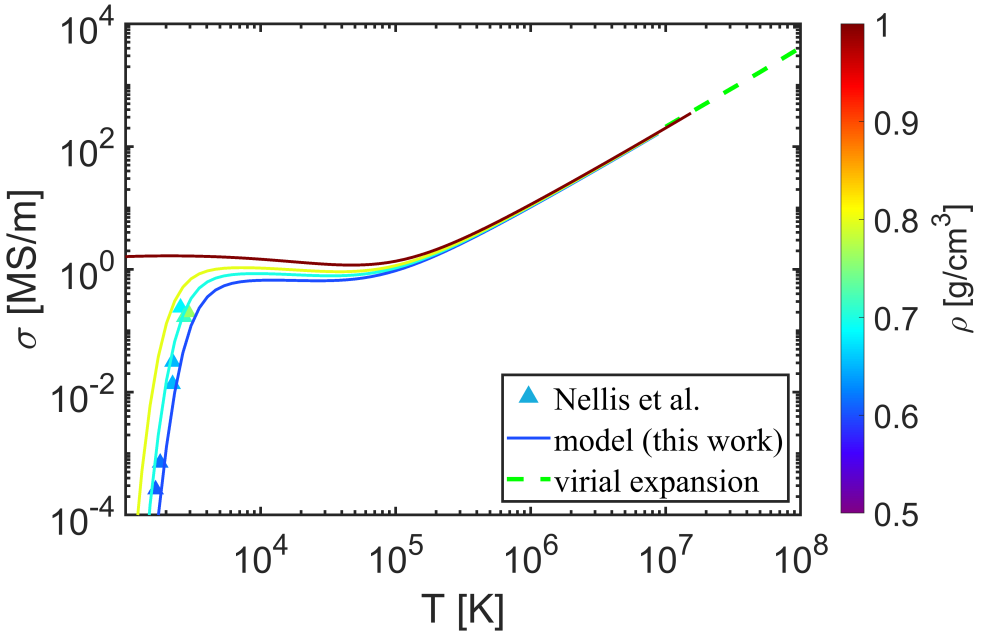

Figure 11: Comparison of the electrical conductivity from our model [179] (color-coded lines) to the gas-gun experiment of Weir *et al.* [55] and Nellis *et al.* [56] (symbols), and the virial expansion of Röpke and co-workers [168, 190] for 1 g/cm^3 (green dashed line).

virial expansion. Also shown are experimental results from gas gun experiments from Nellis *et al.* [56] and Weir *et al.* [55]. The agreement in the electrical conductivity for the given densities and temperatures is excellent. Our DFT-MD-based model could also agree reasonably well with the general trends from average atom models [191] and show perfect agreement for dense hydrogen [179]. This agreement was also shown by several review papers [2, 3]. All the results show that we developed a conductivity model for hydrogen plasmas in the warm dense matter regime that provides reasonably good results over a wide range of densities and temperatures, and leaves open space for improvements to include new scattering processes or fine-tuning for more extreme conditions, like in inertial confinement fusion.

3.3 Conductivities in the outer part of hot gas giant planets

Investigating conductivity for plasmas in the outer part of hot Jupiters is important to understand dynamo effects and Ohmic heating mechanisms in these planets [25–28, 192, 193]. Running DFT-MD simulations under those conditions is not efficient because the interactions of the particles are so weak that the simulation would run nearly forever to get into equilibrium. Instead, we use MALs to extract particle densities and calculate conductivity with the Lee-More model [10, 51] as described in Sec. 2.5. We investigate the first observed exoplanet HD 209458b [194] and calculate the transport properties for four planetary models shown in

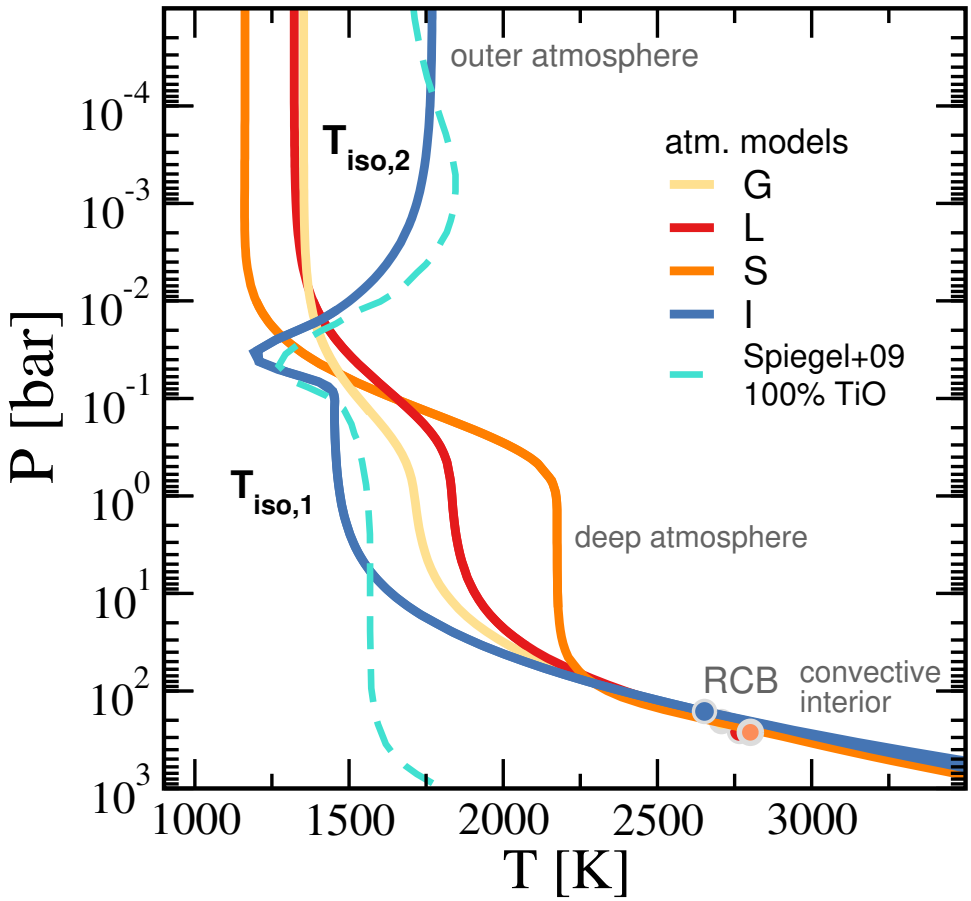

Figure 12: Pressure-temperature profiles of the atmosphere of HD 209458b. Shown are the four atmospheric models used in this work [177], three without an inversion, namely, G (yellow), L (red), and S (orange), and one with an inversion in the temperature, I (blue), located at about 0.03 bar. Further features of the models are displayed: the location of the radiative-convective boundary, the onset of the convective interior, and the characteristic temperatures $T_{iso,1}$ and $T_{iso,2}$.

to pressure-temperature profiles following the approach by Poser *et al.* [195]. Model G is based on the globally averaged theoretical $P - T$ curve by Guillot [196]. The second model, L, reproduces the results by Line *et al.* [197]. Both models show a similar profile. The two models, S and I, follow the suggestions by Spiegel *et al.* [198] where model S has higher temperatures in the range of 0.3 to 100 bar while model I is pretty similar to the original profile of Spiegel *et al.* [198]. Going deeper into the atmosphere, we connect our atmosphere profiles to an adiabatic interior model at the pressure level where the atmospheric temperature gradient matches the adiabatic gradient. The points are marked with circles in the plot. Fig. 13 shows the resulting

transport properties along the profiles. The results for α and the electrical conductivity are closely related because σ_e depends on the total amount of free electrons, which is described by the ionization degree α. The thermal conductivity shows similar trends but minor variations along the profiles. This is because we consider additional terms to the electric part, namely the translational motion of neutral particles and the dissociation and ionization of molecules and atoms in these regions. The results show clearly that the choice of the profile can cause significant differences in the results by three orders of magnitude at the same pressure. This also influences the effect of Ohmic dissipation or Ohmic heating. This process is directly correlated to the electrical conductivity. With our results, Ohmic heating would be too inefficient to explain hot Jupiter inflation due to its low electrical conductivity. Nevertheless, newer internal models suggest much higher temperatures in the atmosphere of HD 209458b [197], leading to a higher ionization degree and electrical conductivity. That would make the effect of Ohmic heating possible. The results show that besides good conductivity models, the presence of good planetary models is significant. If both components are at the highest level of our knowledge, we can make reasonable predictions for these complex systems. More details about building up a planetary profile and how the electrical conductivity and magnetic fields influence the Ohmic heating can be found in many research articles [13, 14, 25–28, 192, 193, 195, 199].

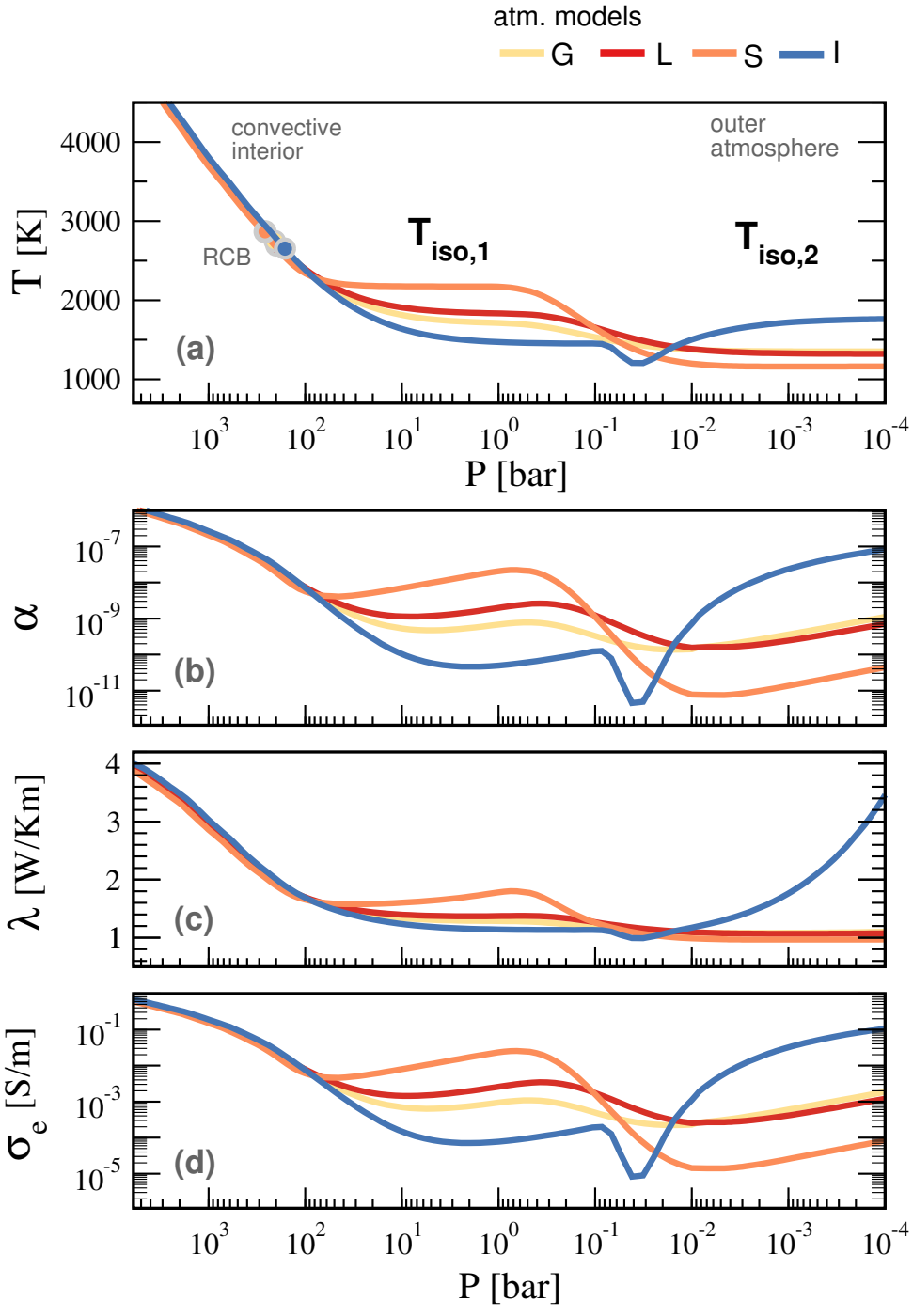

Figure 13: Temperature T, ionization degree α, thermal conductivity λ, and electrical conductivity σ_e for different planetary interior models along the pressure axis of HD 209458b, specifically, for the four atmospheric models used in this work [177]: G (yellow), L (red), S (orange), and one with an inversion, I (blue). Circles in the temperature profile represent the location of the radiative-convective boundary.

Chapter 4.

4 Discussion and Outlook

This work has shown the importance of conductivity in the WDM regime and the great advantage of DFT as a theoretical method for describing these conditions. It provides important benchmarks for future experiments and gives simple fit formulas for iron's conductivity and a wide-range model for hydrogen, which can be used for conditions in gas planets, brown dwarfs, and stars.
The iron results show that the electrical conductivity experiments agree well over a wide range with our theoretical predictions, mainly if one includes the dependence on geometric changes in the sample during the experiments [185]. However, the disagreement in the thermal conductivity between theory and experiment is substantial. This indicates problems in the experimental setup because the experiments diverge from the Wiedemann-Franz law, which should not be the case under these conditions. The difference can be caused by problems in the temperature measurement or geometric changes in the sample, as was found for the electrical conductivity measurements. Recent measurements [38] agree much better with our theoretical predictions and show a good trend to overcome the discrepancy between experimental and theoretical results.
Nevertheless, there is still much potential for future work. We can use our predictions and the new measurements as a benchmark to test new experimental setups or theoretical approaches. We can use the growing computer power to go beyond the current status by increasing, e.g., particle numbers in the simulations, or go to much more extreme conditions like in the center of super-Earths. This work also provides simple fit formulas for the conductivities that can be used in the future to calculate results along a core profile of the Earth, which is important for MHD simulations.
Furthermore, the structural influence on the conductivity was investigated, and it was shown that the more isotropic fcc structure provides higher conductivity results than the hcp structure. Also, the components in hcp iron show an anisotropy effect where the component in the z-direction is up to 30 % higher.
The results for hydrogen in the WDM regime from DFT-MD simulations in this work provide an extensive data set over a wide density-temperature range. This data set was used to modify the relaxation time in the Lee-More model to include stronger correlations in the plasma. The modified model shows excellent agreement over a wide range of temperatures and densities with the DFT-MD results and other theoretical results, like average atom models [2, 3, 191] or the viral expansion [168, 190]. The agreement with experiments on the gas gun [55, 56] is also excellent. Nevertheless, there are still some discrepancies for very dense and relatively cold hydrogen plasmas between our model and DFT-MD calculations [189]. This leaves space for future improvements by performing DFT-MD simulations for very dense hydrogen and renewing the fit formula from this work, or building a new fit formula for very dense hydrogen plasmas. This method would also be beneficial in the region of ICF by redoing this formalism with, e.g., deuterium and tritium. In the end, we can claim that our modified Lee-More model for partially and fully ionized hydrogen plasmas can be used to calculate conductivities inside

gas giant planets, brown dwarfs, the envelopes of stars, or the regime of confinement fusion with further improvements. In the future, it would be necessary to investigate more complex systems like hydrogen-helium mixtures or the burning material in ICF capsules. Therefore, modifying the Lee-More model for helium or any other material of interest in combination with our model could calculate the conductivities of the mixture.
In the region of less dense and hot plasmas, we used the original Lee-More model to calculate the conductivity of a multi-component system in the outer atmosphere of a hot Jupiter with the help of mass action laws. Therefore, several planetary profiles are used to calculate the conductivities along these parts. It is shown that temperature differences in the profiles can cause significant differences in the electrical conductivity and minor differences in the thermal conductivity. This is because the electrical conductivity is directly proportional to the ionization degree, while the thermal conductivity has, besides the electrical part, a translational and dissociation part. Nevertheless, the results for all profiles provide conductivities that are too low to explain the effect of Ohmic heating and can not explain the bigger radius of hot Jupiters. Newer planetary profiles suggest much higher atmospheric temperatures [197], which leads to higher conductivity and the possibility of making Ohmic heating possible. This work has shown that, besides an accurate conductivity model, which is validated in the underlying condition, very accurate atmospheric profiles of the planets are needed because minor differences can cause drastic changes in the ionization degree and, therefore, in conductivity.
To conclude, this work provides substantial effort in calculating transport properties in WDM. The results provide a new benchmark, and the given fit formulas and models can be used to calculate conductivities along planetary profiles as an input for MHD simulations. The formalisms in this work have shown that we can use DFT-MD data to modify analytical models or find fit formulas that can explain the behaviour of the conductivity inside planets. With this knowledge, it is possible to use these formalisms for other transport properties and increase the field of application to even more extreme conditions.

Chapter 5.

5 Publication

This section shows the first author and co-author papers [177–179]. For each publication, a detailed overview with the title, the author list, and their contributions are provided. Notice that two other papers [3, 103] were published but are not part of these cumulative thesis.

5.1 Ionization and transport in partially ionized multicomponent plasmas: Application to atmospheres of hot Jupiters

Author contributions

S. Kumar: Preparation of the manuscript, further development of the code for the transport properties, analysis and interpretation of the results

A. J. Poser: Preparation of the manuscript, calculation of the athmospheric thermal profiles of HD 209458b and of the coupled atmospheric, interior, and thermal evolution data, analysis and interpretation of the results

M. Schöttler: Development of the initial code for the transport properties

U. Kleinschmidt: Application and first benchmarking of the initial code for the transport properties, investigating the manuscript

W. Dietrich: Preparation of the manuscript, analysis of the planetary magnetic field and induction process, interpretation of the results

J. Wicht: Supervision of the project, analysis of the planetary magnetic field and induction process, preparation of the manuscript

M. French: Supervision of the project, preparation of the manuscript

R. Redmer: Supervision of the project, preparation of the manuscript

Ionization and transport in partially ionized multicomponent plasmas: Application to atmospheres of hot Jupiters

Sandeep Kumar,[1,*] Anna Julia Poser,[1] Manuel Schöttler,[1] Uwe Kleinschmidt,[1] Wieland Dietrich,[2] Johannes Wicht,[2] Martin French,[1] and Ronald Redmer[1]

[1]*Institut für Physik, Universität Rostock, 18051 Rostock, Germany*

[2]*Max-Planck-Institut für Sonnensystemforschung, 37077 Göttingen, Germany*

(Received 16 February 2021; accepted 17 May 2021; published 4 June 2021)

We study ionization and transport processes in partially ionized multicomponent plasmas. The plasma composition is calculated via a system of coupled mass-action laws. The electronic transport properties are determined by the electron-ion and electron-neutral transport cross sections. The influence of electron-electron scattering is considered via a correction factor to the electron-ion contribution. Based on these data, the electrical and thermal conductivities as well as the Lorenz number are calculated. For the thermal conductivity, we consider also the contributions of the translational motion of neutral particles and of the dissociation, ionization, and recombination reactions. We apply our approach to a partially ionized plasma composed of hydrogen, helium, and a small fraction of metals (Li, Na, Ca, Fe, K, Rb, and Cs) as typical for atmospheres of hot Jupiters. We present results for the plasma composition and the transport properties as a function of density and temperature and then along typical *P-T* profiles for the outer part of the hot Jupiter HD 209458b. The electrical conductivity profile allows revising the Ohmic heating power related to the fierce winds in the planet's atmosphere. We show that the higher temperatures suggested by recent interior models could boost the conductivity and thus the Ohmic heating power to values large enough to explain the observed inflation of HD 209458b.

DOI: 10.1103/PhysRevE.103.063203

I. INTRODUCTION

Partially ionized multicomponent plasmas are composed of molecules, atoms, and ions of various species as well as of free electrons. The plasma parameters of density and temperature determine their ionization degree and thus also their equation of state and transport properties such as electrical and thermal conductivity [1–8]. Profound knowledge of the thermophysical properties of such plasmas is important for applications in astrophysics, atmospheric science, and plasma technology. For instance, Earth's ionosphere [9,10] and the atmospheres of hot Jupiters [11,12] can be treated as low-density partially ionized multicomponent plasmas. Another example is the formation of stars out of initially cold and dilute clouds which consist mostly of molecular hydrogen, helium, and a small fraction of heavier elements and collapse due to gravitational instability [13,14]. The evolution to a protostar, which is much hotter and denser, runs through the plasma regime, where dissociation and ionization processes determine the heating and contraction dynamics essentially. The quenching gas in high-power circuit breakers [15] or arc plasmas [16] are examples of important technical applications of multicomponent partially ionized plasmas (PIPs).

The transport properties of partially ionized plasmas are determined by the ionization degree and the charge state distribution of its constituents. This defines the number of free electrons and the strength of the collisional interactions between the plasma species and determines their mobility. At low temperatures, the ionization degree is very low and the transport properties are dominated by neutral particles (atoms and molecules), while charged particles become more and more important with increasing temperature due to thermal ionization. Such thermal ionization conditions are typical for the outer atmospheres of planets in close proximity to their star, like hot Jupiters and hot mini-Neptunes [17]. The electrical conductivity, in particular due to the ionization of alkali metals, can rise to values where magnetic effects become important for the evolution and dynamics of the planetary interior.

Hot Jupiters orbit their parent stars in close proximity and are locked in synchronous rotation, which means that they always face the same side to the star. Several physical mechanisms are discussed to explain why the radii of hot Jupiters are significantly larger than expected [12,18,19]. One possibility is Ohmic dissipation that directly scales with the electrical conductivity.

The differential stellar irradiation drives fierce winds in the outer atmosphere that tend to equilibrate the difference in dayside and nightside temperatures. Interaction of the winds with a planetary magnetic field induces electric currents that can flow deeper into the planet. When efficient enough, the related Ohmic heating transports a sufficient fraction of the stellar irradiation received by the planet to deeper interiors where it could explain the inflation.

Accurate data on the composition and the transport coefficients along realistic pressure-temperature (*P-T*) profiles of hot Jupiters are also critical input in corresponding magnetohydrodynamics simulations [20]. Using the corresponding plasma composition, i.e., the molar fractions of the various

*sandeep.kumar@uni-rostock.de

species, and the absorption coefficient of the plasma, the opacity of the planet's atmosphere can be calculated, which in turn determines the P-T profile [21].

In this paper we calculate the ionization degree, the electrical and thermal conductivity, and the Lorenz number for a PIP as a function of temperature and mass density. Mass-action laws (MALs) are used to calculate the composition of the PIP [22–26]. We assume that the plasma is in thermal and chemical equilibrium so that Saha-like equations for each dissociation and ionization reaction can be derived, from which the partial densities of all species are calculated, i.e., the plasma composition. Furthermore, the electron-ion and electron-neutral transport cross sections have to be determined [27]. The effect of electron-electron scattering is considered by introducing a correction factor to the electron-ion contribution according to the Spitzer theory [28]. Note that the influence of the electron-electron interaction on the transport coefficients is currently of interest also for dense nonideal plasmas [29,30]. The contributions of the translational motion of neutrals and of the heat of dissociation, ionization, and recombination reactions to the thermal conductivity of PIP were also studied. For a benchmark we have compared the thermal conductivity of hydrogen plasma obtained from our model to the experimental arc-discharge results of Behringer and van Cung [31]. In the next step we study the general trends of the ionization degree and of the transport coefficients with respect to the plasma density and temperature. Finally, we calculate the ionization degree as well as the electrical and the thermal conductivity along typical P-T profiles through the atmosphere of the inflated hot Jupiter HD 209458b. These results are then used to assess the Ohmic heating in the planet's atmosphere and to infer whether this effect is efficient enough to explain the inflation. Batygin and Stevenson [11] (BS) have used simplified expressions for the calculation of the plasma composition (ionization scaled with the density scale height) and the electrical conductivity (weakly ionized gas) and concluded that Ohmic heating is indeed sufficient to explain the inflation of this hot Jupiter. We use our refined conductivity values to calculate updated estimates for the Ohmic heating in HD 209458b.

Our paper is organized as follows. In Sec. II we outline the theoretical basics for the calculation of the equation of state and the composition of the PIP. Section III provides the basic formulas used for the calculation of the electronic transport coefficients in the PIP. In Sec. IV we report the results for the ionization degree and the electronic transport coefficients in dependence on the plasma temperature and mass density. Section V gives details of the calculation of the translational motion of neutral particles and of the contribution of the heat of dissociation, ionization, and recombination reactions to the thermal conductivity. In Sec. VI, results for the ionization degree and the transport coefficients along typical P-T profiles through the atmosphere of the hot Jupiter HD 209458b are presented. A summary and conclusions are given in Sec. VII.

II. EQUATION OF STATE AND COMPOSITION

We consider an ideal-gaslike model for the partially ionized plasma and calculate its chemical composition using a canonical partition function $Z(\{N_i\}, V, T)$, which depends on the number of particles N_i of species i as well as on the volume V and temperature T of the plasma. We assume the constituent elements H, He, Li, K, Na, Rb, Ca, Fe, and Cs to be the relevant drivers of ionization in hot Jupiter atmospheric plasmas. The abundances of these constituents are given in Table I, which is adopted from Refs. [32,33].

TABLE I. Abundances of constituents considered in this work, with the molar and mass fractions according to Refs. [32,33].

Element	Molar fraction (%)	Mass fraction (%)
H	92.23	74.84
He	7.76	25.02
Li	1.75×10^{-7}	9.82×10^{-7}
Na	1.79×10^{-4}	3.3×10^{-3}
K	1.18×10^{-5}	3.74×10^{-4}
Ca	1.88×10^{-4}	6.1×10^{-3}
Fe	2.7×10^{-3}	0.119
Rb	2.21×10^{-8}	1.52×10^{-6}
Cs	1.16×10^{-9}	1.23×10^{-7}

In a mixture of c noninteracting chemical species, the partition function $Z(\{N_i\}, V, T)$ can be written as a product

$$Z(\{N_i\}, V, T) = \prod_{i=1}^{c} z_i(N_i, V, T), \tag{1}$$

with

$$z_i(N_i, V, T) = z_i^{\text{trans}}(N_i, V, T)\left[z_i^{\text{int}}(T)\right]^{N_i}, \tag{2}$$

where $z_i^{\text{trans}}(N_i, V, T)$ is the translational partition function of species i and $z_i^{\text{int}}(T)$ is its one-particle internal partition function (IPF). The translational partition function is given by

$$z_i^{\text{trans}}(N_i, V, T) = \frac{V^{N_i}}{N_i! \lambda_{th,i}^{3N_i}}, \tag{3}$$

in which $\lambda_{th,i} = h/\sqrt{2\pi m_i k_B T}$ is the thermal wavelength with the Planck constant h, the mass m_i of species i, and the Boltzmann constant k_B. The internal partition function modes are considered to be independent of each other, which gives the formula [34]

$$z_i^{\text{int}} = z_i^{\text{nuc}} z_i^{\text{el}} z_i^{\text{vib}} z_i^{\text{rot}}, \tag{4}$$

where z_i^{nuc}, z_i^{el}, z_i^{vib}, and z_i^{rot} are the nuclear, electronic, vibrational, and rotational partition functions of the species i, respectively.

The nuclear IPF is considered as

$$z_i^{\text{nuc}} = 2I_i^{\text{ns}} + 1, \tag{5}$$

which depends on the spin quantum number I_i^{ns} of the nucleus. The electronic partition function is approximated as follows:

$$z_i^{\text{el}} = (2J + 1)\exp\left(-E_i^0/k_B T\right). \tag{6}$$

Here E_i^0 is the energy and J the electronic angular momentum quantum number of the atom, ion, or molecule in the ground state. We do not consider excited states in this study because their population is small for the plasma parameters considered here so that their effect on ionization and transport is negligible. Note that each excited state introduces a new species for

which all related atomic, ionic, or molecular parameters need to be known for the calculation of the plasma composition and the transport cross sections which would unnecessarily complicate the PIP model as long as their effect is small. For the calculation of the vibrational and rotational partition functions of the H_2 molecule we use the high-temperature approximation

$$z_{H_2}^{\mathrm{vib}} = \frac{1}{1-\exp(-\theta_v/T)}, \tag{7}$$

$$z_{H_2}^{\mathrm{rot}} = \frac{T}{2\theta_r}, \tag{8}$$

where $\theta_v = h\nu/k_B$ and $\theta_r = h^2/8\pi^2 I k_B$ are the vibrational and rotational temperatures, respectively. The latter depends on the moment of inertia $I = \mu_{\mathrm{HH}} r^2$ of the H_2 molecule; $\mu_{\mathrm{HH}} = m_{\mathrm{H}}/2$ is its reduced mass and r its bond length.

The plasma considered here is in thermal and chemical equilibrium, so the particle densities follow from MALs as follows [26]:

$$\prod_i n_i^{\nu_{i,a}} = \prod_i \frac{\left(z_i^{\mathrm{int}}\right)^{\nu_{i,a}}}{\left(\lambda_{th,i}^3\right)^{\nu_{i,a}}} \equiv K_a(T). \tag{9}$$

In this expression, $n_i = N_i/V$ are number densities of species i, $K_a(T)$ is the reaction constant, and $\nu_{i,a}$ are the stoichiometric coefficients of the reaction a. The $\nu_{i,a}$ for the reaction products and reactants are chosen to be positive or negative, respectively. The MALs and particle conservation equations of the PIP are solved numerically to calculate the number density of each species for a given temperature and mass density. We allow the constituents to be doubly ionized at maximum. This sets a maximum temperature of about 30 000 K for our applications, which corresponds to about 10% of the lowest third ionization energy (30.651 eV for Fe [35]) of all constituents considered. The MALs for dissociation and ionization read

$$\frac{n_{\mathrm{H}}^2}{n_{H_2}} = K_{\mathrm{H}}, \tag{10}$$

$$\frac{n_{\mathrm{ion},i}^{+} n_e}{n_{\mathrm{atom},i}} = K_{\mathrm{ion},i}^{+}, \tag{11}$$

$$\frac{n_{\mathrm{ion},i}^{2+} n_e}{n_{\mathrm{ion},i}^{+}} = K_{\mathrm{ion},i}^{2+}, \tag{12}$$

in which n_{ion}^{+} and n_{ion}^{2+} denote the number densities of a singly or doubly charged ion, respectively. The charge neutrality condition in the PIP leads to the equation

$$n_e = \sum_i n_{\mathrm{ion},i}^{+} + \sum_i 2 n_{\mathrm{ion},i}^{2+}, \tag{13}$$

where n_e represents the free electron number density in the PIP. Mass conservation in the plasma provides the relation

$$\rho = \sum_{i=1}^{c} m_i n_i, \tag{14}$$

where ρ is mass density of the plasma. The relative abundance χ_r of each constituent with respect to the H abundance is set as follows:

$$\chi_{r,i} = \frac{n_{\mathrm{atom},i} + n_{\mathrm{ion},i}^{+} + n_{\mathrm{ion},i}^{2+}}{2n_{H_2} + n_{\mathrm{H}} + n_{\mathrm{H}^+}}. \tag{15}$$

Most of the parameters such as ground-state energies E_i^0, ionization energies, total angular momentum quantum numbers J, and atomic weights m_i of the species are taken from the NIST database [35]. The nuclear partition function and ground-state energy of the H_2 molecule are taken as $z_{H_2}^{\mathrm{nuc}} = 4$ and $E_i^0 = -31.738$ eV [26], respectively. The ground-state energy of the H_2 molecule already includes the vibrational ground-state energy. Therefore, the vibrational partition function (7) includes only excited states. We have taken $\theta_v = 6321.3$ K and $\theta_r = 88.16$ K for the vibrational and rotational temperatures of the H_2 molecule [36], respectively. The number densities n_i of each species (molecules, atoms, and ions) for a given plasma temperature and mass density are calculated by solving the coupled equations (10)–(15) using the Newton-Raphson method. The resulting ionization degree α of the plasma is defined as

$$\alpha = \frac{n_e}{n_{\mathrm{total}}}, \tag{16}$$

with $n_{\mathrm{total}} = n_{\mathrm{atoms}} + 2n_{H_2} + n_e$ and the density of all atoms $n_{\mathrm{atoms}} = \sum_i n_{i,\mathrm{atom}}$.

The numerical calculations were benchmarked against the analytical solution of Eqs. (17)–(19) for a pure hydrogen plasma composed of H_2, H, H^+, and electrons:

$$\frac{m_{H_2}}{K_{H_2}} n_{\mathrm{H}}^2 + m_{\mathrm{H}} n_{\mathrm{H}} + m_{\mathrm{H}^+}\sqrt{n_{\mathrm{H}} K_{\mathrm{H}}^{+}} - \rho = 0. \tag{17}$$

In the analytical model, the density of H atoms n_{H} is obtained from the solution of Eq. (17). Furthermore, using n_{H}, we can calculate n_{H_2} and n_{H^+} via the following equations:

$$n_{H_2} = \frac{n_{\mathrm{H}}^2}{K_{\mathrm{H}}}, \tag{18}$$

$$n_{\mathrm{H}^+} = \sqrt{n_{\mathrm{H}} K_{\mathrm{H}}^{+}}. \tag{19}$$

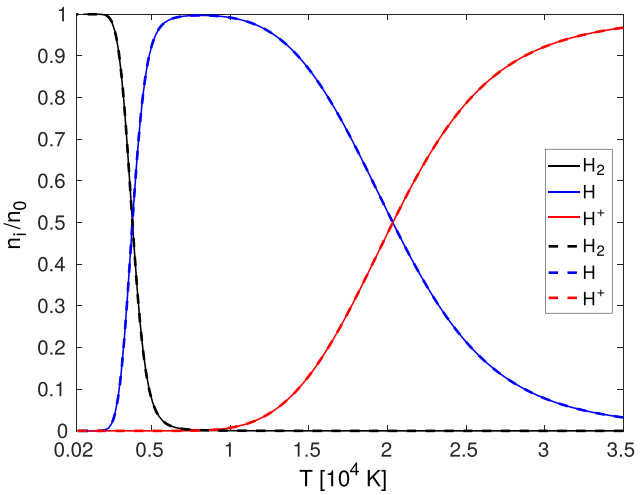

FIG. 1. Composition of hydrogen plasma as a function of temperature for a mass density of $\rho = 10^{-5}$ g/cm^3. Solid lines show analytical results via Eqs. (17)–(19) and dashed lines numerical results. The normalization $n_0 = n_{H_2} + n_{\mathrm{H}} + n_{\mathrm{H}^+}$ refers here to the total number density of hydrogenic species in the plasma.

For benchmarking, the mass density ρ of the plasma is kept constant at 10^{-5} g/cm^3 and the composition is calculated as a function of the temperature (see Fig. 1). The analytical and numerical results are virtually identical. At low temperatures, hydrogen is a molecular gas; the molecules dissociate into atoms with increasing temperature. At even higher temperature, the ionization processes lead to a hydrogen plasma. For further validation, we compare our results for the ionization degree with those of Schlanges *et al.* [37] and find good agreement.

III. ELECTRONIC TRANSPORT COEFFICIENTS

The electronic contribution to the electrical conductivity σ_e, the thermal conductivity λ_e, and the Lorenz number L are defined as [27,38]

$$\sigma_e = e^2 K_0, \tag{20}$$

$$\lambda_e = \frac{1}{T}\left(K_2 - \frac{K_1^2}{K_0}\right), \tag{21}$$

$$L = \left(\frac{e}{k_B}\right)^2 \frac{\lambda_e}{\sigma_e T}, \tag{22}$$

where e is the elementary charge and K_n are Onsager coefficients ($n = 0, 1, 2$) that are composed of individual specific Onsager coefficients $K_{n,es}$ via

$$K_n^{-1} = \sum_s K_{n,es}^{-1}. \tag{23}$$

The expressions for $K_{n,eN}$ and $K_{n,eI}$ are taken from French and Redmer [27] and describe the contribution of electron scattering from neutral (index N) and ionic (index I) species, respectively. We have considered electron-neutral scattering only for H, H_2, and He atoms or molecules because of the very small overall abundance of the heavier elements. The analytical expression of the specific Onsager coefficients for electron-neutral scattering for Eq. (23) is

$$K_{n,eN} = \frac{2^{11/2}\pi^{1/2}(n+3)!\varepsilon_0^2 (k_B T)^{n+3/2} n_e}{3Z_N^2 e^4 m_e^{1/2} n_N \ln A_N(x_N)}. \tag{24}$$

The specific Onsager coefficients for electron-ion scattering for Eq. (23) read

$$K_{n,eI} = \frac{2^{11/2}\pi^{1/2}(n+3)!\varepsilon_0^2 (k_B T)^{n+3/2} n_e}{3Z_I^2 e^4 m_e^{1/2} n_I \ln \Lambda(B_n)}. \tag{25}$$

The logarithmic functions $\ln A_N(x_N)$ and $\ln \Lambda(B_n)$ are defined in Ref. [27]. Electron-electron scattering is accounted for by correction factors according to Spitzer and Härm [28] in the Onsager coefficients for electron-ion scattering $K_{n,eI}$. The respective formula and parameters are taken from French and Redmer [27]. The effect of electron-electron scattering on the electrical and thermal conductivity of dense plasmas in the warm dense matter regime has been studied by Reinholz *et al.* [29] using the linear response theory and by Dejarlais *et al.* [30] using the Kohn-Sham density functional theory. The expressions for the Onsager coefficients including

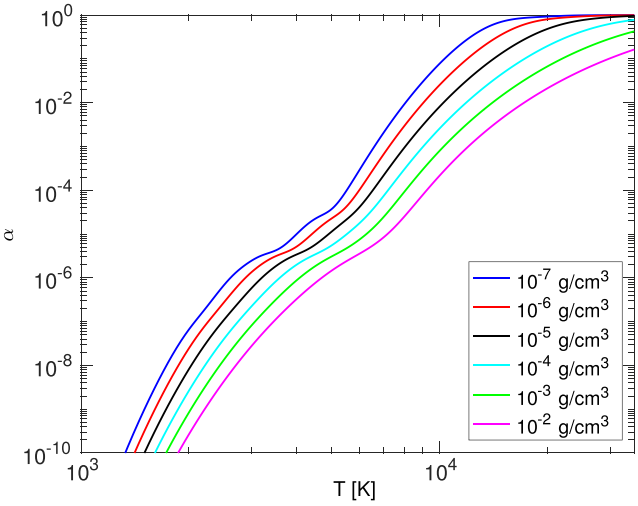

FIG. 2. Ionization degree of the PIP as a function of temperature for different mass densities.

electron-electron scattering are

$$K_{0,eI+ee} = \frac{f_e}{f_I} K_{0,eI}, \tag{26}$$

$$K_{1,eI+ee} = \frac{a_e f_e}{a_I f_I} K_{1,eI} + \frac{5}{2} k_B T \left(\frac{f_e}{f_I} - \frac{a_e f_e}{a_I f_I}\right) K_{0,eI}, \tag{27}$$

$$K_{2,eI+ee} = \frac{L_e f_e}{L_I f_I}\left(K_{2,eI} - \frac{K_{1,eI}^2}{K_{0,eI}}\right) + \frac{K_{1,eI+ee}^2}{K_{0,eI+ee}}, \tag{28}$$

where the factors f_I, f_e, a_I, a_e, L_I, and L_e are defined in Ref. [27].

IV. RESULTS FOR ELECTRONIC TRANSPORT IN PIP

The plasma composition, i.e., the partial number densities n_i of each species obtained from solving the coupled equations (10)–(15), is a necessary input for the calculation of the electronic transport coefficients. Therefore, we first show the behavior of the ionization degree as a function of the temperature at different mass densities in Fig. 2. The ionization degree α is increasing with the temperature due to thermal ionization of the constituents and decreasing with the mass density of the plasma.

The variation of σ_e and λ_e with the temperature at different mass densities is displayed in Figs. 3 and 4, respectively. The curves for σ_e and λ_e show a systematic increase with temperature, caused by thermal ionization of the constituents in the order of their ionization energies, which leads to an enhancement of the free electron density in the PIP. On the other hand, σ_e and λ_e are decreasing with mass density due to more frequent scattering processes with neutral species. At high temperatures (above 20 000 K), σ_e and λ_e are increasing with mass density, oppositely to their low-temperature characteristics. This reversal is emerging because the ionization degree is still increasing with temperature for the higher densities but it is already saturated for the lower densities. The quantities

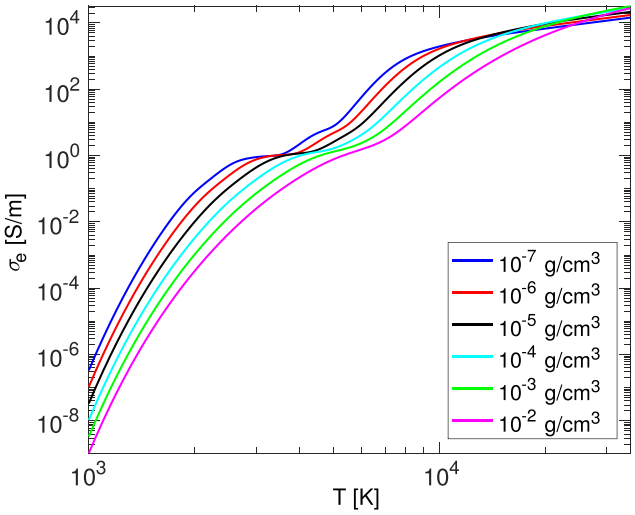

FIG. 3. Electrical conductivity of the PIP as a function of temperature for different mass densities.

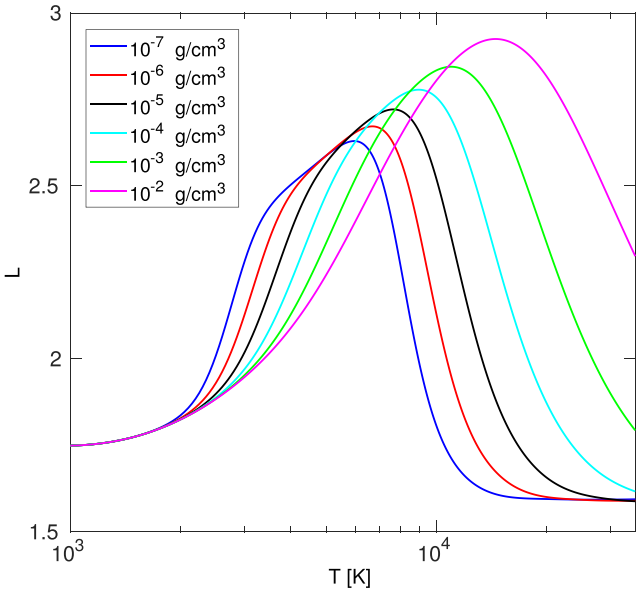

FIG. 5. Lorenz number of the PIP as a function of temperature for different mass densities.

α, σ_e, and λ_e show plateaulike structures. When the plateau is reached, all metals (see Table I) are ionized but H and He require still higher temperatures to contribute to the ionization degree significantly and thus to the electrical and thermal conductivities, which lead to the increase after the plateau. The Lorenz number shown in Fig. 5 first increases with the temperature and, after passing through a maximum, decreases for still higher temperatures. This behavior is shifted systematically towards higher temperatures with increasing density. The high- and low-temperature limiting values of L are determined by the known Spitzer limit in the fully ionized plasma and electron-neutral cross sections in the weakly ionized gas, respectively. The occurrence of the pronounced maximum in L is caused by different energetic weightings of the cross sections in the specific Onsager coefficients [see Eqs. (24) and (25)]. It should be noted that the correction due to electron-

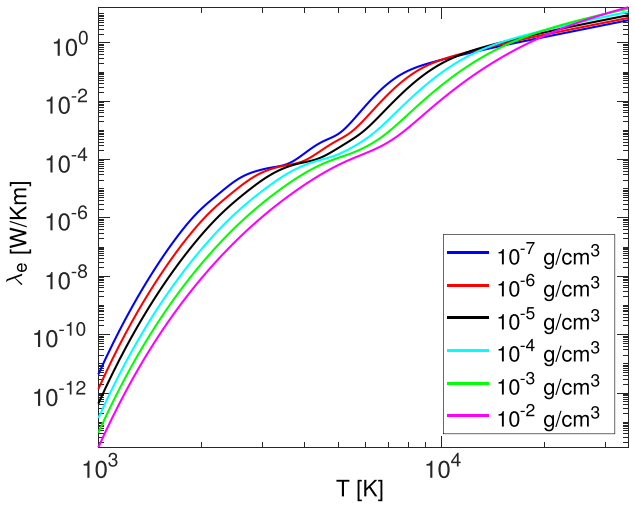

FIG. 4. Thermal conductivity of the PIP as a function of temperature for different mass densities.

electron scattering is only important when the majority of constituent elements are at least singly ionized.

V. THERMAL CONDUCTIVITY FROM NEUTRALS AND CHEMICAL REACTIONS

At low temperatures, the ionization degree is small and therefore the neutral particles contribute significantly to the heat transport. In addition to their translational contribution λ_{tr}, the occurrence of dissociation and ionization reactions also enhances the thermal conductivity in the corresponding temperature region, described by a term λ_r. These contributions have to be added to the electronic heat conductivity λ_e so that the total thermal conductivity λ of the PIP is given by

$$\lambda = \lambda_e + \lambda_{tr} + \lambda_r. \tag{29}$$

We have neglected the translational contribution of ions to the thermal conductivity because it is very small in comparison to that of the electrons λ_e [39,40]. For the neutrals, we have adopted the Chapman-Enskog model for the calculation of the translational heat transport. The first-order expression for λ_{tr} for a single-component gas is given by [41]

$$\lambda_i^{tr} = \frac{25}{32}\left(\frac{k_B T \pi}{m_i}\right)^{1/2} \frac{C_{v,i}}{\Omega_{ii}^{(2,2)}(T)}, \tag{30}$$

where $\Omega_{ii}^{(2,2)}(T)$ is a collision integral and $C_{v,i} = 3k_B/2$ is the heat capacity for atoms of species i at constant volume. The collision integral depends upon the energy-dependent transport cross section. We have simplified the collisional integral by assuming the atoms or molecules to be rigid spheres of diameter d_{ii} so that $\Omega_{ii}^{(2,2)}(T)$ becomes temperature independent and is reduced to πd_{ii}^2. The simplified formula of λ_i^{tr} is then

given by

$$\lambda_i^{tr} = \frac{25}{32}\left(\frac{k_B T \pi}{m_i}\right)^{1/2} \frac{C_{v,i}}{\pi d_{ii}^2}. \tag{31}$$

The vibrational heat capacity $C_{v,\mathrm{H_2}}^{\mathrm{vib}}$ of hydrogen molecules is calculated using the harmonic approximation [34]

$$C_{v,\mathrm{H_2}}^{\mathrm{vib}} = k_B\left(\frac{\theta_v}{T}\right)^2 \frac{\exp(\frac{\theta_v}{T})}{\left[\exp\left(\frac{\theta_v}{T}\right)-1\right]^2}. \tag{32}$$

The rotational heat capacity $C_{v,\mathrm{H_2}}^{\mathrm{rot}}$ of hydrogen molecules is calculated by considering $T \gg \theta_r$ so that

$$C_{v,\mathrm{H_2}}^{\mathrm{rot}} = k_B. \tag{33}$$

For a multicomponent plasma as considered here, we use a generalized formula for the calculation of the translational thermal conductivity of mixtures, which reads [42–44]

$$\lambda_{tr} = \sum_i \frac{x_i \lambda_i^{tr}}{1 + \sum_{j\neq i} \frac{x_j}{x_i}\phi_{ij}}. \tag{34}$$

Here x_i is the molar fraction of species i and $\phi_{ij} = (2\mu_{ij}/m_i)^2$ depends on the reduced mass μ_{ij} and mass of species i.

In the calculation of λ_r we assume that the chemical reactions occur in different temperature regions, so their contributions are additive, according to an expression given by Butler and Brokaw [45,46],

$$\lambda_r = \sum_a \frac{(\Delta H_a)^2}{RT^2}\frac{1}{A_a}, \tag{35}$$

with

$$A_a = \sum_{k=1}^{\beta-1}\sum_{l=k+1}^{\beta}\left(\frac{RT}{PD_{kl}}\right)x_k x_l\left[\left(\frac{\nu_{k,a}}{x_k}\right)-\left(\frac{\nu_{l,a}}{x_l}\right)\right]^2, \tag{36}$$

where ΔH_a is the heat of the reaction a, β is the number of species involved in the reaction, k represents the kth species, R is the universal gas constant, $P = \sum_i n_i k_B T$ is the ideal pressure, and D_{kl} is the binary diffusion coefficient between components k and l. The heat of the reaction ΔH_a is calculated from the reaction constant by van't Hoff's equation [47,48]

$$\frac{\Delta H_a}{RT^2} = \frac{d\ln K_a}{dT}. \tag{37}$$

We use the following expression for the neutral-neutral and neutral-ion binary diffusion coefficients [49]:

$$PD_{kl} = \frac{3}{16}\frac{\sqrt{2\pi k_B^3 T^3/\mu_{kl}}}{\pi d_{kl}^2}. \tag{38}$$

For the electron-neutral and electron-ion diffusion coefficients, we have used the Darken relation and the adiabatic approximation [50], which leads to

$$D_{ke} = x_k D_e + x_e D_k \approx x_k D_e. \tag{39}$$

This expression depends only on the self-diffusion coefficient D_e of the electrons that can be related to their electrical conductivity using the Nernst-Einstein relation

$$PD_{ke} = \frac{x_k}{x_e}\left(\frac{k_B T}{e}\right)^2 \sigma_e. \tag{40}$$

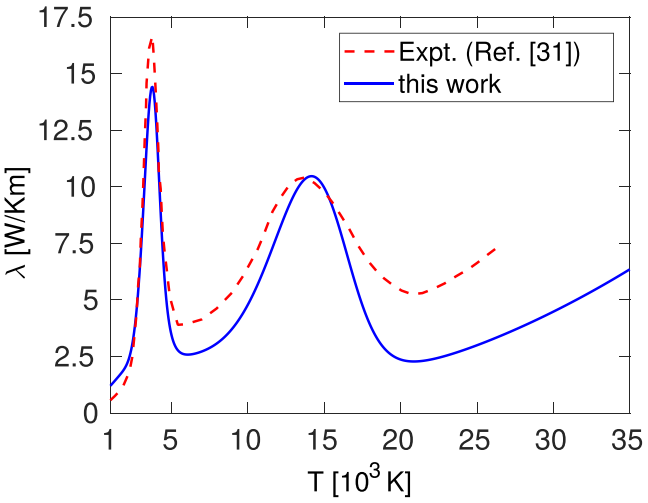

FIG. 6. Thermal conductivity of partially ionized hydrogen plasma as a function of temperature at a constant pressure of 1 bar. We compare our results with the arc-discharge experiment of Behringer and van Cung [31], which was evaluated using the local thermodynamic equilibrium assumption.

We consider the λ_{tr} and λ_r contributions to the thermal conductivity only for species and reactions containing the elements H and He. The hard-sphere diameters of H_2, H, and He are taken from Table II in Ref. [51], specifically of H-H_2 collision data at 3500 K. We have parametrized the effective H-H^+ interaction diameter in our model by matching the height of the second peak in the thermal conductivity profile with that from hydrogen arc-discharge experiments at $P = 1$ bar [31]; the comparison is shown in Fig. 6. The He-He^+ and He^+-He^{2+} interaction diameters have been calculated from Eq. (38) by using the diffusion coefficient value of Devoto and Li at 24 000 K [52]. All hard-sphere diameter values used for the calculation of the thermal conductivity are compiled in Table II.

The variation of λ, λ_r, λ_{tr}, and λ_e with the temperature is displayed in Fig. 7, again for a constant density of 10^{-5} g/cm^3. The λ_{tr} contribution fully determines the total thermal conductivity at the lowest temperatures considered here. Note that the electronic contribution can be neglected there because the ionization degree is virtually zero (see Fig. 1). The first peak in λ at about 4000 K emerges due to the dissociation reaction heat conductivity of H_2 molecules in the PIP. This

TABLE II. Square of the hard-sphere diameters d_{ij} for the interactions between the various species as used in the calculation of the thermal conductivity.

Collision	d_{ij}^2 (Å^2)
H_2-H_2	2.634
H-H_2	2.634
H-H	2.634
H-H^+	11.00
He-He	2.634
He-He^+	13.978
He^+-He^{2+}	13.978

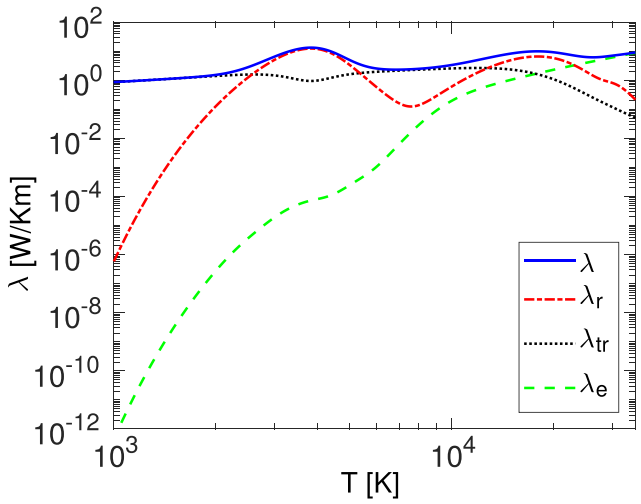

FIG. 7. Total thermal conductivity λ according to Eq. (29) as a function of temperature at 10^{-5} g/cm^3. The contributions of the translational motion of neutrals λ_{tr} and of the heat of chemical reactions λ_r and the electronic contribution are shown separately.

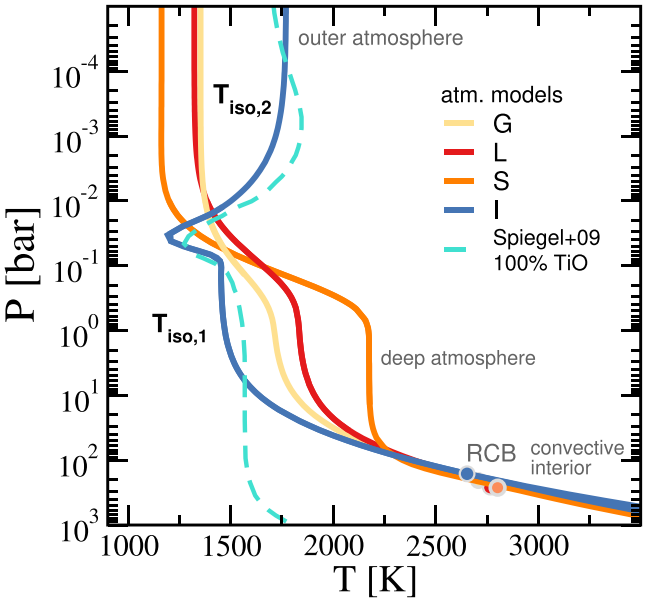

FIG. 8. Pressure-temperature profiles of the atmosphere of HD 209458b. Shown are the four atmospheric models used in this work, three without an inversion, namely, G (yellow), L (red), and S (orange), and one with an inversion in the temperature, I (blue), located at about 0.03 bar. Further features of the models are displayed: the location of the radiative-convective boundary, the onset of the convective interior, and the characteristic temperatures $T_{\mathrm{iso},1}$ and $T_{\mathrm{iso},2}$.

contribution becomes smaller at higher temperatures because most of the H_2 molecules are dissociated into H atoms. As temperature increases further, the H atoms are ionized, which leads to a second peak in the thermal conductivity at about 20 000 K due to the corresponding ionization reaction heat. A shoulder in λ_r emerges at about 30 000 K due the ionization of He. The free electron density n_e is systematically increasing with temperature so that λ_e dominates the thermal conductivity λ in the high-temperature limit above 25 000 K and both λ_{tr} and λ_r can be neglected there.

VI. APPLICATION TO THE ATMOSPHERE OF THE HOT JUPITER HD 209458b

HD 209458b was the first exoplanet observed transiting its host star [53]. With an orbital period of 3.5 days, a semimajor axis of only 0.047 AU, a radius of $1.36R_J$, and a mass of $0.69M_J$, HD 209458b is clearly an inflated hot Jupiter [54]. Here R_J and M_J denote Jupiter's radius and mass, respectively.

In this section we apply the methods discussed above to HD 209458b and discuss how the updated electrical conductivity would affect Ohmic heating. The electrical currents responsible for the Ohmic heating could penetrate down to a pressure level of few kbar according to BS. We therefore focus the application of our PIP model on this pressure range and start by discussing the corresponding *P*-*T* profile.

A. The *P*-*T* profile of the atmosphere

We calculate the composition and the transport coefficients of the planetary PIP for the four planetary models shown in Fig. 8. The atmospheric models are obtained by fitting semianalytical one-dimensional parametrizations to pressure-temperature profiles suggested in the literature, following the approach by Poser *et al.* [55]. The parametrization guarantees a consistent description and allows us to extend all models to the same pressure range and to connect them to an adiabatic interior.

Model G is based on the globally averaged theoretical *P*-*T* curve by Guillot [56], while model L replicates the most recent result by Line *et al.* [57], which is based on high-resolution spectroscopy data of the Hubble Space Telescope and data from the Spitzer Space Telescope for the planet's dayside. Both profiles turn out to be very similar. Profiles S and I follow suggestions by Spiegel *et al.* [58]. While profile S has a particularly high temperature between 0.3 and 100 bar, model I, based on the variant with a solar abundance of TiO by Spiegel *et al.* [58], shows a temperature inversion at pressures smaller than 30 mbar. The reason is that the highly abundant TiO serves as an additional absorber in the upper atmosphere and leads to the rise in temperature.

Our parametrization of model I is broadly similar to the original profile of Spiegel *et al.* [58] but assumes a shallower transition to the convective interior and thus predicts higher temperatures for pressures beyond 10 bar. In addition, our temperatures are up to 100 K lower than the original in the isothermal region between 1 and 10 mbar. Between 10^{-2} and 10^{-3} bar, the original shows a local maximum that is not present in our model. The temperatures in profile I are therefore up to 200 K colder than in the original paper.

We connect our atmosphere profiles to an adiabatic interior model at the pressure level where the atmospheric temperature gradient matches with the adiabatic gradient. The respective transition points are marked with circles in Fig. 8. The interior model is derived from the usual structure equations for nonrotating spherical gas planets (see, e.g., [59]). Like BS, we use a solar helium mass fraction of $Y = 0.24$, assume no planetary

core, and set the heavy-element mass fraction of both the atmosphere and the interior to the solar reference metallicity of $Z_\odot = 0.015$ [33]. For H and He we use the equation of state (EOS) of Saumon *et al.* [60]. Heavy elements are represented by the ice EOS of Hubbard and Marley [61]. The upper boundary of our interior model is set to $P_{\rm out}(R_P) = 10^{-2}$ bar. The heat flux from below is determined by the interior model (no core). The observed radius inflation is then obtained by adding extra energy during the thermal evolution [55,62].

Batygin and Stevenson also used variants of the original model I by Spiegel *et al.* [58] for their Ohmic dissipation study. Like us, they assumed a transition to an adiabatic interior model in a comparable pressure range. Their exact profiles have not been published but are likely similar to our model I.

Beyond the radiative-convective boundary (RCB), the atmosphere models span a large temperature range of up to 750 K around 1 bar. This may partly be owed to the large local variation in brightness temperature with a dayside-to-nightside difference of about 500 K [63] but mostly reflects the different model assumptions and a lack of observational constraints [64]. Note, however, that the most recent observation-based model by Line *et al.* [57] could not confirm the inversion discussed by Spiegel *et al.* [58] and covers an intermediate-temperature range.

All of our atmosphere models have two nearly isothermal regions. The deeper region, labeled $T_{\rm iso,1}$ in Fig. 8, is a typical feature in strongly irradiated planets [12,65]. The shallower isothermal region $T_{\rm iso,2}$ from the 10 mbar level to the outer boundary of our models is typical for analytical, semigray atmosphere models (see, e.g., [66]). For profiles G, L, and S, both regions are connected by a pronounced temperature drop of several hundred degrees Kelvin. In the inversion profile, the temperature first drops but then increases towards the outer boundary.

B. Transport properties of the atmosphere

We have calculated the ionization degree α, the electrical conductivity σ_e, and the thermal conductivity λ along our four P-T models for HD 209458b (see Fig. 9). The ionization degree [Fig. 9(b)] and the electrical conductivity [Fig. 9(d)] are closely related and follow a very similar behavior (see Sec. IV). The thermal conductivity profile [Fig. 9(c)] also shows a similar form but with much smaller variations.

In the two isothermal regions of each profile, the decreasing density causes α and σ_e to increase outward. However, the drastic changes of temperature in the intermediate regions between the isothermal layers influence α and σ_e in more characteristic ways. This is especially the case in the inversion region in profile I (blue), where we find pronounced minima of α and σ_e near 30 mbar (see Fig. 9).

Due to the large differences between the models, the ionization degree and electrical conductivity differ by up to three orders of magnitude for the same pressure. The drop in electrical conductivity between the two isothermal regions varies from one order of magnitude in model G to more than three orders of magnitude in model S. The increase from the inner isothermal region to the RCB varies from a bit more than two orders of magnitude in model S to four orders of magnitude in model I. In contrast, the variation of the thermal conductivity between the models is much smaller. The reason is that thermal conductivity is determined mostly by collisions between neutral particles in the relevant temperature range and is thus not susceptible to the strongly changing ionization degree.

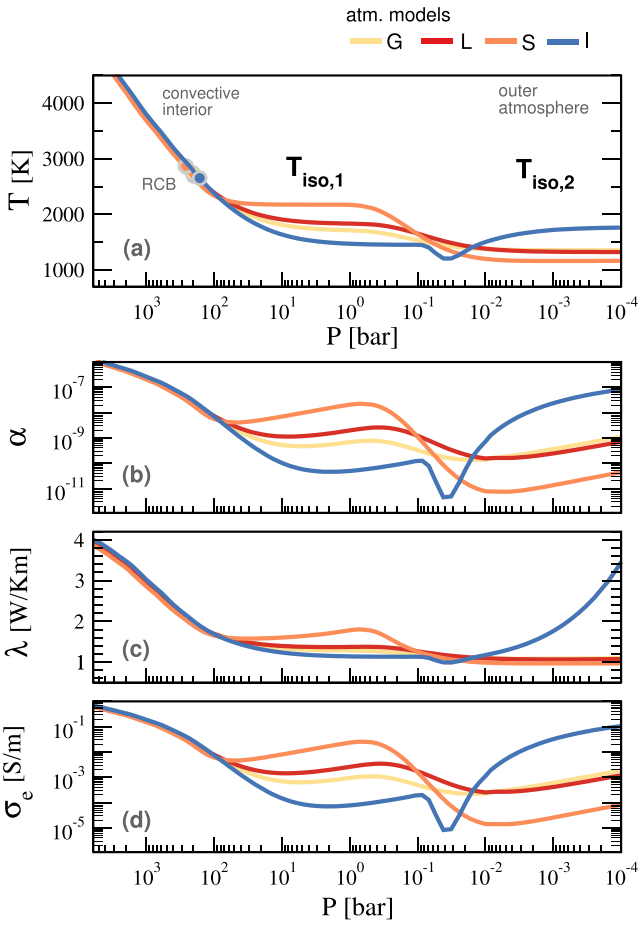

FIG. 9. Temperature T, ionization degree α, thermal conductivity λ, and electrical conductivity σ_e for different planetary interior models along the pressure axis of HD 209458b, specifically, for the four atmospheric models used in this work: G (yellow), L (red), S (orange), and one with an inversion, I (blue). Circles in the temperature profile represent the location of the radiative-convective boundary.

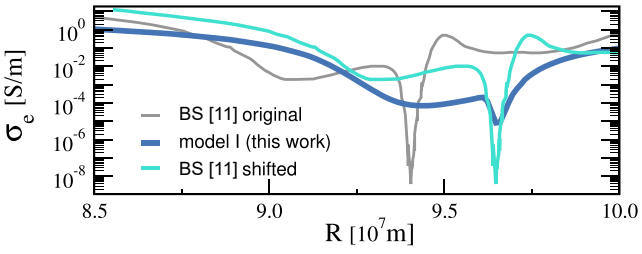

FIG. 10. Electrical conductivity σ_e for model I along the radius axis of HD 209458b, compared to the results of Batygin and Stevenson [11]. We show their original data (gray) as well as a shifted version (cyan) to ease the comparison (see the text).

Figure 10 compares the electrical conductivity for model I with the results taken from Fig. 2 in [11]. The associated pressure profile $P(r)$ is obtained by solving the equation of hydrostatic equilibrium. Each of the curves has a pronounced minimum in the electrical conductivity. Note that these minima are located at different radii in Fig. 10, which is likely caused by a different planetary radius assumed by BS that unfortunately was not stated in their paper. For better comparison, we also show a shifted Batygin-Stevenson profile in Fig. 10 that aligns both minima.

The electrical conductivity minimum predicted by BS is extraordinarily deep, with σ_e dropping by six orders of magnitude. In contrast, the temperature dependence of our model (see Fig. 3) yields a conductivity drop by only two orders of magnitude at the 300 K temperature dip of our model I.

In the inner isothermal region, the electrical conductivity is two orders of magnitude lower than suggested by BS. Unfortunately, we do not know the exact atmosphere model used by BS but, as discussed above, it seems conceivable that the temperatures in this region are about 100 K lower than assumed by BS for their Fig. 2. According to Fig. 3, however, this would only explain a conductivity difference by about a factor 5. At very low pressures and also toward the RCB, the electrical conductivities become more similar, likely because our model assumes higher temperatures. At the RCB, our electrical conductivity is about one order of magnitude lower than suggested by BS.

C. Ohmic dissipation

The electric currents $\vec{j}_e$ in the outer atmosphere are induced by the interaction of the fierce atmospheric winds with the planetary magnetic field according to Ohm's law

$$\vec{j}_e = \sigma_e(\vec{U} \times \vec{B}_0 - \vec{\nabla}\Phi), \tag{41}$$

where $\vec{U}$ is the wind velocity, $\vec{B}_0$ the internally produced background field, and Φ the electric potential. Note that we use a fluid approach where the velocity describes the motion of the neutral medium (neutrals, ions, and electrons). Furthermore, we use a linear approximation, assuming that the magnetic field locally produced by the currents is smaller than the background field [67,68]. Using the fact that the currents are divergence-free, i.e., $\vec{\nabla} \cdot \vec{j}_e = 0$, allows calculating the missing electric potential (BS). The global heating power from Ohmic dissipation is then simply given by the following volume integral:

$$\dot{Q} = \int \frac{\vec{j}_e^2}{\sigma_e} dV. \tag{42}$$

Being driven by the differential irradiation, the depth of the winds is limited [69]. Batygin and Stevenson assume that they penetrate down to the 10 bar level. Because the minimum in the electrical conductivity around 30 mbar provides a boundary for the electric currents, only the layer from 10 bar up to this minimum has to be considered for inducing the currents that could potentially penetrate deeper into the planet. We refer to this region as the induction layer. While the electric currents in the induction layer already provide very powerful heating, the deeper penetrating currents are more relevant for explaining the inflation. We refer to the deeper layer where these currents remain significant as the leakage layer, which may extend from 10 bar to a few kbar (BS).

With no appreciable flows being present between 10 bar and the RCB, the respective currents in the leakage layer obey the simpler relation

$$\vec{j}_e = -\sigma_e \vec{\nabla}\Phi. \tag{43}$$

The electric potential differences $\vec{\nabla}\Phi$ are determined by the action in the induction layer and the electrical conductivity distribution. Batygin and Stevenson therefore call the leakage layer the inert layer. The electrical conductivity profile controls how deep the currents produced in the induction layer flow into the leakage layer.

We can now roughly quantify the changes in Ohmic heating compared to those of BS by simply rescaling their results with our electrical conductivity profiles. Batygin and Stevenson assumed a simple flow structure with typical velocities of $U = 1$ km/s and a background field strength of $B_0 = 10$ G. Because our electrical conductivity is about two orders of magnitude lower in the induction layer, the induced electric currents are two orders of magnitude weaker, according to Eq. (41). Consequently, the Ohmic heating power (42) is also two orders of magnitude lower.

In the leakage layer, the currents encounter a conductivity that is more similar to the one assumed by BS. Assuming that the conductivity is one order of magnitude lower (see Fig. 10), the deeper Ohmic heating is about 10^{-3} times smaller than in the work of BS. Explaining the inflation of HD 209458b requires a power of about 4×10^{18} W to be deposited at or below the RCB [19]. While the models considered by BS deposit up to 10^{20} W in the convective interior, the lower electrical conductivity of model I would render Ohmic heating too inefficient.

However, as shown above, the Ohmic heating processes depend strongly on the conductivity and thus on the atmosphere model. Because of the higher temperatures, the electrical conductivity in the induction layers of the most-up-to-date model L is comparable to that assumed by BS; consequently, the induced currents also have a similar magnitude. If assuming once more a ten times lower conductivity in the leakage layer, the leakage layer heating will be ten times stronger than in the work of BS, which is more than enough to explain the inflation. For model S, the heating will be even stronger because of the particularly high temperatures in the induction region.

Because the electrical currents depend linearly on the wind velocity U and the background field strength B_0, the heating power (42) scales quadratically with both of these quantities. Updating the value of $U = 1$ km/s assumed by BS with a newer estimate of $U = 2$ km/s [70] thus increases Ohmic heating by a factor of 4. On the contrary, an indirect reassessment of the magnetic field strength of HD 209458b suggests that it may as well be on the order of 1 G [71] rather than the 10 G assumed by BS. This would reduce the Ohmic heating power by a factor of 100 and may once more render the process too inefficient to explain the inflation.

All the estimates discussed above represent a linear approximation, assuming that the magnetic field produced by the locally induced currents is smaller than the background field in Eq. (41) [67,68,72]. The ratio of the locally induced

field to the background field is roughly given by the magnetic Reynolds number

$$\mathrm{Rm} = U d \sigma_e \mu_0, \tag{44}$$

where μ_0 is the magnetic permeability of vacuum and d the electrical conductivity scale height

$$d = \frac{\sigma_e}{|\partial \sigma_e / \partial r|}. \tag{45}$$

The linear approximation therefore breaks down when Rm exceeds one. When assuming $U = 1$ km/s and the value $d = 3 \times 10^2$ km as suggested by Fig. 10, this happens where the electrical conductivity is larger than $\sigma_e = 10^{-2}$ S/m in the induction region. Model S, where $T_{\mathrm{iso},1} = 2200$ K, is the only model for which the linear approximation is certainly questionable.

Observations suggest that dayside and nightside temperatures of HD 209458b differ by roughly 500 K [63]. The fact that this difference is smaller than expected is, like the pronounced hot-spot shift [63], likely the result of heat distribution by the fierce winds in the upper atmosphere. The temperature dependence proposed here predicts that the electrical conductivity in the nightside induction region is about 10^3 times lower than on the dayside. We thus expect that dayside heating would dominate.

VII. CONCLUSION

We have presented a model for calculating the chemical composition and electrical and thermal conductivity of low-density multicomponent plasmas suitable for applications in atmospheres of hot Jupiters. This model is based on mass-action laws and cross sections for all binary particle interactions and generalizes an earlier model for the thermoelectric properties of one-component plasmas [25] to multicomponent plasmas. We have shown that the results for the ionization degree and in particular for the electrical conductivity can differ by several orders of magnitude from simpler models applied to hot Jupiter [11,73] or hot Neptune atmospheres [17].

Note that the plasma becomes nonideal with increasing depth (i.e., density), so interaction contributions have to be treated when evaluating MALs for deeper atmosphere regions. Furthermore, simple expressions for the cross sections as used here no longer apply and the different scattering processes have to be treated on the T matrix level by calculating the corresponding scattering phase shifts (see, e.g., [5,23–25,74]). It would also be interesting to study the influence of the magnetic field of the planet on the transport properties, in particular for the hot and dilute outer atmosphere (ionosphere). This is a subject left for future work.

The plasma is strongly coupled and degenerate in the deep interior of the planet, so first-principles approaches have to be applied in order to calculate the corresponding equation of state data, the ionization degree, and the transport properties. For instance, extensive molecular-dynamics simulations have been performed for the ions in dense H-He plasmas in combination with electronic structure calculations using density functional theory (density functional theory–based molecular-dynamics method). The corresponding results provide a reliable database to determine interior profiles for density, temperature, and pressure [75] and to simulate the dynamo process based on further material properties such as electrical and thermal conductivities [76,77] for Jupiter [78] and Jupiter-like planets. The deep interior, however, is not important for the study of Ohmic dissipation in the outer atmosphere, so the current results persist.

We have therefore used our results to predict the thermal and electrical conductivities for four different models proposed for the atmosphere of the hot Jupiter HD 209458b. The estimates suggest that the electrical conductivity is between one and two orders of magnitude lower than assumed by BS [11] in their study of Ohmic heating. While BS concluded that this additional heat source could explain the observed inflation of HD 209458b, our updated conductivities reduce the effect by up to three orders of magnitude and would make Ohmic heating too inefficient.

However, newer internal models [57] suggest significantly higher temperatures in the planet's atmosphere than assumed for these estimates. The resulting higher electrical conductivity would guarantee more than enough Ohmic heat to explain the inflation, even for our lower electrical conductivity values. The large uncertainties in the atmospheric temperature, but also in the planet's magnetic field strength [71], yet prevent us from giving reliable estimates of Ohmic heating in the atmosphere of HD 209458b.

Our estimates for the electric currents and thus for the Ohmic heating power largely follow simple scaling arguments based on previous attempts [11,72]. It would be interesting to run refined numerical models that solve for electrical currents using the updated conductivities proposed here. Because of the significant radial and dayside-to-nightside variation in temperature, the electrical conductivity will also have a three-dimensional field structure, making three-dimensional simulations essential. Repeating the simplified calculations by BS would be a first step. However, full magnetohydrodynamic simulations are required should the locally induced magnetic fields and associated Lorentz forces prove important.

ACKNOWLEDGMENTS

We thank Jan Maik Wissing for providing altitude data of the thermosphere and Nadine Nettelmann, Ludwig Scheibe, Martin Preising, and Clemens Kellermann for helpful discussions. This work was supported by the Deutsche Forschungsgemeinschaft within the Priority Program SPP 1992 "The Diversity of Exoplanets" and the Research Unit FOR 2440 "Matter under Planetary Interior Conditions."

[1] W. Ebeling, V. E. Fortov, Y. L. Klimontovich, N. P. Kovalenko, W. D. Kraeft, Y. P. Krasny, D. Kremp, P. P. Kulik, V. A. Riaby, G. Röpke, E. K. Rozanov, and M. Schlanges, *Transport Properties of Dense Plasmas* (Akademie-Verlag, Berlin, 1983).

[2] K. Günther and R. Radtke, *Electric Properties of Weakly Nonideal Plasmas* (Akademie-Verlag, Berlin, 1984).

[3] W.-D. Kraeft, D. Kremp, W. Ebeling, and G. Röpke, *Quantum Statistics of Charged Particle Systems* (Akademie-Verlag, Berlin, 1986).

[4] V. Fortov and I. Iakubov, *Physics of Nonideal Plasma* (Hemisphere, New York, 1990).

[5] R. Redmer, Phys. Rep. **282**, 35 (1997).

[6] A. Likalter, Phys. Scr. **55**, 114 (1997).

[7] A. A. Ovechkin, P. A. Loboda, and A. L. Falkov, High Energy Density Phys. **20**, 38 (2016).

[8] M. R. Zaghloul, Plasma Phys. Rep. **46**, 574 (2020).

[9] M.-B. Kallenrode, *Space Physics* (Springer, Berlin, 2001).

[10] J. M. Wissing and M.-B. Kallenrode, J. Geophys. Res. **114**, A06104 (2009).

[11] K. Batygin and D. J. Stevenson, Astrophys. J. Lett. **714**, L238 (2010).

[12] T. D. Komacek and A. N. Youdin, Astrophys. J. **844**, 94 (2017).

[13] N. Yoshida, K. Omukai, and L. Hernquist, Science **321**, 669 (2008).

[14] S.-I. Inutsuka, Prog. Theor. Exp. Phys. **2012**, 01A307 (2012).

[15] C. M. Franck and M. Seeger, Contrib. Plasma Phys. **46**, 787 (2006).

[16] X. Guo, X. Li, A. B. Murphy, and H. Zhao, J. Phys. D **50**, 345203 (2017).

[17] B. Pu and D. Valencia, Astrophys. J. **846**, 47 (2017).

[18] P. Sarkis, C. Mordasini, T. Henning, G. Marleau, and P. Molliere, Astron. Astrophys. **645**, A79 (2021).

[19] A. Burrows, I. Hubeny, J. Budaj, and W. B. Hubbard, Astrophys. J. **661**, 502 (2007).

[20] T. Rogers and A. Showman, Astrophys. J. Lett. **782**, L4 (2014).

[21] R. S. Freedman, M. S. Marley, and K. Lodders, Astrophys. J. Suppl. Ser. **174**, 504 (2008).

[22] R. Redmer, T. Rother, K. Schmidt, W. D. Kraeft, and G. Röpke, Contrib. Plasma Phys. **28**, 41 (1988).

[23] R. Redmer, Phys. Rev. E **59**, 1073 (1999).

[24] S. Kuhlbrodt and R. Redmer, Phys. Rev. E **62**, 7191 (2000).

[25] S. Kuhlbrodt, B. Holst, and R. Redmer, Contrib. Plasma Phys. **45**, 73 (2005).

[26] M. Schöttler, R. Redmer, and M. French, Contrib. Plasma Phys. **53**, 336 (2013).

[27] M. French and R. Redmer, Phys. Plasmas **24**, 092306 (2017).

[28] L. Spitzer and R. Härm, Phys. Rev. **89**, 977 (1953).

[29] H. Reinholz, G. Röpke, S. Rosmej, and R. Redmer, Phys. Rev. E **91**, 043105 (2015).

[30] M. P. Desjarlais, C. R. Scullard, L. X. Benedict, H. D. Whitley, and R. Redmer, Phys. Rev. E **95**, 033203 (2017).

[31] K. Behringer and N. van Cung, Appl. Phys. **22**, 373 (1980).

[32] K. Lodders, in *Lecture Notes of the Kodai School on Synthesis of Elements in Stars held at Kodaikanal Observatory, India, 2008*, edited by A. Goswami and B. E. Reddy (Springer, Heidelberg, 2010), pp. 379–417.

[33] K. Lodders, Astrophys. J. **591**, 1220 (2003).

[34] R. Pathria and P. D. Beale, in *Statistical Mechanics*, 3rd ed., edited by R. Pathria and P. D. Beale (Academic, Boston, 2011), pp. 141–178.

[35] A. Kramida, Y. Ralchenko, J. Reader, and NIST ASD Team, NIST Atomic Spectra Database, version 5.7.1, available at https://physics.nist.gov/asd, National Institute of Standards and Technology, Gaithersburg, 2019.

[36] F. Bošnjaković and K. F. Knoche, *Technische Thermodynamik: Teil I* (Steinkopff, Heidelberg, 1998).

[37] M. Schlanges, M. Bonitz, and A. Tschttschjan, Contrib. Plasma Phys. **35**, 109 (1995).

[38] Y. T. Lee and R. M. More, Phys. Fluids **27**, 1273 (1984).

[39] V. Imshennik, Sov. Astron. **5**, 495 (1962).

[40] H. Reinholz, R. Redmer, and D. Tamme, Contrib. Plasma Phys. **29**, 395 (1989).

[41] G. C. Maitland, M. Rigby, E. B. Smith, and W. A. Wakeham, *Intermolecular Forces: Their Origin and Determination*, International Series of Monographs on Chemistry Vol. 3 (Clarendon, Oxford, 1981).

[42] E. Mason and S. Saxena, Phys. Fluids **1**, 361 (1958).

[43] R. S. Brokaw, J. Chem. Phys. **29**, 391 (1958).

[44] M. P. Saksena and S. C. Saxena, Appl. Sci. Res. **17**, 326 (1967).

[45] R. S. Brokaw, J. Chem. Phys. **32**, 1005 (1960).

[46] J. N. Butler and R. S. Brokaw, J. Chem. Phys. **26**, 1636 (1957).

[47] H. Hanley, R. McCarty, and H. Intemann, J. Res. Natl. Bur. Stand. **74A**, 331 (1970).

[48] G. M. Kremer, *An Introduction to the Boltzmann Equation and Transport Processes in Gases* (Springer Science+Business Media, New York, 2010).

[49] J. O. Hirschfelder, C. F. Curtiss, R. B. Bird, and M. G. Mayer, *Molecular Theory of Gases and Liquids* (Wiley, New York, 1964), Vol. 165.

[50] J. P. Hansen and I. R. McDonald, *Theory of Simple Liquids* (Elsevier, Amsterdam, 1990).

[51] J. Vanderslice, S. Weissman, E. Mason, and R. Fallon, Phys. Fluids **5**, 155 (1962).

[52] R. Devoto and C. Li, J. Plasma Phys. **2**, 17 (1968).

[53] D. Charbonneau, T. M. Brown, D. W. Latham, and M. Mayor, Astrophys. J. **529**, L45 (2000).

[54] D. K. Sing, J. J. Fortney, N. Nikolov, H. R. Wakeford, T. Kataria, T. M. Evans, S. Aigrain, G. E. Ballester, A. S. Burrows, D. Deming, J. M. Désert, N. P. Gibson, G. W. Henry, C. M. Huitson, H. A. Knutson, A. L. D. Etangs, F. Pont, A. P. Showman, A. Vidal-Madjar, M. H. Williamson *et al.*, Nature (London) **529**, 59 (2016).

[55] A. J. Poser, N. Nettelmann, and R. Redmer, Atmosphere **10**, 664 (2019).

[56] T. Guillot, Astron. Astrophys. **520**, A27 (2010).

[57] M. R. Line, K. B. Stevenson, J. Bean, J.-M. Desert, J. J. Fortney, L. Kreidberg, N. Madhusudhan, A. P. Showman, and H. Diamond-Lowe, Astrophys. J. **152**, 203 (2016).

[58] D. S. Spiegel, K. Silverio, and A. Burrows, Astrophys. J. **699**, 1487 (2009).

[59] N. Nettelmann, J. J. Fortney, U. Kramm, and R. Redmer, Astrophys. J. **733**, 2 (2011).

[60] D. Saumon, G. Chabrier, and H. M. van Horn, Astrophys. J. Suppl. Ser. **99**, 713 (1995).

[61] W. B. Hubbard and M. S. Marley, Icarus **78**, 102 (1989).

[62] D. P. Thorngren and J. J. Fortney, Astrophys. J. **155**, 214 (2018).

[63] R. T. Zellem, N. K. Lewis, H. A. Knutson, C. A. Griffith, A. P. Showman, J. J. Fortney, N. B. Cowan, E. Agol, A. Burrows, D. Charbonneau, D. Deming, G. Laughlin, and J. Langton, Astrophys. J. **790**, 53 (2014).

[64] B. Drummond, E. Hébrard, N. J. Mayne, O. Venot, R. J. Ridgway, Q. Changeat, S.-M. Tsai, J. Manners, P. Tremblin, N. L. Abraham, D. Sing, and K. Kohary, Astron. Astrophys. **636**, A68 (2020).

[65] J. J. Fortney, K. Lodders, M. S. Marley, and R. S. Freedman, Astrophys. J. **678**, 1419 (2008).
[66] V. Parmentier and T. Guillot, Astron. Astrophys. **562**, A133 (2014).
[67] J. Liu, P. M. Goldreich, and D. J. Stevenson, Icarus **196**, 653 (2008).
[68] J. Wicht, T. Gastine, and L. D. V. Duarte, J. Geophys. Res.—Planets **124**, 837 (2019).
[69] R. Perna, K. Heng, and F. Pont, Astrophys. J. **751**, 59 (2012).
[70] I. A. G. Snellen, R. J. de Kok, E. J. W. de Mooij, and S. Albrecht, Nature (London) **465**, 1049 (2010).
[71] K. G. Kislyakova, M. Holmström, H. Lammer, P. Odert, and M. L. Khodachenko, Science **346**, 981 (2014).
[72] J. Wicht, T. Gastine, L. D. V. Duarte, and W. Dietrich, Astron. Astrophys. **629**, A125 (2019).
[73] X. Huang and A. Cumming, Astrophys. J. **757**, 47 (2012).
[74] J. R. Adams, H. Reinholz, and R. Redmer, Phys. Rev. E **81**, 036409 (2010).
[75] N. Nettelmann, B. Holst, A. Kietzmann, M. French, R. Redmer, and D. Blaschke, Astrophys. J. **683**, 1217 (2008).
[76] M. French, A. Becker, W. Lorenzen, N. Nettelmann, M. Bethkenhagen, J. Wicht, and R. Redmer, Astrophys. J. Suppl. Ser. **202**, 5 (2012).
[77] A. Becker, M. Bethkenhagen, C. Kellermann, J. Wicht, and R. Redmer, Astron. J. **156**, 149 (2018).
[78] T. Gastine, J. Wicht, L. D. V. Duarte, M. Heimpel, and A. Becker, Geophys. Res. Lett. **41**, 5410 (2014).

5.2 Electrical and thermal conductivity of fcc and hcp iron under conditions of the Earth's core from ab initio simulations

Author contributions

U. Kleinschmidt: Preparation of the manuscript, calculating the transport properties, analysis and interpretation of the results

M. French Supervision of the project, preparation of the manuscript

G. Steinle-Neumannn: Supervision of the project, preparation of the manuscript

R. Redmer: Supervision of the project, preparation of the manuscript

Electrical and thermal conductivity of fcc and hcp iron under conditions of the Earth's core from *ab initio* simulations

Uwe Kleinschmidt,[1] Martin French,[1] Gerd Steinle-Neumann,[2] and Ronald Redmer[1]
[1]*Universität Rostock, Institut für Physik, Albert-Einstein-Strasse 23-24, D-18059 Rostock, Germany*
[2]*Bayerisches Geoinstitut, Universität Bayreuth, D-95440 Bayreuth, Germany*

(Received 24 August 2022; revised 14 December 2022; accepted 9 February 2023; published 27 February 2023)

We use *ab initio* simulations based on density functional theory to calculate the electrical and thermal conductivity of solid iron in face-centered cubic and hexagonal phases at high pressures and temperatures up to Earth's core conditions. Both our electrical and thermal conductivities increase systematically with density and reasonably follow the Wiedemann-Franz law, in particular at low temperatures. A trend towards density-independent thermal conductivity observed in recent experiments is not supported by our calculations.

DOI: 10.1103/PhysRevB.107.085145

I. INTRODUCTION

The electrical and thermal conductivity of iron play an important role in the stability and evolution of planetary magnetic fields [1]. Liquid iron dominates the dynamo-active outer core in terrestrial planets, and solid phases in the inner core–at least for Earth and Mercury [2,3]–may influence the generation of magnetic fields [4]. At the high pressure (P) of planetary interiors, experiments show that close-packed phases exist along the melting curve, with the triple point between the face-centered cubic (fcc), the hexagonal close packed (hcp) phases, and the liquid located at $P = 90 - 110$ GPa and temperature $T = 2800 - 3400$ K [5–7]. Despite the lack of experiments indicating its presence [8,9] at conditions of the Earth's core ($P > 135$ GPa and $T \gtrsim 4000$ K [10]), the possible occurrence of the body-centered cubic (bcc) phase predicted by some molecular dynamics simulations [11] remains a topic of debate in mineral physics. However, the consideration of this phase is beyond the scope of the current manuscript.

The past decade has seen significant advances [12–14] in both experimental [15–20] and computational studies [21–31] on high-P conductivities of iron and some of its alloys, but no study has systematically investigated the effect of crystal structure on electronic transport; only the difference between the solid and liquid phases has been considered, for the systematic jump in electrical (σ) and thermal conductivity (λ) [21–23,28]. Here we compare σ and λ of the fcc and hcp phases and explore their anisotropy in the hcp phase. We do so by performing finite-temperature density functional theory (FT-DFT) calculations. This method allows for a description of the electronic and ionic structure of iron from first principles and has been successfully applied also to other metals, e.g., lithium [32], molybdenum [33], and aluminum [34,35].

II. THEORY AND METHODS

A. Density functional theory and molecular dynamics

We describe our system with a combination of FT-DFT [36–38] for the electrons and classical molecular dynamics (MD) for the atoms, based on the Born-Oppenheimer approximation [39], using the Vienna *Ab initio* Simulation Package (VASP) [40–42] in version 5.4.4. Electronic exchange and correlation (XC) effects are approximated with the functional of Perdew, Burke, and Ernzerhof (PBE) [43]. We use a projector augmented wave (PAW) potential [44–46] with 8 valence electrons ($[Ar]4s^1 3d^7$, PAW_PBE Fe_GW) for the electron-ion interaction, and a plane-wave cutoff of 1200 eV. The electronic wave functions are calculated at the Γ point for the hexagonal structure and at the Baldereschi mean value point [47] for fcc. For convenience, an orthorhombic supercell is used to describe the hexagonal structure [48], which yields equivalent results [49]. Temperature is controlled by a Nosé-Hoover thermostat [50,51]. All FT-DFT-MD simulations are performed with a time step of 2 fs and are run for 2–10 ps. Most of these numerical parameters were also used in previous work [29] and we confirm them to yield converged results. We run our simulations at densities $\rho = 9.00, 10.36, 12.00, 13.55$ g/cm^3 and $T = 1850, 3350, 4350, 6350$ K. We carefully monitor the structures through the pair distribution function during the MD simulations to see whether they remain solid and stay in the same symmetry.

Our present calculations exclusively employ the spin-degenerate version of DFT, and calculations in the liquid phase show that this approximation is physically reasonable at $P > 50$ GPa ($\rho \sim 9.5$ g/cm^3), where liquid iron loses its paramagnetic properties [29].

B. Electronic transport coefficients

From each of the equilibrated FT-DFT-MD simulations, we take 10–30 uncorrelated ionic configurations and run static FT-DFT calculations to compute the electronic transport properties, and average the results over configurations. We evaluate the following expressions for the Onsager coefficients derived from linear response

theory [52,53]:

$$L_n(\omega) = \frac{2\pi(-1)^n}{V\omega} \sum_{\mathbf{k}\nu\mu} \mathrm{Re}(\langle \mathbf{k}\nu|\hat{\mathbf{v}}|\mathbf{k}\mu\rangle \otimes \langle \mathbf{k}\mu|\hat{\mathbf{v}}|\mathbf{k}\nu\rangle) \times (f_{\mathbf{k}\nu} - f_{\mathbf{k}\mu}) \left(\frac{E_{\mathbf{k}\mu} + E_{\mathbf{k}\nu}}{2} - h_e\right)^n \times \delta(E_{\mathbf{k}\mu} - E_{\mathbf{k}\nu} - \hbar\omega), \quad (1)$$

with frequency ω, the reduced Planck constant $\hbar$, the volume of the simulation box V, the matrix elements $\langle \mathbf{k}\nu|\hat{\mathbf{v}}|\mathbf{k}\mu\rangle$ with the velocity operator $\hat{\mathbf{v}}$ and Bloch states $|\mathbf{k}\mu\rangle$, energy eigenvalue $E_{\mathbf{k}\mu}$, Fermi occupation number $f_{\mathbf{k}\mu}$ and the enthalpy per electron h_e. The matrix elements $\langle \mathbf{k}\nu|\hat{\mathbf{v}}|\mathbf{k}\mu\rangle$ are calculated from the dipole matrix elements $\langle \mathbf{k}\nu|\hat{\mathbf{r}}|\mathbf{k}\mu\rangle$[1] that take into account the nonlocal contributions from the PAW potentials and are implemented in the optical routines of VASP [53,54]. A Gaussian function is used to broaden the δ function to a small finite width.

The static electrical conductivity is given by

$$\sigma = e^2 \lim_{\omega\to 0} L_0(\omega), \quad (2)$$

where e is the elementary charge. The coefficient $L_0(\omega)$ is known as the ω-dependent Kubo-Greenwood formula [55,56]. The thermal conductivity reads

$$\lambda = \frac{1}{T} \lim_{\omega\to 0} \left(L_2(\omega) - L_1(\omega)L_0^{-1}(\omega)L_1(\omega)\right). \quad (3)$$

In practice, the static electrical and thermal conductivities are derived by linear extrapolations to $\omega = 0$ across an unphysical decrease at very small ω (Fig. 3 in the Supporting Online Material [57]).

The electrical and thermal conductivity are related by the Lorenz number, which is given by

$$L = \frac{\lambda}{T\sigma} \left(\frac{e}{k_B}\right)^2, \quad (4)$$

with the Boltzmann constant k_B. In the degenerate limit, the Wiedemann-Franz law [58,59] describes this ratio between λ and σ by the constant value of $\pi^2/3$ [60].

The static FT-DFT calculations are run with an energy cutoff of 400 eV [29] and several different Monkhorst-Pack **k**-point sets in the irreducible wedges of the Brillouin zones of the ideal crystalline supercells [61], similar to previous work [33,62]. Our convergence tests on particle number and **k** points (see Tables I-III in the Supporting Online Material [57]) show that it is necessary to consider at least 288 atoms and a reduced wedge Monkhorst-Pack **k**-point set of $4 \times 4 \times 4$ in case of the hexagonal (orthorhombic) system and 256 atoms and a reduced wedge Monkhorst-Pack **k**-point set of $4 \times 4 \times 4$ for the fcc structure to get results for σ and λ that are converged to 1–6%, depending on density ρ and T. Further, we quantify the influence of the pseudopotential, which somewhat affects the ionic configurations generated from the FT-DFT-MD simulations and, consequently, conductivities in Figs. 1 and 2 of the Supporting Online Material [57]. Compared to a hard potential with 16 valence electrons, σ is lower by 5% compared to the 8-valence electron potential. Combining these accuracy assessments, we estimate an uncertainty of 10% for the calculated transport properties.

[1]This procedure is only applicable to the off-diagonal matrix elements. However, diagonal matrix elements (electron velocities) do not contribute in Eq. (1).

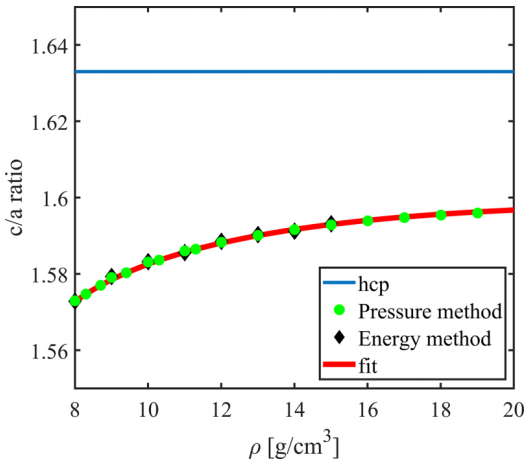

FIG. 1. Dependence of the c/a ratio in hexagonal iron on density at $T = 0$. DFT results are shown as green dots (pressure method) and black diamonds (energy method) compared to the ideal hcp ratio (blue line). Results are fitted (red) with an analytical function, Eq. (5).

C. Static DFT calculations for hexagonal iron

Before discussing the FT-DFT-MD simulations, we examine the equilibrium geometry of hexagonal iron at $T = 0$ with static DFT calculations. By adjusting the c/a ratio at given ρ until the diagonal elements of the pressure tensor are equal, we find hydrostatic ratios for densities between 4.35 and 26.5 g/cm^3, and test this approach by minimizing

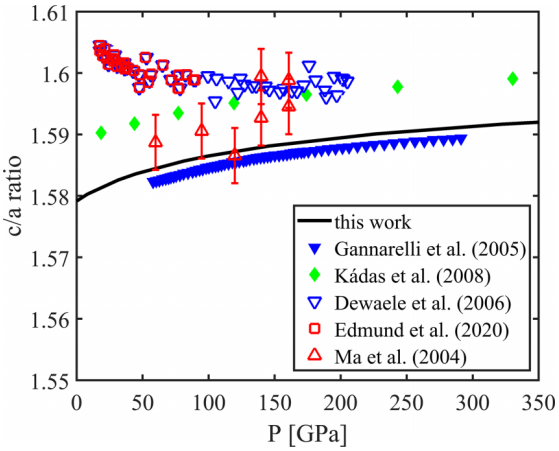

FIG. 2. Static c/a ratios of hexagonal iron calculated in the pressure range up to 350 GPa. Our results from Eq. (5) are shown as a black line, and compared to other DFT calculations by Gannarelli *et al.* [63] (blue triangles) and Kádas *et al.* [65] (green diamonds). Also shown are experimental data at room T by Dewaele *et al.* [66] (open blue triangles), Edmund *et al.* [67] (open red squares), and Ma *et al.* [68] (open red triangles).

TABLE I. Coefficients for Eq. (5).

b_0	b_1 [cm^3/g]	b_2 [(cm^3/g)^2]	b_3 [(cm^3/g)^3]	b_4 [(cm^3/g)^4]
1.591	0.5813	−13.00	88.34	−246.10

total energy as a function of c/a at selected ρ. For these calculations we use a hexagonal cell with two atoms and a Monkhorst-Pack **k**-point mesh of 39 × 39 × 30 and an energy cutoff of 1200 eV, which is sufficient to converge all pressure tensor components.

III. RESULTS

A. c/a ratio at zero temperature

The hydrostatic c/a ratio at $T = 0$ is always smaller than the ideal hcp ratio of $\sqrt{8/3} \approx 1.633$ (Fig. 1). It decreases strongly toward low ρ and approaches a constant value of ∼1.60 for high ρ. Numerically, we fit our results to

$$\frac{c}{a}(\rho, T = 0) = b_0 + \frac{b_1}{\rho} + \frac{b_2}{\rho^2} + \frac{b_3}{\rho^3} + \frac{b_4}{\rho^4}, \qquad (5)$$

with coefficients given in Table I. Results from equalizing the components of the pressure tensor and minimizing energy are fully consistent.

In Fig. 2 we compare our c/a results to other DFT calculations and experimental data at room T. In the range $P = 0 - 350$ GPa, our results are in a good agreement with earlier DFT calculations by Gannarelli *et al.* [63], Steinle-Neumann *et al.* [64], and Kádas *et al.* [65], the latter with a small systematic deviation relative to the other results.

Figure 2 also shows measurements by Dewaele *et al.* [66], Edmund *et al.* [67], and Ma *et al.* [68] at room T, who provide results in the same P region as the DFT calculations. Differences of our results to experiments are likely due to the PBE approximation of the XC functional, assuming $T = 0$, and nuclear vibrational quantum effects not considered here.

In the following, we use the c/a ratio from Eq. (5) as a lower bound in our FT-DFT-MD simulations as the c/a ratio can be expected to increase with T and, possibly, approach the ideal hcp value. Experiments of Ma *et al.* [68] indicate that the T dependence of the c/a ratio is very weak up to 2750 K.

B. Pressure-temperature conditions

An analoguous determination of the hydrostatic c/a ratios for each ρ at various $T > 0$ would require a large amount of FT-DFT-MD simulations, which we did not attempt. Instead, we explore the sensitivity of conductivities on c/a by performing the calculations with three different ratios: The static value from Eq. (5), the ideal value of $c/a = \sqrt{8/3} \approx 1.633$, and $c/a = 1.61$, which lies in between.

Figure 3 shows the $P-T$ conditions generated in our simulations. All hexagonal and the fcc structures result in very similar P at given T and ρ, with differences <7%. For nonhydrostatic conditions, the average of the diagonal components of the pressure tensor is taken as total P.

As calculations with the PBE functional do not reproduce the experimental $P-\rho$ relation correctly, we add a P correction from Wagle and Steinle-Neumann [10] to mitigate this inaccuracy. This correction has a more pronounced effect for calculations at $\rho = 9$ g/cm^3, where the correction leads to $P = 9$ GPa compared to 12 GPa obtained directly from the simulations. For higher ρ, the P correction becomes smaller and is almost negligible for our highest ρ values, with 1 GPa on $P = 300$ GPa from FT-DFT-MD.

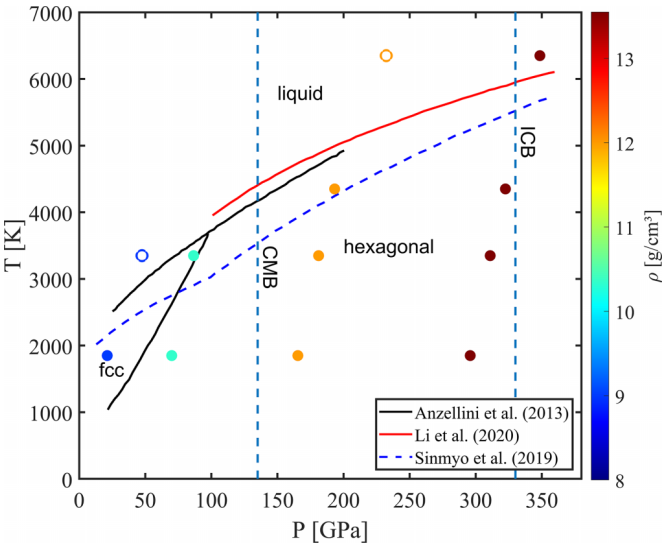

FIG. 3. Phase diagram of iron with phase boundaries given by Anzellini *et al.* [8], Li *et al.* [69], and Sinmyo *et al.* [9]. The symbols show the pressure-temperature conditions for the simulations we perform. Open circles indicate iron in the liquid phase, filled circles the hcp phase. Also shown are the pressures at the core-mantle (CMB) and inner core boundary (ICB) in Earth (dashed vertical lines).

The pair distribution function and particle diffusion reveals that the solid structures melt into the liquid state at two conditions ($\rho = 9$ g/cm^3, $T = 3350$ K and $\rho = 12$ g/cm^3, $T = 6350$ K), generally consistent with experimental melting curves (Fig. 3). Those simulations are excluded from further processing.

Based on a decrease of the pressure tensor anisotropy at higher c/a ratio for high T, we infer that the hydrostatic c/a ratio has to increase with T at given ρ. Nevertheless, the hydrostatic c/a ratios at arbitrary T fall between the value calculated for $T = 0$ (Fig. 1) and the ideal hcp value.

C. Conductivity anisotropy in hcp iron

Our computed electrical and thermal conductivity tensors show that they are relatively insensitive to the c/a ratio, especially for $T \geqslant 3350$ K (Tables IV and V in the Supporting Online Material [57]). Due to the small influence of c/a on conductivities, we continue the discussion exclusively for the conductivities of ideal hcp (Figs. 4 and 5). Because of the hexagonal symmetry, the xx and yy components of the conductivity tensors, i.e., in the basal plane (indexed with B) should be equal, which we observe within 4–5% for our orthorhombic supercells with 288 atoms (Tables I and II in the Supporting Online Material). This small deviation supports the good convergence with respect to **k** points and particle numbers in our calculations, and we take the mean values of the xx and yy components as σ_B and λ_B.

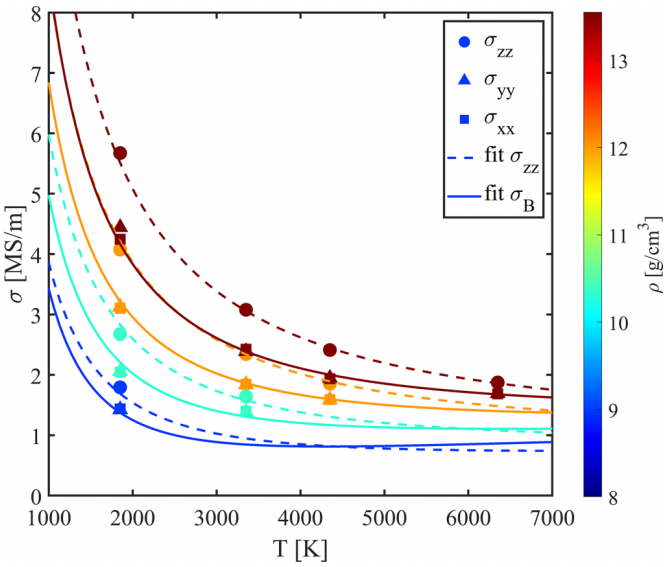

FIG. 4. Components of the electrical conductivity tensor for hcp Fe, σ_{xx} (squares), σ_{yy} (triangles), and σ_{zz} (circles), for different temperature and densities from simulations with 288 atoms. Also shown are fits for σ_{zz} (dashed lines) and σ_B (solid lines) using Eq. (6).

The zz component of σ and λ in the hexagonal phase is systematically larger by 3–33% than the basal component. The magnitude of the anisotropy decreases with T and almost vanishes at 6000 K. Anisotropy in conductivities for hcp iron has previously been reported by Xu *et al.* [27] and Ohta *et al.* [70]. Xu *et al.* [27] predicted $\sigma_{zz} > \sigma_{xx}$ with a combination of DFT and dynamical mean-field theory (DFT+DMFT) by a factor of 1.3, comparable to our results. Ohta *et al.* [70] measured $\lambda_{zz} > \lambda_B$ by a factor of 3–4 at room T, in line with the T trend of the anisotropy, although with a significantly larger value.

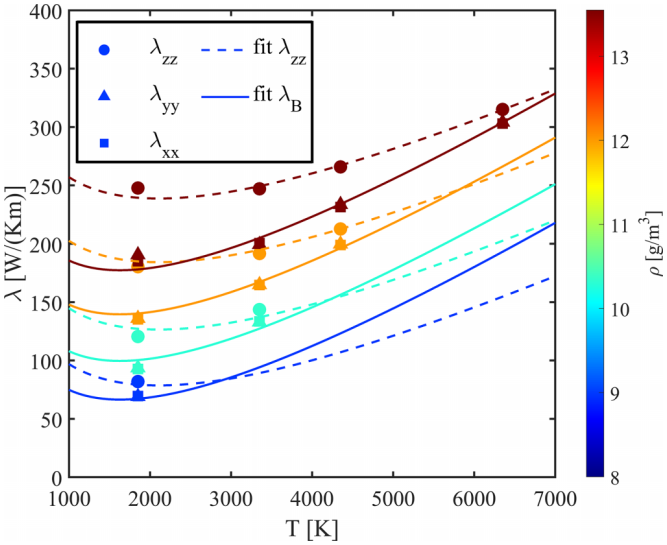

FIG. 5. Components of the thermal conductivity tensor for hcp Fe, λ_{xx} (squares), λ_{yy} (triangles), and λ_{zz} (circles), for different temperature and densities from simulations with 288 atoms. Also shown are fits for λ_{zz} (dashed lines) and λ_B (solid lines) using Eq. (7).

TABLE II. Coefficients for Eq. (6).

	$T\sigma_{\text{fcc}}$	$T\sigma_B$	$T\sigma_{zz}$
c_0 [MSK/m]	−2477	17490	7464
c_1 [SKm^2/g]	1434	1136	1555
c_2 [MS/m]	0.933	1.684	1.101
c_3 [MSK/m]	−1228	−3760	−2708

D. Comparison of hcp and fcc conductivities

Results for the basal plane B and zz components of σ and λ are used for analytical fits. The following expressions, which allowed for an accurate parametrization of FT-DFT-MD conductivity data for solid molybdenum [33], are used:

$$T\sigma_i = c_0 + c_1\rho + c_2 T + c_3 \ln T, \tag{6}$$

$$\lambda_i = d_0 + d_1\rho + d_2 T + d_3 \ln T. \tag{7}$$

Resulting coefficients are given in Tables II and III. Computed conductivities for fcc iron are processed the same way. These fit formulas are purely empirical and should not be extrapolated far beyond the underlying points used in the parametrization.

In Fig. 6 we show electrical conductivities in the fcc phase compared with the directionally averaged values for the hcp phase calculated via

$$\sigma_{\text{hcp}} = \tfrac{2}{3}\sigma_B + \tfrac{1}{3}\sigma_{zz}. \tag{8}$$

The electrical conductivity decreases with T and increases with ρ, and values for the fcc structure are larger than for hcp by up to ∼25%. Also shown are plots of the fit functions, Eq. (6), along isotherms which reproduce the numerical results very well.

For the thermal conductivity, averaging was done the same way as for σ, see Eq. (8), and results are shown in Fig. 7. The thermal conductivity increases with T and ρ for both structures, and–as for σ–the values in the fcc structure are systematically larger by up to ∼25%. The fit curves from Eq. (7) are in a good agreement with the computational results. Intersections between them at low T are probably artificial and should be viewed with caution.

E. Lorenz number

Figure 8 shows the Lorenz number calculated from Eq. (4) using our conductivity results. The Lorenz number of hcp and fcc iron decreases with P and increases with T. At low T the results for L become nearly constant and agree with the Wiedemann-Franz law [58,59] $L = \pi^2/3$, within few percent.

TABLE III. Coefficients for Eq. (7).

	λ_{fcc}	λ_B	λ_{zz}
d_0 [W/(Km)]	−137.1	373	315.8
d_1 [10^{-6}Wm^2/(gK)]	35.29	24.35	35.19
d_2 [W/(K^{2}m)]	0.02538	0.05051	0.03958
d_3 [W/(Km)]	−20.07	−82.2	−83.27

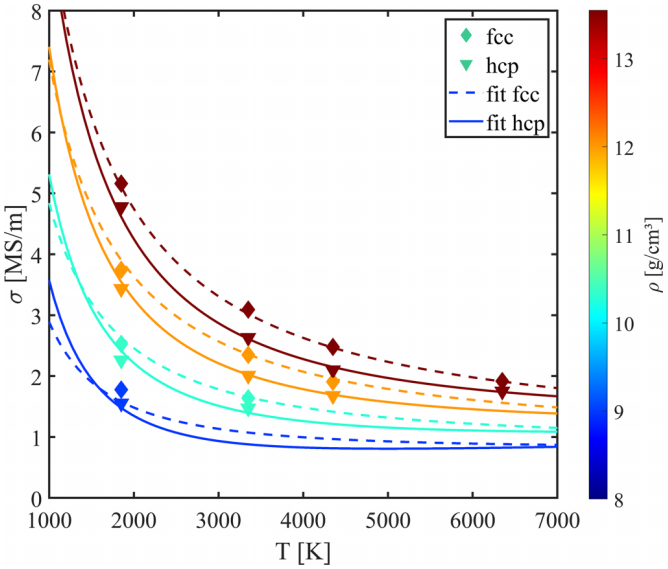

FIG. 6. Dependence of electrical conductivity on temperature for given densities for solid iron phases. Results for hcp Fe (triangles) are compared to those of the fcc phase (diamonds). Fits from Eq. (6) are shown as solid lines for hcp and dashed lines for fcc.

The T and P dependence of L is somewhat weaker for the fcc phase than for hcp. At high T, the Lorenz number shows significantly positive deviations from the Wiedemann-Franz law that can exceed 10%.

Within the adiabatic approximation, the Wiedemann-Franz law can be derived from kinetic theory for a fully degenerate electron gas, regardless of the scattering mechanisms of the electrons or complexity of electronic structure [60]. The deviations in our calculations likely arise from thermal electronic excitations and increasing lattice disorder in the ionic structure. They cannot be caused by electron-electron

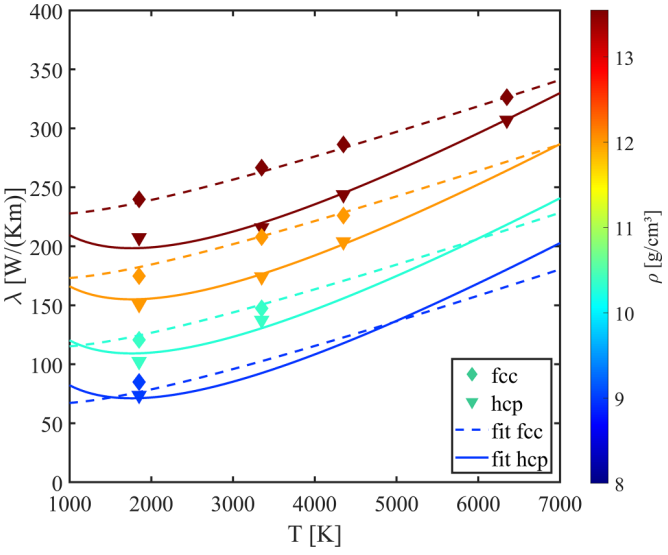

FIG. 7. Dependence of thermal conductivity on temperature for given densities for solid iron phases. Results for hcp Fe (triangles) are compared to that of the fcc phase (diamonds). Fits from Eq. (7) are shown as solid lines for hcp and dashed lines for fcc.

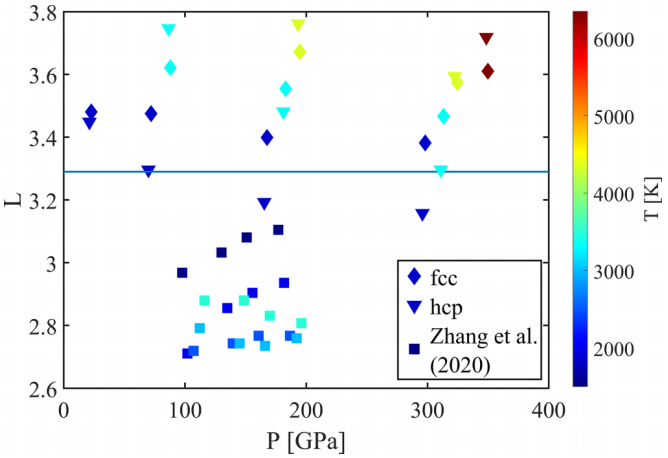

FIG. 8. Lorenz number for iron at high pressure and temperature. Our results for the hcp (triangles) and fcc (diamonds) phases are compared to those from Zhang *et al.* [20] for hcp iron (squares) using DFT+DMFT. The line indicates the degenerate limit $L = \pi^2/3$ from the Wiedemann-Franz law.

collisions, which our method does not account for as DFT represents a single-particle approximation of electrons [71]. Note that in liquid iron, where electrons are less degenerate, FT-DFT-MD calculations reproduce experimental data for σ and λ along a low-P isobar within 10%, while also closely following the Wiedemann-Franz law [29]. This suggests that electron-electron scattering is not an important process in iron at geophysical relevant conditions. Electron-electron scattering must not be confused with correlations among electrons, which are important and are approximated with the PBE XC functional used in our work.

IV. DISCUSSION

A. Comparison of conductivities with other computations and experiments

In Fig. 9, our FT-DFT-MD results for $\sigma_{\rm hcp}$ are compared to those of Pozzo *et al.* [23,24], who applied the same computational approach along two isochores. At $\rho = 10.36$ g/cm^3 ($P < 100$ GPa) our simulations reproduce the values of Pozzo and Alfè [24] very well. Larger systematic differences occur for $\rho = 13.55$ g/cm^3 (in the 300 GPa region), where both our P and conductivities are lower by 3–10%. While this is within the stated uncertainity of our results, the difference is systematic and warrants further consideration that may hint at possible causes:

(i) We find that the pressure tensor is not converged when using an energy cutoff of 293 eV as in Ref. [24].

(ii) In some cases we observe that if FT-DFT-MD simulations for hcp iron start with configurations too far from equilibrium, structural distortions of the lattice (especially in the third coordination shell) can occur, which then lead to inconsistent values in the pressure tensor, for σ, and for λ.

(iii) The extrapolation of $\sigma(\omega)$ to $\omega = 0$ may arrive at different results, with the linear extrapolation used here (Fig. 3 in the Supporting Online Material [57]) sometimes leading to larger values than a Drude fit used elsewhere [21].

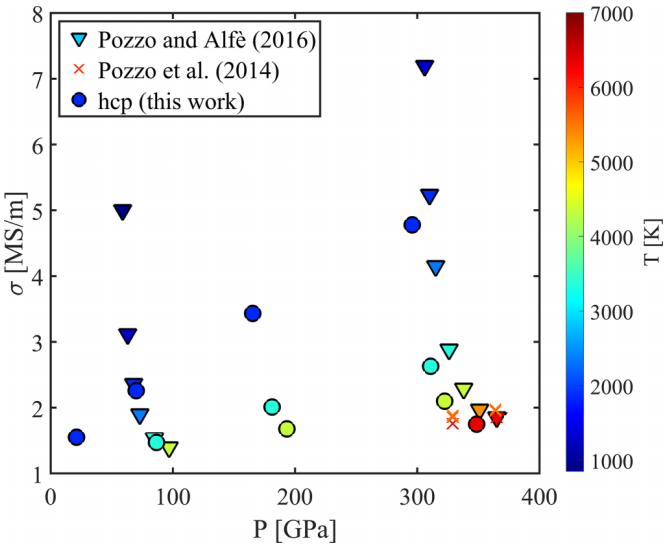

FIG. 9. Electrical conductivity of hcp iron as a function of pressure and temperature. Our results (circles) are compared to those from Pozzo *et al.* [23,24] (triangles and diamonds) in the same T and P range.

To compare our conductivity results to experimental data at arbitrary P and T, we use the Birch-Murnaghan equation of state for hcp iron by Belonoshko [73] to determine the P corresponding to our fit curves for $\sigma(\rho, T)$ and $\lambda(\rho, T)$. Resulting isothermal curves for the electrical and thermal conductivity as a function of P are compared with diamond anvil cells measurements in Figs. 10 and 11.

The electrical conductivity is compared to high-T experiments by Ohta *et al.* [17] and Zhang *et al.* [20], and a model resulting from experiments at room T by Gomi *et al.* [15] in Fig. 10. Both experimental and computed σ increase with P and decrease with T. The data of Zhang *et al.* [20] agree very well with our values at low P; however, they diverge for

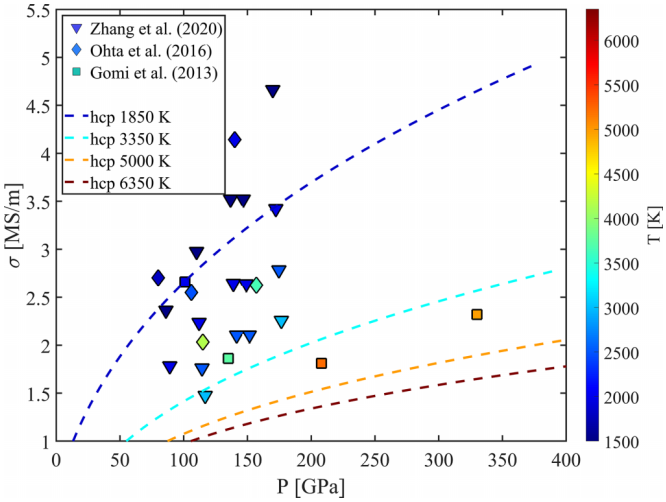

FIG. 10. Electrical conductivity of hcp iron as a function of pressure for given temperature. Our fit is shown as dashed lines for four isotherms and compared to experimental data of Zhang *et al.* [20] (triangles), Ohta *et al.* [17] (diamonds), and Gomi *et al.* [15] (squares).

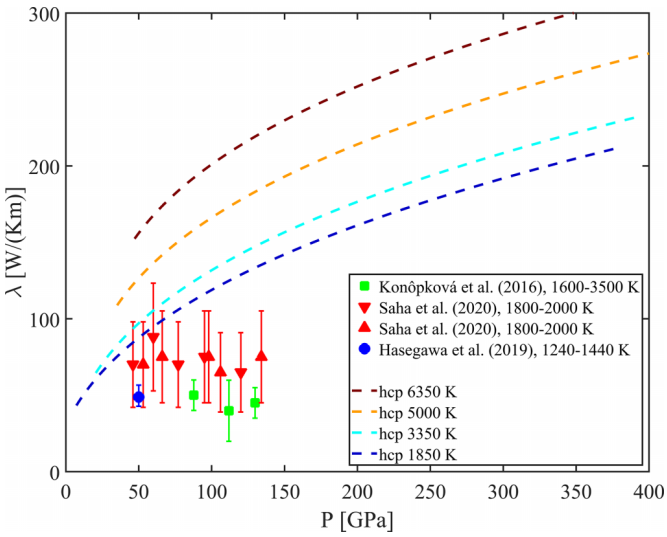

FIG. 11. Thermal conductivity of hcp iron as a function of pressure: Experimental data from Konôpková *et al.* [16] (green squares), Saha *et al.* [19] (red triangles: Upward for pressure transmitting medium NaCl and downward for pressure transmitting medium Al_2O_3), and Hasegawa *et al.* [18] (blue circle) are compared to the fit of our FT-DFT-MD results for hcp iron evaluated along four isotherms.

higher P as our σ rises much less steeply than theirs. Gomi *et al.* [15] tabulated values for σ at selected geophysically interesting points, like the core-mantle boundary (CMB) and inner core boundary (ICB). Their extrapolations to 101 GPa and 2010 K and the CMB (135 GPa and 3750 K) agree well with our isothermal model curves at 1850 K and 3350 K; larger deviations occur for high P and T extrapolations, at 208 GPa and 5220 K and P at the ICB (330 GPa and 4971 K). Values for σ by Ohta *et al.* [17] are significantly higher than ours for all P-T conditions of their experiments. Lobanov and Geballe [72] suggest that the large discrepancies between experimental results may originate from P-induced changes of sample geometry; they semiquantitatively reanalyzed experimental data by Ohta *et al.* [17] and Zhang *et al.* [20], and found that the discrepancy between the measurements decrease, as well as the difference between our results and experimental data.

The thermal conductivity is compared to experiments by Konôpková *et al.* [16], Saha *et al.* [19], and Hasegawa *et al.* [18] in Fig. 11. The values of Saha *et al.* [19] overlap with our curve for 1850 K at low P. Strangely, these measurements show no increase with P unlike our FT-DFT-MD results. This also applies to the measurements of Konôpková *et al.* [16], made for $T = 1600 - 3500$ K, which report much lower values than ours. The data from Hasegawa *et al.* [18] fall in the range of the other two experiments.

B. Lorenz number

A different P dependence for σ and λ would imply a P-dependent Lorenz number, Eq. (4), and consequently a strong departure from the Wiedemann-Franz law at higher P. Since our calculated σ and λ rise similarly with P, we do not observe a substantial P dependence of the Lorenz

number (Fig. 8). Further, measured values of $\sigma_{\rm hcp}$ are generally larger than the FT-DFT-MD results (Fig. 10), whereas the experiments on λ generally yield smaller values (Fig. 11), especially at $P > 100$ GPa. If these combined experimental trends are correct, a Lorenz number smaller by a factor of 2–3 than the Wiedemann-Franz limit of $L = \pi^2/3$ would follow. Such a large deviation would require a special theoretical explanation, especially as the degeneracy of electrons becomes stronger with P, which increasingly favors a Lorenz number *converging to* the Wiedemann-Franz limit, not *diverging from* it.

Zhang *et al.* [20] calculated the Lorenz number with DFT+DMFT using additional repulsive interaction energies between correlated electronic orbitals via Hubbard model parameters U and J that are chosen by external constraints [26,27]. This changes the electronic structure of iron compared to standard DFT calculations and influences σ and λ, also lowering the Lorenz number by up to 20% (Fig. 8). While the DFT+DMFT approach may offer an improved description of electronic correlations, it remains an open question whether it can properly describe electron-electron collisions as claimed previously [25–27]. Further, the DFT+DMFT method has not yet been benchmarked against experiments in the liquid phase [74–78]; neither has the high-T limit for which the exact limit for L that accounts for electron-electron scattering, known from Spitzer theory [71,79], been reproduced with the DFT+DMFT method.

C. Planetary implications

Assuming $T = 6350$ K at the ICB (330 GPa) [10,22], $\sigma = 1.65$ MS/m and $\lambda = 295$ W/(Km) for the hcp phase, making up the Earth's inner core, are juxtaposed with $\sigma = 1.60$ MS/m and $\lambda = 230$ W/(Km) for liquid iron [21], as a first-order approximation to the outer core. The small discontinuity (Δ) in σ between the solid and liquid is in line with systematic considerations by Wagle and Steinle-Neumann [28] based on the Ziman approximation, and slightly smaller than that estimated by Pozzo *et al.* [22–24] ($\Delta\sigma = 0.20$ MS/m). By contrast, the large difference in thermal conductivity with $\Delta\lambda = 70$ W/(Km) between the liquid and solid (with $\Delta\lambda = 90$ W/(Km) by Pozzo *et al.* [22–24] even larger) is of geophysical significance, with direct consequences on the thermal state and deformation regime of the inner core [80]. With a significantly larger value of λ in the inner core, a difference that will even increase [81] by the expulsion of light elements during its solidification from the outer core [80], the inner core is likely not in a convective regime as heat is conducted very efficiently along an adiabat, counteracting the buildup of a superadiabatic T profile that could form as a consequence of a thermal memory effect during its solidification history [82].

The presence of a significant amount of light elements [83] in the core of Mercury and limited knowledge of its internal structure [84,85] makes a similar comparison for the innermost planet in our solar system less meaningful. Nevertheless, at its central $P \sim 40$ GPa [83,86], with the melting point of Fe of ~2500 K [6], the fcc phase of iron coexists with the liquid, with values for $\sigma = 1.32$ MS/m (1.28 MS/m for the liquid [21]) and $\lambda = 90$ W/(Km) (75 W/(Km) for the liquid [21,28]), respectively. The jump in σ is comparable to that at ICB conditions in the Earth, and significantly smaller than that obtained by Wagle and Steinle-Neumann [28] ($\Delta\sigma = 0.18$ MS/m), putting the applicability of the Ziman approximation for iron at high P used in their work in question.

V. CONCLUSION

We have calculated the electrical σ and thermal conductivities λ of hexagonal and fcc iron at high pressures and temperatures from density functional theory. We show that for the hexagonal phase they display significant anisotropy that decreases with T, although the c/a ratio has little influence on calculated conductivities. Our results for the Lorenz number closely follow the Wiedemann-Franz law, in contrast to trends one may deduce from various recently performed experiments and computations that consider additional electronic repulsion (dynamic mean field theory). In particular, our calculated thermal conductivity is two times larger than experimental values and shows a linear increase with density. Our results for electrical conductivity are in good agreement with experiments at low T and P, but are smaller in the higher P–T region. These discrepancies need to be resolved by future experiments and further computations, possibly on other, simpler, metals. Finally, we provide convenient fit formulas for $\sigma(\rho, T)$ and $\lambda(\rho, T)$ for application in planetary science and comparison to experiments.

ACKNOWLEDGMENTS

We thank Stewart McWilliams for helpful discussions and Georg Kresse for providing us with the Fe_sv_h PAW potential. This work was supported by the Deutsche Forschungsgemeinschaft (DFG) within the Research Unit FOR 2440 and the Priority Program SPP 1992. The *ab initio* calculations were performed at the North-German Supercomputing Alliance (HLRN) facilities and at the IT and Media Center of the University of Rostock.

[1] C. Davies, M. Pozzo, D. Gubbins, and D. Alfè, Nature Geosci. **8**, 678 (2015).
[2] P. Cummins and L. R. Johnson, J. Geophys. Res. **93**, 9058 (1988).
[3] A. Genova, S. Goossens, E. Mazarico, F. G. Lemoine, G. A. Neumann, W. Kuang, T. J. Sabaka, S. A. Hauck II, D. E. Smith, S. C. Solomon, and M. T. Zuber, Geophys. Res. Lett. **46**, 3625 (2019).
[4] H. Amit and P. Olson, Earth Planet. Sci. Lett. **414**, 68 (2015).
[5] T. Komabayashi, Y. Fei, Y. Meng, and V. Prakapuka, Earth Planet. Sci. Lett. **282**, 252 (2009).
[6] T. Komabayashi, J. Geophys. Res. Solid Earth **119**, 4164 (2014).
[7] D. Zhang, J. M. Jackson, J. Zhao, W. Sturhahn, E. E. Alp, M. Y. Hu, T. S. Toellner, C. A. Murphy, and V. B. Prakapenka, Earth Planet. Sci. Lett. **447**, 72 (2016).

[8] S. Anzellini, A. Dewaele, M. Mezouar, P. Loubeyreand, and G. Morard, Science **340**, 464 (2013).
[9] R. Sinmyo, K. Hirose, and Y. Ohishi, Earth Planet. Sci. Lett. **510**, 45 (2019).
[10] F. Wagle and G. Steinle-Neumann, J. Geophys. Res. Solid Earth **124**, 3350 (2019).
[11] A. B. Belonoshko, T. Lukinov, J. Fu, J. Zhao, S. Davis, and S. I. Simak, Nat. Geosci. **10**, 312 (2017).
[12] M. Berrada, R. A. Secco, W. Yong, and J. A. H. Littleton, J. Geophys. Res. Planets **125**, e2020JE006380 (2020).
[13] M. Berrada, R. A. Secco, and W. Yong, Sci. Rep. **12**, 9941 (2022).
[14] Y. Yin, L. Wang, S. Zhai, and Y. Fei, J. Geophys. Res. Planets **127**, e2021JE007116 (2022).
[15] H. Gomi, K. Ohta, K. Hirose, S. Labrosse, R. Caracas, M. J. Verstraete, and J. W. Hernlund, Phys. Earth Planet. Inter. **224**, 88 (2013).
[16] Z. Konôpková, R. McWilliams, N. Gómez-Pérez, and A. F. Goncharov, Nature (London) **534**, 99 (2016).
[17] K. Ohta, Y. Kuwayama, K. Hirose, K Shimizu, and Y. Oshishi, Nature (London) **534**, 95 (2016).
[18] A. Hasegawa, T. Yagi, and K. Ohta, Rev. Sci. Instrum. **90**, 074901 (2019).
[19] P. Saha, A. Mazumder, and G. D. Mukherjee, Geosci. Front. **11**, 1755 (2020).
[20] Y. Zhang, M. Hou, G. Liu, C. Zhang, V. B. Prakapenka, E. Greenberg, Y. Fei, R. E. Cohen, and J.-F. Lin, Phys. Rev. Lett. **125**, 078501 (2020).
[21] N. de Koker, G. Steinle-Neumann, and V. Vlček, Natl. Acad. Sci. **109**, 4070 (2012).
[22] M. Pozzo, C. Davies, D. Gubbins, and D. Alfè, Nature (London) **485**, 355 (2012).
[23] M. Pozzo, C. Davies, D. Gubbins, and D. Alfè, Earth Planet. Sci. Lett. **393**, 159 (2014).
[24] M. Pozzo and D. Alfè, SpringerPlus **5**, 256 (2016).
[25] L. V. Pourovskii, J. Mravlje, A. Georges, S. I. Simak, and I. A. Abrikosov, New J. Phys. **19**, 073022 (2017).
[26] L. V. Pourovskii, J. Mravlje, M. Pozzo, and Alfè, Nat. Commun. **11**, 4105 (2020).
[27] J. Xu, P. Zhang, K. Haule, J. Minar, S. Wimmer, H. Ebert, and R. E. Cohen, Phys. Rev. Lett. **121**, 096601 (2018).
[28] F. Wagle and G. Steinle-Neumann, Geophys. J. Int. **213**, 237 (2018).
[29] J.A. Korell, M. French, G. Steinle-Neumann, and R. Redmer, Phys. Rev. Lett. **122**, 086601 (2019).
[30] M. Pozzo, C. Davies, D. Gubbins, and D. Alfè, Phys. Rev. B **87**, 014110 (2013).
[31] M. Pozzo, C. Davies, and D. Alfè, Earth Planet. Sci. Lett. **584**, 117466 (2022).
[32] A. Kietzmann, R. Redmer, M. P. Desjarlais, and T. R. Mattsson, Phys. Rev. Lett. **101**, 070401 (2008).
[33] M. French and T. R. Mattsson, Phys. Rev. B **90**, 165113 (2014).
[34] M. P. Desjarlais, J. D. Kress, and L. A. Collins, Phys. Rev. E **66**, 025401(R) (2002).
[35] B. B. L. Witte, M. Shihab, S. H. Glenzer, and R. Redmer, Phys. Rev. B **95**, 144105 (2017).
[36] P. Hohenberg and W. Kohn, Phys. Rev. **136**, B864 (1964).
[37] W. Kohn and L. J. Sham, Phys. Rev. **140**, A1133 (1965).
[38] N. D. Mermin, Phys. Rev. **137**, A1441 (1965).
[39] M. Born and R. Oppenheimer, Ann. Phys. **389**, 457 (1927).
[40] G. Kresse and J. Furthmüller, Phys. Rev. B **54**, 11169 (1996).
[41] G. Kresse and J. Hafner, Phys. Rev. B **47**, 558 (1993).
[42] G. Kresse and J. Hafner, Phys. Rev. B **49**, 14251 (1994).
[43] J. P. Perdew, K. Burke, and M. Ernzerhof, Phys. Rev. Lett. **77**, 3865 (1996).
[44] P. E. Blöchl, Phys. Rev. B **50**, 17953 (1994).
[45] G. Kresse and D. Joubert, Phys. Rev. B **59**, 1758 (1999).
[46] M. Valiev and J. H. Weare, J. Phys. Chem. A **103**, 10588 (1999).
[47] A. Baldereschi, Phys. Rev. B **7**, 5212 (1973).
[48] G. Steinle-Neumann, L. Stixrude, and R. E. Cohen, Proc. Natl. Acad. Sci. **101**, 33 (2004).
[49] C. X. Li, Key Eng. Mater. **837**, 146 (2020).
[50] S. Nosé, J. Chem. Phys. **81**, 511 (1984).
[51] W. G. Hoover, Phys. Rev. A **31**, 1695 (1985).
[52] B. Holst, M. French, and R. Redmer, Phys. Rev. B **83**, 235120 (2011).
[53] M. French and R. Redmer, Phys. Plasmas **24**, 092306 (2017).
[54] M. Gajdoš, K. Hummer, G. Kresse, J. Furthmüller, and F. Bechstedt, Phys. Rev. B **73**, 045112 (2006).
[55] R. Kubo, J. Phys. Soc. Jpn. **12**, 570 (1957).
[56] D. A. Greenwood, Proc. Phys. Soc. **71**, 585 (1958).
[57] See Supporting Material at http://link.aps.org/supplemental/10.1103/PhysRevB.107.085145 for convergence tables and additional figures.
[58] G. Wiedemann and R. Franz, Ann. Phys. **165**, 497 (1853).
[59] L. Lorenz, Ann. Phys. Chem. **223**, 429 (1872).
[60] A. Sommerfeld and H. Bethe, *Elektronentheorie der Metalle* (Springer, Berlin, 1967).
[61] H. J. Monkhorst and J. D. Pack, Phys. Rev. B **13**, 5188 (1976).
[62] D. Alfè, M. Pozzo, and M. P. Desjarlais, Phys. Rev. B **85**, 024102 (2012).
[63] C. M. S. Gannarelli, D. Alfè, and M. J. Gillan, Phys. Earth Planet. Inter. **152**, 67 (2005).
[64] G. Steinle-Neumann, L. Stixrude, and R. E. Cohen, Phys. Rev. B **60**, 791 (1999).
[65] K. Kádas, L. Vitos, and R. Ahuja, Earth Planet. Sci. Lett. **271**, 221 (2008).
[66] A. Dewaele, P. Loubeyre, F. Occelli, M. Mezouar, P. I. Dorogokupets, and M. Torrent, Phys. Rev. Lett. **97**, 215504 (2006).
[67] E. Edmund, F. Miozzi, G. Morard, E. Boulard, A. Clark, F. Decremps, G. Garbarino, V. Svitlyk, M. Mezouar, and D. Antonangeli, Minerals **10**, 98 (2020).
[68] Y. Ma, M. Somayazulu, G. Shen, H. Mao, J. Shu, and R. J. Hemley, Phys. Earth Planet. Inter. **143-144**, 455 (2004).
[69] J. Li, Q. Wu, J. Li, T. Xue, Y. Tan, X. Zhou, Y. Zhang, Z. Xiong, Z. Gao, and T. Sekine, Geophys. Res. Lett. **47**, e2020GL087758 (2020).
[70] K. Ohta, Y. Nishihara, Y. Sato, K. Hirose, T. Yagi, S. I. Kawaguchi, N. Hirao, and Y. Ohishi, Front. Earth Sci. **6**, 176 (2018).
[71] M. French, G. Röpke, M. Schörner, M. Bethkenhagen, M. P. Desjarlais, and R. Redmer, Phys. Rev. E **105**, 065204 (2022).
[72] S. S. Lobanov, Z. M. Geballe, Geophys. Res. Lett. **49**, e2022GL100379 (2022).
[73] A. B. Belonoshko, Condens. Matter Phys. **13**, 23605 (2010).
[74] J. B. van Zytveld, J. Phys. Colloques **41**, C8-503 (1980).
[75] R. S. Hixson, M. A. Winkler, and M. L. Hodgdon, Phys. Rev. B **42**, 6485 (1990).

[76] M. Beutl, G. Pottlacher, and H. Jäger, Int. J. Thermophys. **15**, 1323 (1994).
[77] K. C. Mills, B. J. Monaghan, and B. J. Keene, Int. Mater. Rev. **41**, 209 (1996).
[78] T. Nishi, H. Shibata, Y. Waseda, and H. Ohta, Metall. Mater. Trans. A **34**, 2801 (2003).
[79] L. Spitzer and R. Härm, Phys. Rev. **89**, 977 (1953).
[80] M. Lasbleis and R. Deguen, Phys. Earth Planet. Int. **247**, 80 (2015).
[81] F. Wagle, G. Steinle-Neumann, and N. de Koker, Comptes Rendus Geoscience **351**, 154 (2019).
[82] R. Deguen and P. Cardin, Geophys. J Int. **187**, 1101 (2011).
[83] A. Rivoldini, T. V. Hoolst, and O. Verhoeven, Icarus **201**, 12 (2009).
[84] I. Wardinski, H. Amit, B. Langlais, and E. Thébault, J. Geophys. Res. Planets **126**, e2020JE006792 (2021).
[85] A. Rivoldini and T. Van Hoolst, Earth Planet. Sci. Lett. **377-378**, 62 (2013).
[86] S. A. Hauck II, J.-L. Margot, S. C. Solomon, R. J. Phillips, C. L. Johnson, F. G. Lemoine, E. Mazarico, T. J. McCoy, S. Padovan, S. J. Peale, M. E. Perry, D. E. Smith, and M. T. Zuber, J. Geophys. Res. Planets **118**, 1204 (2013).

Supporting Online Material: Electrical and thermal conductivity of fcc and hcp iron under conditions of the Earth's core from ab initio simulations

Uwe Kleinschmidt[1], Martin French[1], Gerd Steinle-Neumann[2], and Ronald Redmer[1]
[1] *Universität Rostock, Institut für Physik, Albert-Einstein-Strasse 23-24, D-18059 Rostock, Germany*
[2] *Bayerisches Geoinstitut, Universität Bayreuth, D-95440 Bayreuth, Germany*

This material supplements the article "Electrical and thermal conductivity of fcc and hcp iron under conditions of the Earth's core from ab initio simulations" with tables and additional figures.

I. INFLUENCE OF THE PSEUDOPOTENTIAL ON THE CONDUCTIVITY

Here we present test calculations that quantify the influence of the pseudopotential on the DFT-MD simulations and the static linear-response DFT calculations at the two density-temperature conditions (Figs. 1 and 2).

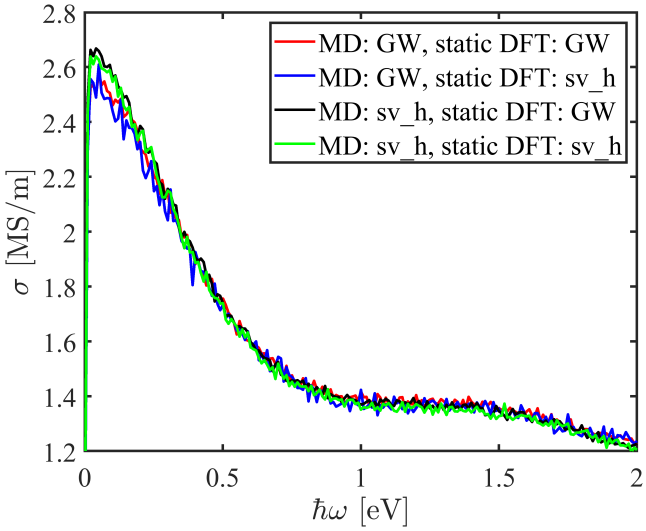

FIG. 1. Frequency-dependent electrical conductivity of fcc iron with $N = 108$ atoms at $\rho = 10.3$ g/cm^3 and $T = 1850$ K: The four combinations of using the potentials Fe_sv_h ([Ne]3s^{2}3p^{6}4s^{1}3d^7) and Fe_GW ([Ar]4s^{1}3d^7) in DFT-MD or the static linear-response DFT calculations to determine the electronic transport coefficients are shown.

The 16-valence electron potential (used with a cutoff energy of 1800 eV in the DFT-MD and 1200 eV in the static DFT calculations) yields essentially the same results in the linear-response DFT calculations as the 8-valence electron potential we use in our work. However, the choice of pseudopotential affects the ionic configurations generated in the DFT-MD simulations, which then leads to a higher DC conductivity in case of the 16-valence electron pseudopotential. At 10.3 g/cm^3 and 1850 K, DC conductivities are $\sigma_0 = 2.722$ MS/m (16 electrons) and $\sigma_0 = 2.593$ MS/m (8 electrons). At 13.55 g/cm^3 and 6350 K they are $\sigma_0 = 2.064$ MS/m (16 electrons) and $\sigma_0 = 1.974$ MS/m (8 electrons), respectively.

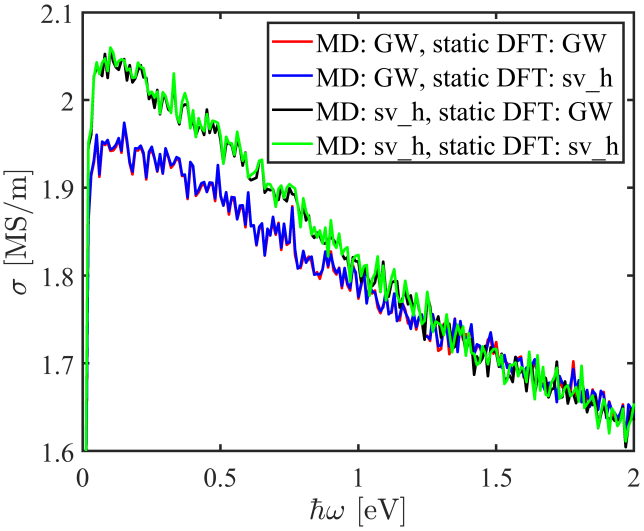

FIG. 2. Frequency-dependent electrical conductivity of fcc iron with $N = 108$ atoms at $\rho = 13.55$ g/cm^3 and $T = 6350$ K: The four combinations of using the potentials Fe_sv_h ([Ne]3s^{2}3p^{6}4s^{1}3d^7) and Fe_GW ([Ar]4s^{1}3d^7) in DFT-MD or the static linear-response DFT calculations to determine the electronic transport coefficients are shown.

II. EXTRAPOLATION TO ZERO FREQUENCY

The DC conductivity is derived by linear extrapolation to $\omega = 0$ across an unphysical decrease at very small ω. An example is shown in Fig. 3 for fcc iron at $\rho = 10.36$ g/cm^3 and $T = 1850$ K. The ω-range over which the unphysical decrease occurs shifts to smaller values for larger particle number. The interval in which a linear fit to σ appears reasonable also narrows with larger particle number and shifts to lower ω.

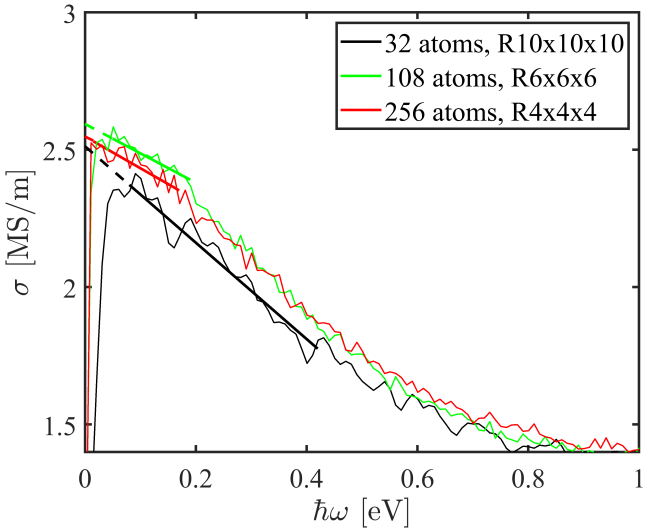

FIG. 3. Frequency-dependent electrical conductivity for fcc iron at $\rho = 10.36$ g/cm^3 and $T = 1850$ K for three different particle numbers and **k**-point sets. Also shown are the linear extrapolations to $\omega = 0$.

III. CONDUCTIVITY TABLES

TABLE I. Components of the electrical conductivity tensor and their directionally averaged values for the hcp structure at different temperatures, densities, number of atoms, and number of **k** points. The "R" in front of the **k**-point mesh indicates a Monkhorst-Pack **k**-point mesh in the reduced wedge. The given statistical uncertainty is from the 95% confidence interval of the linear regression.

T [K]	ρ [g/cm^3]	box continuation	N	**k** points	σ_{xx} [MS/m]	σ_{yy} [MS/m]	σ_{zz} [MS/m]	σ [MS/m]
1850	10.36	2×2×2	64	R3×3×3	2.179 ± 0.039	2.318 ± 0.033	3.056 ± 0.044	2.518 ± 0.029
1850	10.36	2×2×2	64	R4×4×4	2.298 ± 0.039	2.179 ± 0.033	2.780 ± 0.030	2.419 ± 0.022
1850	10.36	2×2×2	64	R5×5×5	2.318 ± 0.023	2.209 ± 0.018	2.877 ± 0.026	2.468 ± 0.018
1850	10.36	2×2×2	64	R6×6×6	2.332 ± 0.023	2.252 ± 0.012	2.830 ± 0.022	2.471 ± 0.016
1850	10.36	3×3×3	216	R3×3×3	2.012 ± 0.017	2.013 ± 0.017	2.544 ± 0.020	2.190 ± 0.014
1850	10.36	3×3×3	216	R4×4×4	1.957 ± 0.016	1.954 ± 0.027	2.442 ± 0.021	2.118 ± 0.016
1850	10.36	3×3×3	216	R6×6×6	2.001 ± 0.009	2.011 ± 0.011	2.498 ± 0.013	2.170 ± 0.009
1850	10.36	3×3×4	288	R4×4×4	2.043 ± 0.029	2.058 ± 0.019	2.676 ± 0.035	2.259 ± 0.024
1850	10.36	3×3×4	288	R6×6×6	2.059 ± 0.026	2.052 ± 0.020	2.646 ± 0.027	2.252 ± 0.021
1850	10.36	3×3×5	360	R4×4×4	2.081 ± 0.015	2.082 ± 0.027	2.591 ± 0.032	2.251 ± 0.019
1850	10.36	3×3×5	360	R6×6×6	2.080 ± 0.015	2.096 ± 0.021	2.594 ± 0.026	2.257 ± 0.016
1850	10.36	4×4×3	384	R4×4×4	2.123 ± 0.025	2.197 ± 0.021	2.633 ± 0.028	2.318 ± 0.018
1850	13.55	2×2×2	64	R3×3×3	3.973 ± 0.104	4.299 ± 0.131	6.663 ± 0.192	4.978 ± 0.112
1850	13.55	2×2×2	64	R4×4×4	4.581 ± 0.111	4.322 ± 0.088	5.279 ± 0.081	4.727 ± 0.055
1850	13.55	2×2×2	64	R5×5×5	4.484 ± 0.057	4.231 ± 0.061	5.583 ± 0.064	4.766 ± 0.055
1850	13.55	2×2×2	64	R6×6×6	4.635 ± 0.071	4.242 ± 0.041	5.372 ± 0.050	4.750 ± 0.048
1850	13.55	3×3×3	216	R3×3×3	4.097 ± 0.030	4.335 ± 0.045	5.421 ± 0.050	4.618 ± 0.032
1850	13.55	3×3×3	216	R4×4×4	4.109 ± 0.029	4.199 ± 0.039	5.151 ± 0.048	4.487 ± 0.033
1850	13.55	3×3×3	216	R6×6×6	4.175 ± 0.031	4.311 ± 0.028	5.088 ± 0.036	4.525 ± 0.029
1850	13.55	3×3×4	288	R4×4×4	4.245 ± 0.046	4.442 ± 0.039	5.673 ± 0.064	4.778 ± 0.038
1850	13.55	3×3×4	288	R6×6×6	4.291 ± 0.031	4.413 ± 0.034	5.642 ± 0.049	4.782 ± 0.035
1850	13.55	3×3×5	360	R4×4×4	4.431 ± 0.049	4.577 ± 0.066	5.808 ± 0.094	4.939 ± 0.057
1850	13.55	3×3×5	360	R6×6×6	4.498 ± 0.063	4.576 ± 0.057	5.723 ± 0.071	4.933 ± 0.060
1850	13.55	4×4×3	384	R4×4×4	4.436 ± 0.044	4.579 ± 0.051	5.274 ± 0.056	4.764 ± 0.042
3350	10.36	2×2×2	64	R3×3×3	1.455 ± 0.010	1.444 ± 0.011	1.713 ± 0.012	1.537 ± 0.007
3350	10.36	2×2×2	64	R4×4×4	1.467 ± 0.008	1.430 ± 0.008	1.704 ± 0.009	1.533 ± 0.005
3350	10.36	2×2×2	64	R5×5×5	1.467 ± 0.005	1.436 ± 0.005	1.711 ± 0.007	1.538 ± 0.003
3350	10.36	2×2×2	64	R6×6×6	1.465 ± 0.004	1.431 ± 0.005	1.705 ± 0.006	1.534 ± 0.004
3350	10.36	3×3×3	216	R3×3×3	1.389 ± 0.006	1.406 ± 0.005	1.597 ± 0.007	1.464 ± 0.004
3350	10.36	3×3×3	216	R4×4×4	1.391 ± 0.003	1.407 ± 0.004	1.600 ± 0.007	1.466 ± 0.003
3350	10.36	3×3×3	216	R6×6×6	1.391 ± 0.004	1.409 ± 0.004	1.601 ± 0.004	1.467 ± 0.003
3350	10.36	3×3×4	288	R4×4×4	1.400 ± 0.008	1.383 ± 0.006	1.641 ± 0.007	1.473 ± 0.004
3350	10.36	3×3×4	288	R6×6×6	1.402 ± 0.004	1.389 ± 0.005	1.640 ± 0.005	1.475 ± 0.003
3350	10.36	3×3×5	360	R4×4×4	1.402 ± 0.006	1.414 ± 0.007	1.660 ± 0.007	1.497 ± 0.006
3350	10.36	3×3×5	360	R6×6×6	1.398 ± 0.004	1.414 ± 0.003	1.644 ± 0.006	1.485 ± 0.003
3350	10.36	4×4×3	384	R4×4×4	1.383 ± 0.006	1.402 ± 0.005	1.640 ± 0.007	1.473 ± 0.004
6350	13.55	2×2×2	64	R3×3×3	1.770 ± 0.009	1.768 ± 0.008	1.832 ± 0.009	1.790 ± 0.006
6350	13.55	2×2×2	64	R4×4×4	1.777 ± 0.007	1.766 ± 0.006	1.827 ± 0.007	1.790 ± 0.004
6350	13.55	2×2×2	64	R5×5×5	1.780 ± 0.005	1.767 ± 0.005	1.829 ± 0.004	1.792 ± 0.003
6350	13.55	2×2×2	64	R6×6×6	1.778 ± 0.005	1.766 ± 0.004	1.823 ± 0.004	1.78 9± 0.003
6350	13.55	3×3×3	216	R3×3×3	1.667 ± 0.006	1.678 ± 0.006	1.853 ± 0.006	1.732 ± 0.004
6350	13.55	3×3×3	216	R4×4×4	1.673 ± 0.005	1.677 ± 0.005	1.852 ± 0.005	1.734 ± 0.003
6350	13.55	3×3×3	216	R6×6×6	1.665 ± 0.004	1.678 ± 0.003	1.851 ± 0.004	1.731 ± 0.003
6350	13.55	3×3×4	288	R4×4×4	1.684 ± 0.006	1.693 ± 0.006	1.873 ± 0.007	1.750 ± 0.004
6350	13.55	3×3×4	288	R6×6×6	1.686 ± 0.003	1.692 ± 0.003	1.871 ± 0.004	1.750 ± 0.002
6350	13.55	3×3×5	360	R4×4×4	1.667 ± 0.005	1.688 ± 0.005	1.844 ± 0.006	1.731 ± 0.004
6350	13.55	3×3×5	360	R6×6×6	1.664 ± 0.003	1.684 ± 0.004	1.831 ± 0.003	1.726 ± 0.003
6350	13.55	4×4×3	384	R4×4×4	1.685 ± 0.005	1.685 ± 0.006	1.821 ± 0.005	1.730 ± 0.004
1850	9	3×3×4	288	R4×4×4	1.437 ± 0.010	1.427 ± 0.011	1.793 ± 0.013	1.552 ± 0.008
1850	9	3×3×4	288	R6×6×6	1.434 ± 0.007	1.425 ± 0.007	1.794 ± 0.010	1.551 ± 0.007
1850	12	3×3×4	288	R4×4×4	3.102 ± 0.032	3.124 ± 0.035	4.073 ± 0.058	3.433 ± 0.036
1850	12	3×3×4	288	R6×6×6	3.128 ± 0.025	3.124 ± 0.028	4.060 ± 0.045	3.437 ± 0.030
3350	12	3×3×4	288	R4×4×4	1.844 ± 0.009	1.841 ± 0.010	2.344 ± 0.014	2.010 ± 0.008
3350	12	3×3×4	288	R6×6×6	1.853 ± 0.007	1.852 ± 0.007	2.352 ± 0.009	2.019 ± 0.006
3350	13.55	3×3×4	288	R4×4×4	2.425 ± 0.016	2.388 ± 0.016	3.077 ± 0.025	2.630 ± 0.016
3350	13.55	3×3×4	288	R6×6×6	2.415 ± 0.012	2.392 ± 0.014	3.079 ± 0.017	2.629 ± 0.013
4350	12	3×3×4	288	R4×4×4	1.591 ± 0.005	1.588 ± 0.004	1.851 ± 0.007	1.677 ± 0.005
4350	12	3×3×4	288	R6×6×6	1.587 ± 0.004	1.584 ± 0.004	1.845 ± 0.006	1.672 ± 0.003
4350	13.55	3×3×4	288	R4×4×4	1.935 ± 0.013	1.948 ± 0.020	2.412 ± 0.018	2.099 ± 0.010
4350	13.55	3×3×4	288	R6×6×6	1.938 ± 0.006	1.953 ± 0.006	2.416 ± 0.007	2.099 ± 0.005

TABLE II. Components of the thermal conductivity tensor and their directionally averaged values for the hcp structure at different temperatures, densities, number of atoms, and number of **k** points. The "R" in front of the **k**-point mesh indicates a Monkhorst-Pack **k**-point mesh in the reduced wedge. The given statistical uncertainty is from the 95% confidence interval of the linear regression.

T [K]	ρ [g/cm^3]	box continuation	N	**k** points	λ_{xx} [W/Km]	λ_{yy} [W/Km]	λ_{zz} [W/Km]	λ [W/Km]
1850	10.36	2×2×2	64	R3×3×3	106.1 ± 0.9	103.8 ± 0.9	114.3 ± 1.8	108.1 ± 0.8
1850	10.36	2×2×2	64	R4×4×4	103.2 ± 0.9	102.1 ± 0.8	126.7 ± 1.2	110.7 ± 0.6
1850	10.36	2×2×2	64	R5×5×5	102.5 ± 0.7	101.9 ± 0.8	124.4 ± 0.8	109.6 ± 0.6
1850	10.36	2×2×2	64	R6×6×6	102.6 ± 0.6	101.5 ± 0.6	124.1 ± 0.8	109.4 ± 0.5
1850	10.36	3×3×3	216	R3×3×3	89.87 ± 0.55	90.00 ± 0.36	113.0 ± 0.61	97.61 ± 0.32
1850	10.36	3×3×3	216	R4×4×4	89.60 ± 0.55	89.65 ± 0.51	112.1 ± 0.70	97.10 ± 0.42
1850	10.36	3×3×3	216	R6×6×6	89.79 ± 0.23	89.80 ± 0.27	112.7 ± 0.30	97.42 ± 0.17
1850	10.36	3×3×4	288	R4×4×4	92.80 ± 0.64	93.67 ± 1.06	120.6 ± 1.2	102.3 ± 0.7
1850	10.36	3×3×4	288	R6×6×6	92.80 ± 0.57	93.80 ± 0.83	120.7 ± 0.7	102.4 ± 0.6
1850	10.36	3×3×5	360	R4×4×4	93.86 ± 0.52	94.35 ± 1.21	117.4 ± 1.00	101.9 ± 0.8
1850	10.36	3×3×5	360	R6×6×6	94.02 ± 0.53	94.75 ± 0.47	117.4 ± 0.70	102.1 ± 0.5
1850	10.36	4×4×3	384	R4×4×4	97.00 ± 0.74	97.39 ± 0.61	119.2 ± 1.3	104.5 ± 0.6
1850	13.55	2×2×2	64	R3×3×3	202.5 ± 2.6	191.8 ± 3.5	221.2 ± 3.7	205.2 ± 2.6
1850	13.55	2×2×2	64	R4×4×4	204.7 ± 2.9	195.1 ± 2.0	233.9 ± 2.2	211.2 ± 1.7
1850	13.55	2×2×2	64	R5×5×5	203.7 ± 2.4	198.2 ± 2.0	245.9 ± 1.9	215.9 ± 2.0
1850	13.55	2×2×2	64	R6×6×6	208.8 ± 3.0	200.6 ± 2.6	227.9 ± 2.3	212.2 ± 2.3
1850	13.55	3×3×3	216	R3×3×3	177.2 ± 1.2	186.6 ± 1.5	226.1 ± 1.8	196.6 ± 1.2
1850	13.55	3×3×3	216	R4×4×4	182.2 ± 1.1	186.8 ± 1.2	221.9 ± 1.6	197.0 ± 1.1
1850	13.55	3×3×3	216	R6×6×6	179.2 ± 0.9	186.5 ± 1.1	225.5 ± 1.3	197.1 ± 1.0
1850	13.55	3×3×4	288	R4×4×4	185.0 ± 1.5	190.6 ± 1.9	247.7 ± 1.5	207.3 ± 1.4
1850	13.55	3×3×4	288	R6×6×6	182.4 ± 1.4	190.7 ± 1.5	249.3 ± 1.6	207.4 ± 1.4
1850	13.55	3×3×5	360	R4×4×4	196.4 ± 2.0	199.8 ± 2.1	253.6 ± 2.5	216.6 ± 1.8
1850	13.55	3×3×5	360	R6×6×6	193.3 ± 2.1	200.3 ± 2.3	251.7 ± 2.8	215.1 ± 2.3
1850	13.55	4×4×3	384	R4×4×4	189.2 ± 1.5	193.6 ± 1.5	224.6 ± 1.8	202.4 ±1.4
3350	10.36	2×2×2	64	R3×3×3	129.4 ± 1.4	135.3 ± 1.5	146.7 ± 1.7	137.1 ± 1.1
3350	10.36	2×2×2	64	R4×4×4	132.7 ± 1.2	130.3 ± 1.2	145.5 ± 1.2	136.1 ± 1.0
3350	10.36	2×2×2	64	R5×5×5	132.7 ± 0.9	133.3 ± 0.9	144.7 ± 0.9	136.9 ± 0.7
3350	10.36	2×2×2	64	R6×6×6	133.5 ± 0.7	133.1 ± 0.8	143.2 ± 0.8	136.6 ±0.6
3350	10.36	3×3×3	216	R3×3×3	132.1 ± 0.81	133.3 ± 1.1	139.3 ± 1.0	134.9 ± 0.71
3350	10.36	3×3×3	216	R4×4×4	132.0 ± 0.70	133.2 ± 0.7	139.9 ± 0.8	135.1 ± 0.60
3350	10.36	3×3×3	216	R6×6×6	132.0 ± 0.50	133.9 ± 0.6	139.7 ± 0.6	135.2 ± 0.40
3350	10.36	3×3×4	288	R4×4×4	133.5 ± 1.1	133.0 ± 1.1	143.6 ± 1.2	137.3 ± 0.9
3350	10.36	3×3×4	288	R6×6×6	134.1 ± 0.7	134.4 ± 0.7	144.1 ± 0.7	137.5 ± 0.6
3350	10.36	3×3×5	360	R4×4×4	134.9 ± 1.1	136.5 ± 1.3	145.5 ± 1.3	139.6 ± 1.1
3350	10.36	3×3×5	360	R6×6×6	135.5 ± 0.7	138.0 ± 1.0	145.6 ± 0.6	139.7 ± 0.6
3350	10.36	4×4×3	384	R4×4×4	133.7 ± 1.0	134.7 ± 0.8	143.0 ± 1.0	137.6 ± 0.8
6350	13.55	2×2×2	64	R3×3×3	287.1 ± 2.4	298.9 ± 2.0	297.5 ± 2.4	294.5 ± 1.7
6350	13.55	2×2×2	64	R4×4×4	300.1 ± 2.6	292.4 ± 2.7	296.0 ± 2.7	296.2 ± 2.1
6350	13.55	2×2×2	64	R5×5×5	299.8 ± 1.7	297.5 ± 2.0	295.6 ± 1.7	297.6 ± 1.4
6350	13.55	2×2×2	64	R6×6×6	300.0 ± 2.0	296.4 ± 2.0	291.3 ± 1.4	295.9 ± 1.5
6350	13.55	3×3×3	216	R3×3×3	300.3 ± 1.8	302.9 ± 1.7	309.5 ± 2.2	304.2 ± 1.5
6350	13.55	3×3×3	216	R4×4×4	302.1 ± 1.9	301.6 ± 1.8	310.2 ± 2.1	304.6 ± 1.5
6350	13.55	3×3×3	216	R6×6×6	300.6 ± 1.3	304.1 ± 1.1	309.2 ± 1.1	304.6 ± 0.8
6350	13.55	3×3×4	288	R4×4×4	302.9 ± 2.4	304.2 ± 1.8	315.1 ± 2.1	306.9 ± 1.6
6350	13.55	3×3×4	288	R6×6×6	301.7 ± 1.1	307.2 ± 1.6	315.2 ± 1.2	308.0 ± 1.0
6350	13.55	3×3×5	360	R4×4×4	300.6 ± 2.0	303.4 ± 2.3	309.5 ± 2.1	305.1 ± 1.7
6350	13.55	3×3×5	360	R6×6×6	297.9 ± 1.2	304.6 ± 1.3	307.0 ± 1.3	303.1 ± 1.0
6350	13.55	4×4×3	384	R4×4×4	298.6 ± 2.3	301.2 ± 1.9	306.8 ± 2.0	302.6 ± 1.7
1850	9	3×3×4	288	R4×4×4	69.55 ± 0.78	69.12 ± 0.66	81.95 ± 0.58	73.54 ± 0.48
1850	9	3×3×4	288	R6×6×6	69.34 ± 0.40	69.27 ± 0.51	81.47 ± 0.84	73.36 ± 0.39
1850	12	3×3×4	288	R4×4×4	135.3 ± 1.4	136.1 ± 1.2	180.3 ± 1.5	150.6 ± 1.1
1850	12	3×3×4	288	R6×6×6	133.7 ± 1.1	135.6 ± 0.9	181.1 ± 1.6	150.1 ± 1.1
3350	12	3×3×4	288	R4×4×4	164.7 ± 1.0	164.9 ± 1.2	191.6 ± 0.9	174.1 ± 0.8
3350	12	3×3×4	288	R6×6×6	164.6 ± 0.6	165.1 ± 0.7	192.2 ± 1.2	174.0 ± 0.7
3350	13.55	3×3×4	288	R4×4×4	200.6 ± 0.9	199.3 ± 0.7	247.1 ± 1.2	215.7 ± 0.6
3350	13.55	3×3×4	288	R6×6×6	200.1 ± 0.5	199.9 ± 0.5	247.2 ± 0.7	215.7 ± 0.4
4350	12	3×3×4	288	R4×4×4	198.9 ± 0.9	199.7 ± 0.8	212.7 ± 0.9	203.8 ± 0.6
4350	12	3×3×4	288	R6×6×6	198.3 ± 0.9	201.3 ± 1.0	211.4 ± 0.9	203.7 ± 0.7
4350	13.55	3×3×4	288	R4×4×4	231.5 ± 1.2	233.6 ± 0.9	265.9 ± 1.2	243.7 ± 0.9
4350	13.55	3×3×4	288	R6×6×6	231.2 ± 0.6	235.4 ± 0.8	265.7 ± 0.9	244.1 ± 0.6

TABLE III. Electrical and thermal conductivity for the fcc structure at different temperatures, densities, number of atoms, and number of **k** points. The "R" in front of the **k**-point mesh indicates a Monkhorst-Pack **k**-point mesh in the reduced wedge. The given statistical uncertainty is from the 95% confidence interval of the linear regression.

T [K]	ρ [g/cm^3]	box continuation	N	**k** points	σ [MS/m]	λ [W/Km]
1850	10.36	2×2×2	32	R2×2×2	2.465 ± 0.074	106.8 ± 2.6
1850	10.36	2×2×2	32	R4×4×4	2.420 ± 0.047	116.8 ± 2.6
1850	10.36	2×2×2	32	R6×6×6	2.491 ± 0.030	117.2± 1.5
1850	10.36	2×2×2	32	R8×8×8	2.512 ± 0.036	117.1 ± 1.6
1850	10.36	2×2×2	32	R10×10×10	2.493 ± 0.034	116.8 ± 1.4
1850	10.36	2×2×2	32	R12×12×12	2.510 ± 0.030	118.4 ± 1.4
1850	10.36	3×3×3	108	R2×2×2	2.532 ± 0.048	134.8 ± 2.3
1850	10.36	3×3×3	108	R4×4×4	2.655 ± 0.042	125.6 ± 1.4
1850	10.36	3×3×3	108	R6×6×6	2.593 ± 0.033	122.9 ± 1.5
1850	10.36	3×3×3	108	R8×8×8	2.621 ± 0.034	123.3 ± 1.5
1850	10.36	4×4×4	256	R2×2×2	2.551 ± 0.082	120.5 ± 1.3
1850	10.36	4×4×4	256	R4×4×4	2.528 ± 0.045	120.7 ± 1.6
1850	10.36	4×4×4	256	R6×6×6	2.530 ± 0.024	121.1 ± 1.0
1850	13.55	2×2×2	32	R2×2×2	4.200 ± 0.407	147.0 ± 7.7
1850	13.55	2×2×2	32	R4×4×4	4.688 ± 0.302	192.9 ± 6.3
1850	13.55	2×2×2	32	R6×6×6	4.293 ± 0.108	198.8 ± 3.8
1850	13.55	2×2×2	32	R8×8×8	4.286 ± 0.147	204.0 ± 3.2
1850	13.55	2×2×2	32	R10×10×10	4.154 ± 0.054	201.1 ± 1.5
1850	13.55	2×2×2	32	R12×12×12	4.195 ± 0.086	202.0 ± 2.8
1850	13.55	3×3×3	108	R2×2×2	4.959 ± 0.134	260.2 ± 6.2
1850	13.55	3×3×3	108	R4×4×4	5.190 ± 0.270	239.8 ± 9.8
1850	13.55	3×3×3	108	R6×6×6	5.135 ± 0.110	239.0 ± 5.7
1850	13.55	3×3×3	108	R8×8×8	5.156 ± 0.088	240.3 ± 2.7
1850	13.55	4×4×4	256	R2×2×2	5.366 ± 0.180	236.2 ± 5.0
1850	13.55	4×4×4	256	R4×4×4	5.161 ± 0.139	239.8 ± 2.5
1850	13.55	4×4×4	256	R6×6×6	5.137 ± 0.059	239.6 ± 3.4
3350	10.36	2×2×2	32	R2×2×2	1.676 ± 0.035	143.8 ± 2.5
3350	10.36	2×2×2	32	R4×4×4	1.724 ± 0.022	141.2 ± 1.5
3350	10.36	2×2×2	32	R6×6×6	1.728 ± 0.014	145.3 ± 1.6
3350	10.36	2×2×2	32	R8×8×8	1.743 ± 0.011	144.5 ± 1.9
3350	10.36	2×2×2	32	R10×10×10	1.736 ± 0.009	143.4 ± 1.8
3350	10.36	2×2×2	32	R12×12×12	1.755 ± 0.008	145.2 ± 2.0
3350	10.36	3×3×3	108	R2×2×2	1.754 ± 0.020	151.3 ± 4.2
3350	10.36	3×3×3	108	R4×4×4	1.676 ± 0.025	152.0 ± 2.1
3350	10.36	3×3×3	108	R6×6×6	1.704 ± 0.021	152.0 ± 1.1
3350	10.36	3×3×3	108	R8×8×8	1.710 ± 0.013	152.2 ± 1.0
3350	10.36	4×4×4	256	R2×2×2	1.652 ± 0.026	144.8 ± 2.1
3350	10.36	4×4×4	256	R4×4×4	1.636 ± 0.014	147.4 ± 1.4
3350	10.36	4×4×4	256	R6×6×6	1.639 ± 0.009	146.9 ± 0.8
3350	10.36	5×5×5	500	R2×2×2	1.673 ± 0.029	152.9 ± 1.8
3350	10.36	5×5×5	500	R4×4×4	1.685 ± 0.017	152.8 ± 1.1
6350	13.55	2×2×2	32	R2×2×2	2.115 ± 0.160	319.1 ± 6.1
6350	13.55	2×2×2	32	R4×4×4	2.060 ± 0.022	318.8 ± 3.4
6350	13.55	2×2×2	32	R6×6×6	2.052 ± 0.016	315.5 ± 2.8
6350	13.55	2×2×2	32	R8×8×8	2.074 ± 0.014	319.4 ± 1.7
6350	13.55	2×2×2	32	R10×10×10	2.051 ± 0.016	316.9 ± 1.9
6350	13.55	2×2×2	32	R12×12×12	2.073 ± 0.017	319.1 ± 2.1
6350	13.55	3×3×3	108	R2×2×2	1.989 ± 0.016	326.3 ± 5.1
6350	13.55	3×3×3	108	R4×4×4	1.980 ± 0.008	332.8 ± 4.1
6350	13.55	3×3×3	108	R6×6×6	1.974 ± 0.007	327.8 ± 2.2
6350	13.55	3×3×3	108	R8×8×8	1.985 ± 0.006	329.2 ± 1.6
6350	13.55	4×4×4	256	R2×2×2	1.931 ± 0.014	326.0 ± 3.6
6350	13.55	4×4×4	256	R4×4×4	1.917 ± 0.007	326.4 ± 1.9
6350	13.55	4×4×4	256	R6×6×6	1.918 ± 0.004	326.6 ± 2.3
1850	9.0	4×4×4	256	R4×4×4	1.777 ± 0.021	84.98 ± 0.53
1850	12.0	4×4×4	256	R4×4×4	3.743 ± 0.058	174.8 ± 2.5
3350	12.0	4×4×4	256	R4×4×4	2.350 ± 0.015	207.8 ± 1.6
3350	13.55	4×4×4	256	R4×4×4	3.092 ± 0.033	266.7 ± 1.9
4350	12.0	4×4×4	256	R4×4×4	1.905 ± 0.015	226.0 ± 1.5
4350	13.55	4×4×4	256	R4×4×4	2.479 ± 0.022	286.3 ± 1.1

TABLE IV. Components of the electrical conductivity tensor and their directionally averaged values for three c/a-ratios at different temperatures and densities calculated with 216 atoms and a **k**-point mesh of R4×4×4. The "R" in front of the **k**-point mesh indicates a Monkhorst-Pack **k**-point mesh in the reduced wedge. The given statistical uncertainty is from the 95% confidence interval of the linear regression.

T [K]	ρ [g/cm^3]	c/a-ratio	N	**k** points	σ_{xx} [MS/m]	σ_{yy} [MS/m]	σ_{zz} [MS/m]	σ [MS/m]
1850	10.36	hcp	216	R4×4×4	1.987 ± 0.011	1.995 ± 0.016	2.473 ± 0.014	2.152 ± 0.012
1850	10.36	1.61	216	R4×4×4	2.006 ± 0.011	2.045 ± 0.013	2.538 ± 0.013	2.196 ± 0.010
1850	10.36	1.584	216	R4×4×4	2.029 ± 0.015	2.098 ± 0.015	2.554 ± 0.017	2.227 ± 0.013
1850	13.55	hcp	216	R4×4×4	4.109 ± 0.029	4.199 ± 0.039	5.151 ± 0.048	4.487 ± 0.033
1850	13.55	1.61	216	R4×4×4	3.954 ± 0.039	4.054 ± 0.039	5.094 ± 0.052	4.367 ± 0.035
1850	13.55	1.591	216	R4×4×4	4.227 ± 0.034	4.347 ± 0.039	5.227 ± 0.051	4.600 ± 0.030
3350	10.36	hcp	216	R4×4×4	1.391 ± 0.003	1.407 ± 0.004	1.600 ± 0.007	1.466 ± 0.003
3350	10.36	1.61	216	R4×4×4	1.383 ± 0.005	1.397 ± 0.006	1.597 ± 0.007	1.459 ± 0.004
3350	10.36	1.584	216	R4×4×4	1.383 ± 0.005	1.379 ± 0.005	1.624 ± 0.006	1.462 ± 0.004
6350	13.55	hcp	216	R4×4×4	1.673 ± 0.005	1.677 ± 0.005	1.852 ± 0.005	1.734 ± 0.003
6350	13.55	1.61	216	R4×4×4	1.660 ± 0.004	1.660 ± 0.004	1.852 ± 0.004	1.724 ± 0.002
6350	13.55	1.591	216	R4×4×4	1.656 ± 0.006	1.656 ± 0.004	1.838 ± 0.006	1.717 ± 0.004

TABLE V. Components of the thermal conductivity tensor and their directionally averaged values for three c/a-ratios at different temperatures and densities calculated with 216 atoms and a **k**-point mesh of R4×4×4. The "R" in front of the **k**-point mesh indicates a Monkhorst-Pack **k**-point mesh in the reduced wedge. The given statistical uncertainty is from the 95% confidence interval of the linear regression.

T [K]	ρ [g/cm^3]	c/a-ratio	N	**k** points	λ_{xx} [W/Km]	λ_{yy} [W/Km]	λ_{zz} [W/Km]	λ [W/Km]
1850	10.36	hcp	216	R4×4×4	90.07 ± 0.45	90.15 ± 0.44	113.1 ± 0.60	97.77 ± 0.35
1850	10.36	1.61	216	R4×4×4	89.69 ± 0.35	91.52 ± 0.53	114.9 ± 0.50	98.71 ± 0.31
1850	10.36	1.584	216	R4×4×4	90.44 ± 0.27	92.69 ± 0.50	113.5 ± 0.50	98.88 ± 0.28
1850	13.55	hcp	216	R4×4×4	182.2 ± 1.1	186.8 ± 1.2	221.9 ± 1.6	197.0 ± 1.1
1850	13.55	1.61	216	R4×4×4	176.9 ± 1.5	178.1 ± 1.3	215.4 ± 1.1	190.2 ± 1.0
1850	13.55	1.591	216	R4×4×4	189.5 ± 1.1	192.9 ± 0.7	223.8 ± 1.5	202.1 ± 0.9
3350	10.36	hcp	216	R4×4×4	132.0 ± 0.70	133.2 ± 0.7	139.9 ± 0.8	135.1 ± 0.60
3350	10.36	1.61	216	R4×4×4	131.0 ± 0.90	132.8 ± 1.1	141.6 ± 1.2	135.1 ± 0.80
3350	10.36	1.584	216	R4×4×4	132.0 ± 0.70	131.7 ± 0.8	143.5 ± 0.9	135.7 ± 0.70
6350	13.55	hcp	216	R4×4×4	302.1 ± 1.9	301.6 ± 1.8	310.2 ± 2.1	304.6 ± 1.5
6350	13.55	1.61	216	R4×4×4	299.4 ± 1.7	299.2 ± 1.8	312.0 ± 1.9	303.5 ± 1.4
6350	13.55	1.591	216	R4×4×4	295.9 ± 1.7	296.6 ± 2.1	308.1 ± 1.6	300.2 ± 1.4

5.3 A conductivity model for hydrogen based on ab initio simulations

Author contributions

U. Kleinschmidt: Preparation of the manuscript, calculating the transport properties, analysis and interpretation of the results, development of the new conductivity model

R. Redmer: Supervision of the project, preparation of the manuscript

RESEARCH ARTICLE | MAY 05 2025

A conductivity model for hydrogen based on *ab initio* simulations

Special Collection: Special Issue on ICMRE2024

Uwe Kleinschmidt ; Ronald Redmer

Matter Radiat. Extremes 10, 047602 (2025)
https://doi.org/10.1063/5.0250970

Matter and Radiation at Extremes

RESEARCH ARTICLE

pubs.aip.org/aip/mre

A conductivity model for hydrogen based on *ab initio* simulations

Cite as: Matter Radiat. Extremes 10, 047602 (2025); doi: 10.1063/5.0250970
Submitted: 28 November 2024 • Accepted: 13 April 2025 •
Published Online: 5 May 2025

Uwe Kleinschmidt[a] and Ronald Redmer

AFFILIATIONS

Institut für Physik, Universität Rostock, Albert-Einstein-Strasse 23-24, D-18059 Rostock, Germany

Note: This paper is part of the Special Issue on the 7th International Conference on Matter and Radiation at Extremes (ICMRE2024).
[a]Author to whom correspondence should be addressed: uwe.kleinschmidt@uni-rostock.de

ABSTRACT

We calculate the electrical and thermal conductivity of hydrogen for a wide range of densities and temperatures by using molecular dynamics simulations informed by density functional theory. On the basis of the corresponding extended *ab initio* data set, we construct interpolation formulas covering the range from low-density, high-temperature to high-density, low-temperature plasmas. Our conductivity model reproduces the well-known limits of the Spitzer and Ziman theory. We compare with available experimental data and find very good agreement. The new conductivity model can be applied, for example, in dynamo simulations for magnetic field generation in gas giant planets, brown dwarfs, and stellar envelopes.

I. INTRODUCTION

Knowledge of the thermodynamic, transport, and optical properties of warm dense matter (WDM) is of outstanding importance for planetary science.[1] However, a dense plasma (or WDM) under planetary interior conditions is strongly correlated and degenerate, and so simple models to calculate these properties fail. Therefore, material properties need to be determined preferably on the basis of *ab initio* simulations by using, for example, density functional theory (DFT) for the electrons coupled to classical molecular dynamics (MD) for the ions. This complex program has been executed recently, for example, along the pressure–temperature–density (P–T–ρ) profiles for the interior of Jupiter,[2] Saturn,[3] and brown dwarfs[4] via large-scale DFT-MD simulations. Other extensive *ab initio* calculations have been performed for warm and hot dense matter, with the aims, for example, of generating an equation-of-state table of deuterium for inertial confinement fusion applications[5] and of providing a so-called first-principles equation-of-state (FP-EOS) collection for a number of elements and compounds.[6]

Space missions such as Voyager and Galileo, the recent Cassini–Huygens mission to Saturn that ended in 2017, and the Juno spacecraft still orbiting Jupiter have provided a wealth of new insights into the properties of the gas giants in our solar system. In particular, gravity data of so far unprecedented accuracy have revolutionized our understanding of the interiors of Jupiter[7] and Saturn,[8] which is intimately connected with models for the formation and thermal evolution of these planets. For instance, there is now clear evidence for the existence of inhomogeneous regions in these interiors, which result from hydrogen–helium demixing on the one hand and dissolution of higher-Z material contained in the core region into the mantle of metallic hydrogen on the other.[1] As well as a more detailed picture of the interior structure, advanced models of the dynamo action in the deeper layers that generates Jupiter's magnetic field[9] and of the zonal wind patterns[10] have been established on the basis of the Juno data.[11–13]

Measuring material properties such as electrical and thermal conductivity and the viscosity of matter under such extreme conditions remains a great challenge for experimental high-pressure physics. Nevertheless, these quantities are an essential input into magnetohydrodynamic simulations describing the dynamo action in the deep interior of gas giants, i.e., the generation and evolution of their magnetic fields.[14–17] These data are also important when calculating the influence of Ohmic dissipation by deep-seated zonal winds in the outer atmospheres of hot Jupiters.[18–20]

Therefore, numerous *ab initio* studies have been performed in the last decade to calculate material properties under such extreme conditions for the most abundant elements hydrogen and helium (see, e.g., Refs. 2–6 and 21–24). Comprehensive reviews of the properties of warm dense hydrogen and helium have been provided by McMahon *et al.*[25] and Bonitz *et al.*[26]

The transport properties of fully ionized hydrogen plasmas have been calculated for a wide range of densities and temperatures, in particular in the context of studies of stellar structure and evolution (see, e.g., Refs. 27–30). To save computational costs, the development of elaborate *conductivity models* applicable to plasmas in a wide range of density and temperature is a very important task. These models should reproduce the known limiting cases: the Spitzer theory[31] for low densities and high temperatures and the Ziman formula[32] for high densities and low temperatures. Conductivity models include free parameters that are usually adjusted with reference to available theoretical and experimental data so that they can be applied for arbitrary densities and temperatures.

A well-known example is the quantum-statistical approach of Ichimaru and Tanaka[33] based on a general solution of the Ziman formula for arbitrary degeneracy. Röpke and Redmer[34] provided a virial expansion for the electrical conductivity that is valid for classical fully ionized plasmas. The underlying linear response approach[35] was later generalized to the degenerate domain, and, in particular, the influence of electron–electron scattering was studied in detail.[36] Other conductivity models were derived by, for example, Stygar *et al.*[37] for nondegenerate Lorentz plasmas in magnetic fields and by Fortov *et al.*[38] for strongly correlated plasmas on the basis of experimental data for hydrogen and noble gases. Theoretical approaches to the description of charged particle transport in dense plasmas and for applications in astrophysics and inertial confinement fusion research have been compared recently, spanning methods from semi-empirical models to *ab initio* calculations.[39,40]

Another way to construct a user-friendly conductivity model is by solving the Boltzmann equation in relaxation-time approximation (RTA) for arbitrary degeneracy, as Lee and More (LM)[41] did in their well known study in 1984. By considering scattering cross sections in the Born approximation and applying simple cutoffs in the corresponding Coulomb logarithm, they provided expressions for the complete set of transport coefficients for plasmas in electric and magnetic fields for a given ionization state Z^*, which can be used for many practical applications. For weakly correlated high-temperature plasmas, the Spitzer limit with the prefactors of the Lorentz plasma[42,43] follows because electron–electron collisions are not accounted for in the RTA. The LM model was later generalized by Desjarlais[44] to include the effects of partial ionization and of electron–electron scattering. However, on using the LM model for WDM, one finds huge deviations from DFT-MD data,[23] which underlines the need to improve this and similar conductivity models for those conditions where strong collisions, electronic correlations, and the ionic structure factor have to be considered.

In this work, we describe an approach to improving the LM conductivity model for the case of a hydrogen plasma in the WDM regime. We use an extensive conductivity data set for the electrical and thermal conductivity based on DFT-MD simulations. Finally, we provide convenient interpolation formulas that can be used for applications in plasma and astrophysics as mentioned above.

II. THEORY AND METHODS

A. Density functional theory and molecular dynamics

We use an *ab initio* method based on the Born–Oppenheimer approximation. We describe our system by combining classic MD for the ions and DFT for finite temperatures[45–47] for the electrons. For the DFT-MD simulations, we use the Vienna *Ab initio* Simulation Package (VASP)[48–50] in version 5.4.4. Exchange and correlation (XC) effects of the electrons are approximated with the XC functional of Perdew, Burke, and Ernzerhof (PBE).[51] In our simulation, we use a projector augmented wave (PAW) potential[52–54] (labeled PAW H_h_GW) with a plane-wave cutoff of 1200 eV. For all simulations, we calculate the electronic wave function at the Baldereschi mean value point.[55] The temperature is controlled by a Nosé–Hoover thermostat.[56,57] Depending on the density and temperature of the system, we use up to 1400 atoms in our simulation box to get converged conductivity results and use a time step of 0.05–0.2 fs. The simulations run at least one ps up to several ps to provide a sufficient number of steps for the averages in equilibrium. The density and temperature vary from $\rho = 0.1$ to 8 g/cm^3 and from $T = 2000$ to 500 000 K.

To calculate the electronic transport properties, we run static DFT calculations for 10–200 ionic configurations from each equilibrated simulation and average the results over the number of configurations. Here, we use the Coulomb potential (instead of the PAW potential) with a cutoff of 2000 eV, which has also been done in previous work to get well-converged conductivity data.[23] We use several different Monkhorst–Pack **k**-point sets[58] to check the convergence behavior with the number of **k**-points.

The following expression for the frequency-dependent Onsager coefficients $L_n(\omega)$ can be derived from linear response theory:[21,22]

$$L_n(\omega) = \frac{2\pi(-1)^n}{V\omega} \sum_{\mathbf{k}\nu\mu} \mathrm{Re}\left(\langle \mathbf{k}\nu|\hat{\mathbf{v}}|\mathbf{k}\mu\rangle \otimes \langle \mathbf{k}\mu|\hat{\mathbf{v}}|\mathbf{k}\nu\rangle\right) \times (f_{\mathbf{k}\nu} - f_{\mathbf{k}\mu}) \left(\frac{E_{\mathbf{k}\mu} + E_{\mathbf{k}\nu}}{2} - h_e\right)^n \times \delta(E_{\mathbf{k}\mu} - E_{\mathbf{k}\nu} - \hbar\omega), \quad (1)$$

where ω is the frequency, V is the volume of the simulation box, $\langle \mathbf{k}\nu|\hat{\mathbf{v}}|\mathbf{k}\mu\rangle$ are the matrix elements of the velocity operator $\hat{\mathbf{v}}$, with $|\mathbf{k}\mu\rangle$ the Bloch states, $f_{\mathbf{k}\mu}$ are the Fermi occupation numbers, $E_{\mathbf{k}\mu}$ are the energy eigenvalues, h_e is the enthalpy per electron, and $\hbar$ is the reduced Planck constant. The matrix elements are calculated from the dipole matrix elements $\langle \mathbf{k}\nu|\hat{\mathbf{r}}|\mathbf{k}\mu\rangle$, which are taken directly from the optical routines of VASP.[22,59] To calculate transport properties from the Onsager coefficients, a Gaussian function is used to broaden the δ function to a small finite width. In our simulations, we select a broadening of 0.003–0.03 eV to get reasonable results.

The static electrical conductivity σ_e and thermal conductivity λ_e of the electrons are then given by

$$\sigma_e = e^2 \lim_{\omega\to 0} L_0(\omega), \quad (2)$$

$$\lambda_e = \frac{1}{T} \lim_{\omega\to 0} \left[L_2(\omega) - L_1(\omega) L_0^{-1}(\omega) L_1(\omega)\right], \quad (3)$$

where e is the elementary charge. The coefficient $L_0(\omega)$ is also known as the ω-dependent Kubo–Greenwood formula.[60,61] In practice, the static values are calculated by using a linear extrapolation to $\omega = 0$ across an unphysical decrease at very small ω. This is typically done in the energy region from 0.1 to 1 eV.

B. Electronic conductivity model

1. Lee–More expressions

Another way to calculate transport properties of partially ionized plasmas is to develop an appropriate multicomponent plasma model.[22] Solving the Boltzmann equation in the RTA, Lee and More[41] derived the following expression for the static Onsager coefficients:

$$K_n = -\frac{2m_e}{3\pi^2\hbar^3}\int_0^\infty dE\,\frac{E^{n+1}}{\sum_s n_s Q_{es}(E)}\frac{\partial f_e^0}{\partial E}, \tag{4}$$

which are directly connected to the electrical and thermal conductivities by

$$\sigma_e = e^2 K_0, \qquad \lambda_e = \frac{1}{T}\left(K_2 - \frac{K_1^2}{K_0}\right). \tag{5}$$

The Onsager coefficients K_n depend on the sum of transport cross sections $Q_{es}(E)$ and the derivative of the Fermi function. The transport cross sections describe how strongly electrons (e) are scattered by a specific scattering partner (s) for a given energy. For each scattering partner, one can write the specific Onsager coefficient in the form[22]

$$K_{n,es} = -\frac{2m_e}{3\pi^2\hbar^3 n_s}\int_0^\infty dE\,\frac{E^{n+1}}{Q_{es}(E)}\frac{\partial f_e^0}{\partial E} \tag{6}$$

or, by using the relaxation time τ,[23]

$$K_{n,es} = -\frac{2^{3/2}m_e^{1/2}}{3\pi^2\hbar^3}\int_0^\infty dE\,E^{n+3/2}\tau_{es}(E)\frac{\partial f_e^0}{\partial E}, \tag{7}$$

where the specific relaxation time $\tau_{es} = 1/(\nu Q_{es} n_s)$ for the scattering partner s. In the following, we use Eq. (7) for electron–ion scattering and Eq. (6) for electron–neutral scattering to calculate the specific electrical conductivity σ_{es} and thermal conductivity λ_{es}. The total conductivity values are then calculated according to the Matthiessen rule

$$\sigma_e^{-1} = \sum_s \sigma_{es}^{-1}, \qquad \lambda_e^{-1} = \sum_s \lambda_{es}^{-1}. \tag{8}$$

This Matthiessen-rule-like ansatz for the thermal conductivity is motivated by theories from liquid mixtures[62] and a previous approach to add electron–electron scattering to DFT results.[63]

2. Electron–ion scattering

In most conductivity models, electron–ion scattering is treated with a screened Coulomb potential using, for example, the Debye–Hückel screening length to derive an expression for the relaxation time in the Born approximation.[22,23,64] This leads to a dependence on the so-called Coulomb logarithm, which is approximated via certain points that describe, for example, the effective minimal and maximal scattering distance from the ions.[65]

Here, we adopt a simple expression for the relaxation time,

$$\tau_{eI}(E) = \frac{E^{3/2}P(T,\rho_I)}{n_I Z_I^2}, \tag{9}$$

which has the same dependence on energy, particle density and charge as the relaxation time in the Born approximation. The fitting parameter $P(T,\rho_I)$ is used to provide an accurate match of the LM model, which describes weakly coupled systems at high temperatures, to our DFT results for stronger coupled systems at lower temperatures so that both cases are included. This parameter depends only on the temperature T and the ion density ρ_I and not on the energy, and so we can take it out of the integral in Eq. (7) and get a simple expression for this Onsager coefficient:

$$K_{n,eI} = -\frac{2^{3/2}m_e^{1/2}P(T,\rho_I)}{3\pi^2\hbar^3 n_I Z_I^2}\int_0^\infty dE\,E^{n+3}\frac{\partial f_e^0}{\partial E}. \tag{10}$$

3. Electron–neutral scattering

For the scattering of electrons by atoms and nonpolar molecules, we adopt the expression for the Onsager coefficients given by French and Redmer:[22]

$$K_{n,eN} = \frac{2^{11/2}\pi^{1/2}(n+3)!\varepsilon_0^2(k_BT)^{n+3/2}n_e}{3e^4m_e^{1/2}n_N\sum_i Z_{N,i}^2\ln A_{N,i}(x_{n,N,i})}, \tag{11}$$

with the atomic logarithm function

$$\ln A_N(E) = \left[\frac{\ln(x_N+1)}{2} - \frac{3a_N^2+6a_Nb_N-2b_N^2}{6a_N^2} + \frac{4a_Nb_N+a_N^2}{2a_N^2(x_N+1)} - \frac{b_N^2+a_Nb_N}{a_N^2(x_N+1)^2} + \frac{2b_N^2}{3a_N^2(x_N+1)^3}\right]. \tag{12}$$

The parameters Z_N, a_N, and b_N are used to fit the transport cross section of electrons on neutral species N; they are also taken from Ref. 22. The logarithm function is evaluated at

$$x_{n,N,i} = 8\sqrt{(n+2)(n+3)}b_{N,i}^2 m_e k_B T/\hbar^2. \tag{13}$$

With this expression, one can calculate all possible processes of scattering of electrons by neutral atoms and nonpolar molecules. Here, we assume scattering by hydrogen atoms only. The influence of scattering by hydrogen molecules becomes important for low-temperature plasmas, which are not studied here. In the temperature and density region considered in this work, hydrogen atoms are either ionized or single atoms, which are mostly free or bonded for very short times with a second hydrogen atom (transient molecules). This feature permits us to neglect dissociation processes. Thus, the number of neutral scattering partners is defined by the ionization degree α.

C. Ionization degree

We assume a system of hydrogen atoms H, protons H^+, and electrons e, and so the ionization degree is defined as

$$\alpha = \frac{N_e^{\text{free}}}{N_e^{\text{total}}} = \frac{N_{H^+}}{N_{H^+} + N_H}, \tag{14}$$

where $N_{H^+} + N_H = N_{H,\text{total}}$ is the total number of protons or hydrogen atoms. The density of the system is also directly connected to the total number of hydrogen atoms:

$$\rho = \rho_H + \rho_{H^+} + \rho_e \approx \rho_H + \rho_{H^+} = \rho_{H,\text{total}}. \tag{15}$$

We use these two quantities to define the densities of ions and of neutral atoms, which are needed in Eqs. (10) and (11):

$$\rho_I = \rho_{H^+} = \alpha\rho_{H,\text{total}}, \tag{16}$$

$$\rho_H = (1-\alpha)\rho_{H,\text{total}}. \tag{17}$$

The number density is then given by $n_i = \rho_i/m_H$, with $i = \{H, H^+\}$ and m_H the mass of the hydrogen atom. For hydrogen, the number density of free electrons n_e is equal to the number density of ions (protons). In this work, α is calculated by matching our conductivity model to the DFT data and not by applying a chemical model such as the Saha equation to determine the plasma composition separately (see Sec. III B).

III. RESULTS

A. Fully ionized hydrogen plasma

First we investigate the simplest case of a fully ionized hydrogen plasma, where all atoms are ionized and only electron–ion scattering occurs. We use the electrical conductivity results from the DFT simulations using the Kubo–Greenwood formula and the results from the LM model with a screened Coulomb logarithm that includes degeneracy[23] for high temperatures to fit Eq. (10). For that purpose, we employ the following expression for the fitting parameter $P(T,\rho_I)$:

$$P(T,\rho_I) = a_0 T^{a_1}\rho^{a_2} + a_3\rho^{a_4} + a_5 + a_6\rho^{a_7}\exp\left[-\left(\frac{\log T - a_8}{a_9}\right)^2\right], \tag{18}$$

where we insert the values for T in kelvin and ρ in g/cm^3. The coefficients $a_0, \ldots, a_9$ are given in Table I. The first three terms of the fitting parameter $P(T,\rho_I)$ describe the high-temperature behavior of the LM model, while the last term describes the differences between the high-temperature LM model and the DFT results for lower temperatures where stronger interactions have to be taken into account. The resulting electrical and thermal conductivities are shown in Figs. 1 and 2.

For temperatures above 10^6 K, we consider a weakly coupled plasma and use the results from the LM model. If we ignore electron–electron scattering, the electrical conductivity exhibits Lorentz plasma behavior for a weakly coupled plasma at high temperature. For temperatures below 10^6 K, we use the DFT conductivity to capture stronger correlations in our fit. The curves in

TABLE I. Values of the coefficients a_j in $P(T,\rho_I)$ given by Eq. (18).

a_0	27.95×10^{39} s/(J$^{3/2}$·m^3)
a_1	−0.229 9
a_2	0.104 9
a_3	$0.007\,793 \times 10^{39}$ s/(J$^{3/2}$·m^3)
a_4	0.427 9
a_5	$0.214\,9 \times 10^{39}$ s/(J$^{3/2}$·m^3)
a_6	8.527×10^{39} s/(J$^{3/2}$·m^3)
a_7	0.541 4
a_8	1.523
a_9	2.455

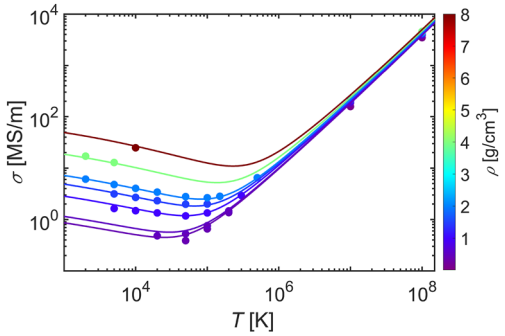

FIG. 1. Electrical conductivity for a fully ionized hydrogen plasma as a function of temperature and density (color-coded). The results from DFT simulations (<10^6 K) and the original LM model[41] (>10^6 K) are shown by the circles and those from Eq. (10) using the fitting parameter $P(T,\rho_I)$ are shown by the curves.

Fig. 1 representing the results using the fitting parameter $P(T,\rho_I)$ nearly overlap the circles representing the DFT and RTA results. This indicates that it is possible to modify the LM model for a fully ionized one-component plasma by using an improved relaxation time that includes the effects of strong correlations, which are

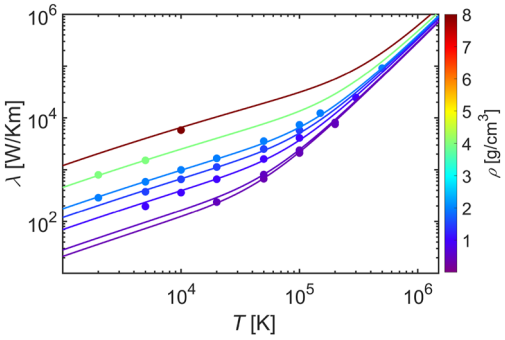

FIG. 2. Thermal conductivity for a fully ionized hydrogen plasma as a function of temperature and density (color-coded). The results from DFT simulations are shown by the circles and those from Eq. (10) using the fitting parameter $P(T,\rho_I)$ are shown by the curves.

essential in WDM. Nevertheless, it is questionable whether the fitting parameter (18) also holds for the very high densities typical of stellar cores or the interiors of compact objects such as white dwarfs. The limits of our model are discussed in Secs. III B and III C. In general, the model describes metallic behavior for lower temperatures, where the stronger vibrations of the ions with temperature lower the conductivity until the system runs into the Spitzer or, here, the Lorentz limit, where the conductivity increases with temperature again.

We can also obtain correct results for the thermal conductivity. In Fig. 2, we show only the region where we compare our fitting parameter with the DFT data. The agreement is again very good. Note that our model slightly overestimates the results for both conductivities for lower densities, but all deviations are within 10%, which is a typical estimate for the uncertainty of DFT conductivities in the WDM domain.

B. Partially ionized hydrogen plasma

Ionization or dissociation effects have not been included in our model so far, although these are essential for lower temperatures and lower densities. The EOS and the composition of partially ionized hydrogen plasmas have long been treated by chemical models. For instance, Ebeling and Richert constructed efficient Padé formulas valid for the thermodynamic functions of fully ionized hydrogen,[66] which were used to predict the plasma composition via chemical models (see, e.g., Ref. 67). Fluid variational theory (FVT) was applied successfully to infer EOS data for shock-compressed liquids[68] and, in particular, for the description of the dissociation equilibrium in dense hydrogen.[69,70] The free-energy model of Saumon, Chabrier, and van Horn[71] treats the dissociation and ionization equilibrium in hydrogen self-consistently and has found widespread applications in plasma physics and astrophysics. Däppen *et al.*[72–75] derived an EOS for hydrogen plasmas to model stellar envelopes. Chemical models have also been applied to evaluate explosively driven shock-wave experiments.[76] The corresponding transport coefficients of partially ionized hydrogen plasmas have been calculated with the aim of locating the nonmetal-to-metal transition in density–temperature space (see, e.g., Refs. 77–79).

An important application of models of partially ionized hydrogen plasmas is to the outer layer of gas giant planets, which are cold and thin enough to consist of molecular hydrogen plus helium and a small amount of heavier elements. Increasing pressure and temperature toward the center of the planet drives dissociation and ionization—hydrogen transforms to a metal. This nonmetal-to-metal transition is of first order below a critical temperature of about 1500 K and a pressure of a few Mbar: a liquid–liquid phase transition (LL-PT). Above the critical temperature, the transition is abrupt but continuous. The location of the corresponding coexistence line has been discussed for many years; for a recent review, see Ref. 26. Calculations based on DFT locate the continuous nonmetal-to-metal transition at about 90% of Jupiter's radius[2] and 70% of Saturn's radius,[3] respectively. The conductivities and other material data are important to better understand the dynamo action in the deep interior of gas giants via MHD simulations (see, e.g., Refs. 16 and 17). Another example is Ohmic dissipation, which might occur in the atmospheres of hot Jupiters. This process is a candidate to explain the radius anomaly of many hot Jupiters.[18,19,80]

TABLE II. Coefficients b_i for the ionization degree α in Eq. (19).

b_0	0.043 91
b_1	0.828 50
b_2	1.918×10^9
b_3	−2.471 0
b_4	2.697 0

Therefore, we generalize the conductivity model derived in Sec. II B to a partially ionized hydrogen plasma. As already mentioned in Sec. II, we assume that the hydrogen plasma consists of atoms, protons, and electrons. This means that we treat all neutrals as atoms. Hydrogen molecules are consequently described by two individual hydrogen atoms. The ionization degree α is calculated from the formula

$$\alpha = 1 - \frac{1}{b_0 T^{b_1} \rho^{(b_2 T^{b_3} + b_4)} + 1} \tag{19}$$

by fitting its value to the electrical conductivity from DFT calculations using the model for a fully ionized hydrogen plasma. Equation (11) for the contribution of electron–neutral interactions is then used to determine the total conductivity via Eq. (8). The parameters b_i in Eq. (19) are given in Table II. We insert again the values for T in kelvin and for ρ in g/cm^3.

In both terms, the ionization degree α defines the number of electrons and the number of scattering partners. The calculated ionization degree that reproduces the DFT results within our model is shown in Fig. 3. The curves show the ionization degree α fitted using Eq. (19). Note that we have used some additional conductivity data for 1 g/cm^3 at 1000 and 2000 K from Holst *et al.*[21] to achieve an improved behavior for the ionization degree in that domain.

Applying the widely used but approximate Saha equations leads to too low ionization degrees for such dense plasmas, as can be seen from the dashed curves in Fig. 3. A rigorous method to determine the ionization degree α is based on the Thomas–Reiche–Kuhn sum rule for the dynamic electrical conductivity, which is calculated via the Kubo–Greenwood equation using DFT. This method provides

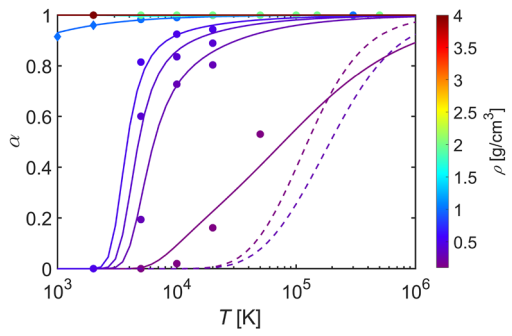

FIG. 3. Ionization degree α as a function of temperature and density (color-coded). The optimal values for the DFT results are shown by the circles (this work) and diamonds (from Holst *et al.*[21]), while the best fits for all conditions are shown by the solid curves. For comparison, the resulting α values from the Saha equation are shown by the dashed curves.

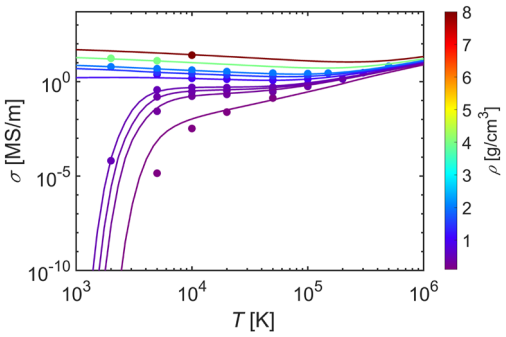

FIG. 4. Electrical conductivity as a function of temperature and density (color-coded) for a partially ionized hydrogen plasma. The direct results from the DFT simulations are shown by the circles and the results from the conductivity model are shown by the curves.

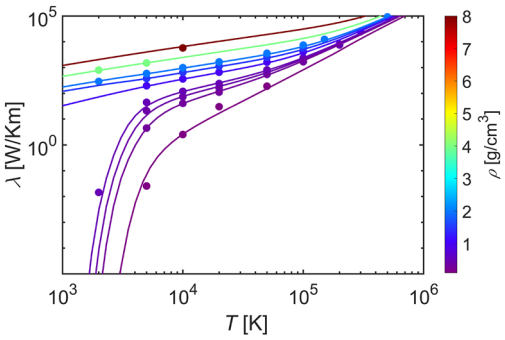

FIG. 5. Thermal conductivity as a function of temperature and density (color-coded) for a partially ionized hydrogen plasma. The direct results from the DFT simulations are shown by the circles, and the results from the conductivity model are shown by the curves.

reliable ionization degrees for high-density carbon[81] and beryllium plasma[82] and was also tested here. However, the sum-rule method does not hold for conditions where the bandgap starts to close or vanishes. For hydrogen, we found an unphysical decrease of the ionization degree with temperature for high densities just in that region. This problem can probably be resolved by using improved meta-generalized gradient approximation (meta-GGA) XC functionals like SCAN (Strongly Constrained and Appropriately Normed)[83] or hybrid functionals like HSE (Heyd–Scuseria–Ernzerhof),[84] which yield more realistic bandgaps compared with the PBE GGA XC functional used in this study.

Therefore, the strong deviations from the target values for the ionization degree in that specific region motivated us to use the fitting formula (19). This provides reliable results for the ionization degree for most densities. Note that the fit starts to deviate strongly in the low-density region where the Saha equation approach holds and only temperature-driven ionization is relevant. Therefore, we use the results of the Saha equation approach whenever they are higher than the ionization degree predicted by the fitting formula (19).

Using the values for the ionization degree determined from Eq. (19), we calculate the electrical and thermal conductivities, as shown by the curves in Figs. 4 and 5, where the circles show the results of the DFT simulations. We very accurately resolve the region where the hydrogen plasma is metallic and the ionization degree is high within our model. We also capture the transition to the non-metallic region in the low-temperature limit. One can see that the deviations become more pronounced at low temperatures and low densities. Note that the densities are still too high for the Saha equation approach, which results in some order-of-magnitude differences. Nevertheless, the plasma has a very low conductivity in both cases, i.e., the number of free electrons and also the corresponding ionization degree α are very low.

Note that the ionic contribution to the currents has to be taken into account for low temperatures and low densities as are typical of, for example, the outer layer of a gas giant planet. Hydrogen is mostly atomic or molecular in this layer, and the thermal conductivity is dominated by the ionic part λ_i and not by the electronic contribution λ_e (see Refs. 2 and 3).

C. Comparison with experiments and computations

In this subsection, we benchmark our conductivity model with other computational methods and available experimental data for dense hydrogen over a wide range of temperatures and densities.

First, we compare our results for the electrical conductivity with those obtained by Lambert *et al.*[85] They used an orbital-free treatment for the electrons in MD simulations to generate atomic configurations for high densities and temperatures. Then, they calculated the transport coefficients within the Kubo–Greenwood formalism [see Sec. II A and Eqs. (1)–(3)] for five snapshots by using DFT in the local density approximation (LDA). To include electron-electron interaction, they used a correction factor given by Bespalov and Polishchuk[86] as described in Ref. 87. The comparison is presented in Fig. 6.

We find very good agreement with the data of Lambert *et al.*[85] for a density of 10 g/cm^3 and the LM model for high temperatures. For higher densities and lower temperatures, we get considerably higher conductivity values. This deviation decreases with temperature, where the Spitzer limit is fulfilled for both methods. Note that we have included the same electron–electron correction factor as chosen by Lambert *et al.* in our model and the LM model, and

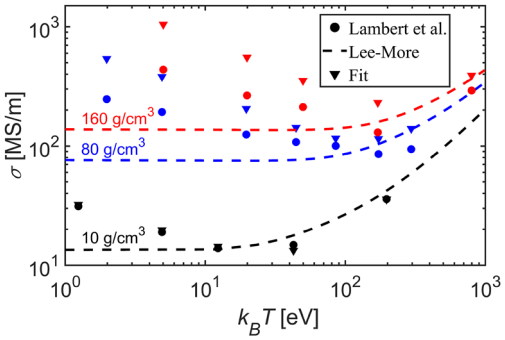

FIG. 6. Electrical conductivity as a function of temperature for three different densities from our model (triangles) in comparison with the results of Lambert *et al.*[85] (circles) and the Lee–More model[23,41] (dashed curves).

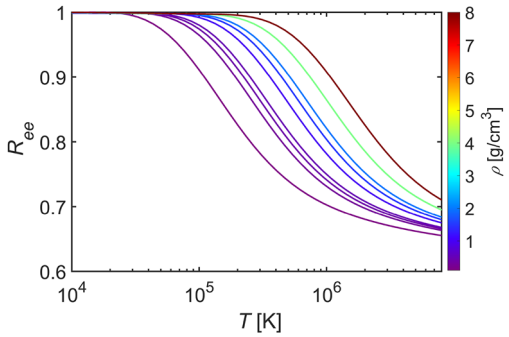

FIG. 7. Electron–electron correction factor R_{ee} for different densities (color-coded) from Eq. (34) in Ref. 36.

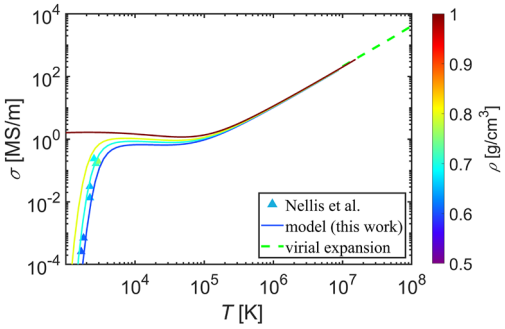

FIG. 8. Comparison of the electrical conductivity from our model (color-coded solid curves) with the gas-gun experiment of Weir *et al.*[90] and Nellis *et al.*[91] (triangles) and the virial expansion of Röpke *et al.*[64,92] for 1 g/cm^3 (green dashed curve).

so this is not the source of the deviations obtained. The deviations for very high densities, especially in the low-temperature region, may be traced back to a different treatment of the broadening or smearing parameter when calculating the Onsager coefficients. If the broadening parameter is chosen too high, the dynamic conductivity has a nonzero Drude-like behavior for $\omega \to 0$ (see Fig. 6 in Ref. 85), while a linear extrapolation should be performed toward the static limit in the region of the unphysical decrease (this paper). This would explain why the results of Lambert *et al.* are systematically lower than those obtained using a linear extrapolation method. Nevertheless, a deviation by a factor of 2 for lower temperatures can probably be traced back not only to the different extrapolation methods. Therefore, we have performed additional simulations for higher densities (20, 50, and 70 g/cm^3) at T = 200 000 K and for 70 g/cm^3 at T = 1 000 000 K. We find that our model overestimates the DFT conductivity values for higher densities. The differences amount to 50% at ρ = 70 g/cm^3. The deviation decreases at higher temperatures. This trend indicates a stronger deviation for even higher densities at lower temperatures, where our model has to be used with caution. For high temperatures, we find better agreement with the LM model that describes the right Spitzer limit by including electron–electron collisions for all three densities. Thus, our model can be used for high densities in the high-temperature limit.

A rigorous formalism to include electron–electron collisions far beyond the simple model of Bespalov and Polishchuk[86] was developed by Reinholz *et al.*[36] within generalized linear response theory. The resulting correction factor R_{ee} that accounts for electron–electron scattering is shown in Fig. 7 for our density–temperature grid. We find that the electron–electron correction factor becomes important for very high temperatures at the densities considered here.

Electron–electron collisions are also important for the conductive opacity κ_c of astrophysical objects, which is directly connected to the thermal conductivity via

$$\kappa_c = \frac{16\sigma_B T^3}{3\rho\lambda}, \tag{20}$$

where σ_B is the Stefan–Boltzmann constant. For many applications in astrophysics, the conductive opacity is calculated with an effective collision frequency that depends on the Coulomb logarithm. Cassisi *et al.*[88] and Blouin *et al.*[89] provide fitting formulas for the opacity of fully ionized hydrogen plasmas over a wide range of densities and temperatures, including electron–electron scattering effects. Our model does not include electron–electron scattering for the thermal conductivity. Cassisi *et al.*[88] provide opacity results for both cases, i.e., electron–ion and electron–ion + electron–electron scattering, while Blouin *et al.*[89] give a correction factor for the Cassisi model at $T > 0.1T_F$, where T_F is the Fermi temperature. Combining the results from Figs. 6 and 7, a comparison is only applicable for temperatures $T < 10^5$ K for lower densities and for very high densities around 100 g/cm^3 where the electron–electron corrections are very small also for high temperatures. Much higher densities as are relevant in white dwarfs cannot be investigated within the current model, because in such a dense plasma relativistic effects have to be taken into account. Our results in the region where we trust our model provide good agreement with the results of Cassisi *et al.*[88] for electron–ion scattering and also agree with the results of Blouin *et al.*,[89] where we expect no or weaker electron–electron correction effects. Note that the decomposition for λ according to electron–ion and electron–electron scattering processes as introduced in Ref. 63 and used by Blouin *et al.*[89] is not valid, as shown by French *et al.*[23]

On the contrary, corrections due to electron–electron scattering can be neglected for low temperatures of only few thousand

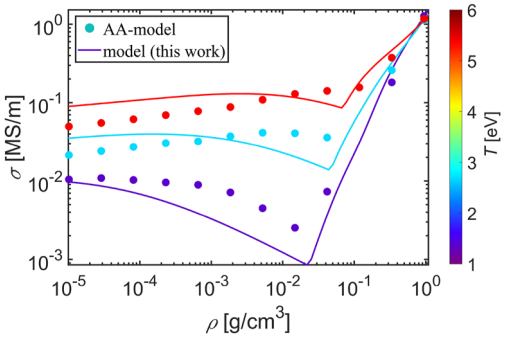

FIG. 9. Comparison of the electrical conductivity from our model (color-coded curves) with results from an AA model (circles).[26] Note that the points below 0.01 g/cm^3 are not shown in Fig. 42 of Ref. 26, but are included here with the permission of the authors.

kelvin, owing to Pauli blocking (degenerate region). In Fig. 8, we compare the predictions of our conductivity model with (i) the gas-gun experiments of Weir *et al.*[90] and Nellis *et al.*[91] inspecting the low-temperature region of a few thousand kelvin and (ii) the virial expansion of Röpke *et al.*,[64,92] which represents the correct high-temperature limit. We find very good agreement with the high-temperature limit given by the virial expansion and also match the experimental results in the lower-temperature region quite well. We can also reproduce the density between 0.6 and 0.7 g/cm^3 as determined in the experiment.

We conclude that our conductivity model predicts the behavior of dense hydrogen over a wide range of temperatures. Other

TABLE III. Electrical and thermal conductivity data calculated with DFT and the values according to our conductivity model using the fitting formulas (9) and (18). Also shown is the ionization degree α calculated by the fitting formula (19).

ρ (g/cm^3)	T (K)	σ_{DFT} (MS/m)	σ_{fit} (MS/m)	λ_{DFT} [W/(K·m)]	λ_{fit} [W/(K·m)]	α_{fit}
0.1	5000	1.41×10^{-5}	$7.265\,2 \times 10^{-4}$	0.025 54	0.074 4	0.004 2
0.1	10 000	0.003 3	0.010 5	2.516	2.601 0	0.092 6
0.1	20 000	0.024 44	0.031 5	30.11	16.702 2	0.225 4
0.1	50 000	0.125 6	0.108 3	188.5	151.669 8	0.405 6
0.3	5000	0.027 07	0.040 7	4.476	4.400 4	0.271 2
0.3	10 000	0.170 1	0.168 0	40.69	39.943 4	0.722 4
0.3	20 000	0.21	0.236 4	110.9	119.610 4	0.855 4
0.3	50 000	0.291 6	0.365 7	540.3	501.82	0.929 9
0.3	100 000	0.554 3	0.640 3	1692	1836.6	0.959 5
0.4	5000	0.155 9	0.131 5	20.76	14.144 8	0.546 6
0.4	10 000	0.294 2	0.315 6	73.07	75.259 2	0.858 7
0.4	20 000	0.332 2	0.369 9	164.6	185.233 6	0.928 7
0.4	50 000	0.388 1	0.475 1	669.6	641.143 5	0.966 5
0.4	100 000	0.658 7	0.748 4	2103	2127.3	0.980 9
0.4	200 000	1.367	1.455 9	7515	8501.2	0.989 2
0.5	2000	2.19×10^{-5}	$8.155\,3 \times 10^{-5}$	0.022 35	0.002 9	$3.482\,2 \times 10^{-4}$
0.5	5000	0.363 7	0.289 9	44.76	31.602 0	0.750 0
0.5	10 000	0.490 4	0.483 4	118.6	115.794 2	0.921 4
0.5	20 000	0.483 6	0.510 2	238.3	253.993 8	0.960 0
0.5	50 000	0.514 68	0.584 1	809.4	777.451 0	0.981 4
0.5	100 000	0.760 7	0.849 8	2372	2394	0.989 5
0.5	200 000	1.399	1.573 7	8159	9154.7	0.994 0
1.0	5000	1.636	1.596 8	196.2	187.728 6	0.980 8
1.0	10 000	1.481	1.463 8	361.7	354.862 2	0.989 1
1.0	20 000	1.345	1.297 0	657.4	638.669 0	0.993 8
1.0	50 000	1.178	1.174 0	1612	1502.5	0.997 1
1.0	100 000	1.347	1.357 1	4108	3687.6	0.998 4
1.0	300 000	2.926	3.022 9	2.45×10^4	2.6337×10^4	0.999 3
1.5	5000	3.153	3.101 3	375.8	373.476	0.996 3
1.5	10 000	2.689	2.607 6	652.8	634.464 9	0.996 7
1.5	20 000	2.318	2.212 2	1129	1085.9	0.998 0
1.5	50 000	1.981	1.850 8	2507	2329	0.999 0
1.5	100 000	2.004	1.909 1	5781	5061.3	0.999 5
2.0	2000	6.087	6.138 7	288.8	299.943 6	1
2.0	5000	4.801	4.719 6	587.9	572.687 0	0.998 8
2.0	10 000	4.028	3.888 3	991.7	947.533 8	0.998 6
2.0	20 000	3.412	3.237 3	1656	1586.8	0.999 1
2.0	50 000	2.791	2.604 7	3560	3248.9	0.999 6
2.0	100 000	2.659	2.509 9	7348	6541.7	0.999 7
2.0	150 000	2.825	2.751 3	1.23×10^4	1.1156×10^4	0.999 8
2.0	500 000	6.499	6.402 2	9.16×10^4	9.3106×10^4	0.999 9
4.0	2000	17.09	15.867 8	795.1	775.166 3	1
4.0	5000	12.821	12.435 5	1515	1517.5	0.999 9
8.0	10 000	24.864	26.606 3	5798	6498.3	1

experiments by, for example, Ternovoi *et al.*[93] and Fortov *et al.*[38,76] show the same jump in conductivity with density, but at slightly higher temperatures. This deviation can be traced back to the determination of the temperature in these experiments.

We also compare our model with results from an average atom (AA) model[94] in the low-density regime, which are shown in Fig. 42 of Ref. 26. The DFT results and the AA data match nearly perfectly for densities above 0.1 g/cm^3, which was also shown in previous work.[39] For lower densities, it is very difficult and numerically expensive to converge the DFT-MD simulations. Here, we can use our model to extrapolate to very low densities. In Fig. 9, we show the low-density behavior of our model compared with the AA model for temperatures of 1.35, 2.69, and 5.39 eV. We find the same general trends as predicted by the AA model, but the deviations are greater than for higher densities. For all three temperatures, one can see a kink in the data set of our model. At this point, we change the value for α from our fit via Eq. (19) to the value given by the Saha equation. This leads to higher ionization with decreasing density. The same behavior is observed in the AA model at nearly the same densities. Combining the results from Figs. 8 and 9, we can predict the general behavior of the ionization degree and the conductivity in the low- and high-density regions.

IV. CONCLUSION

We have calculated an extensive DFT-MD data set for the electrical and thermal conductivity of hydrogen in a wide range of density ρ and temperature T. Based on these *ab initio* results, we have proposed a modified LM model that provides improved predictions for the electrical and thermal conductivities for a dense hydrogen plasma in the fully and partially ionized region by just changing the relaxation time. In addition, we have introduced an expression for the ionization degree α to generalize our model from the fully to the partially ionized plasma region.

Our new conductivity model shows in general very good agreement with other computational results and available experimental data over a wide range of densities and temperatures. The underlying *ab initio* data and the proposed fitting formula can be further benchmarked by future experiments to provide a better understanding of the behavior of warm dense hydrogen. This is essential for improved predictions for the interior structure, thermal evolution, and dynamo action in, for example, gas giant planets. Our model can also be used for conditions in stellar interiors exceeding densities of $\rho = 100$ g/cm^3 and for temperatures up to $T = 1000$ eV.

ACKNOWLEDGMENTS

We thank Martin French for motivating this study and for continual interest in this project. Furthermore, we thank Armin Bergermann, Martin Preising, Argha Roy, and Gerd Röpke for many helpful discussions. We thank Jan Vorberger and Stephanie B. Hansen for providing the AA results for the electrical conductivity shown in Fig. 9. This work was supported by the Priority Program SPP 1992 of the German Science Foundation (DFG) *The Diversity of Exoplanets* under project number 362460292. The *ab initio* calculations were performed at the North-German Supercomputing Alliance (HLRN) facilities and at the IT and Media Center of the University of Rostock.

AUTHOR DECLARATIONS

Conflict of Interest

The authors have no conflicts to disclose.

Author Contributions

Uwe Kleinschmidt: Conceptualization (equal); Formal analysis (lead); Investigation (equal); Visualization (lead); Writing – original draft (equal). **Ronald Redmer**: Conceptualization (equal); Investigation (equal); Supervision (lead); Writing – original draft (equal).

DATA AVAILABILITY

The data that support the findings of this study are available within the article or from the corresponding author upon reasonable request.

APPENDIX A: DATA TABLE

In Table III, we present the electrical and thermal conductivity data calculated with DFT and the values according to our conductivity model using the fitting formulas (9) and (18). The agreement is best in the degenerate high-density limit and becomes less accurate in the partially ionized region at lower temperatures.

APPENDIX B: ACCURACY FOR FULLY IONIZED PLASMAS

We present the results from our model to fit the DFT and LM data for a fully ionized hydrogen plasma in Figs. 1 and 2 and find good agreement over the whole data set. Nevertheless, some small deviations at lower densities are visible. A better understanding of how good a fit actually works can be obtained by looking at the residual plots. These plots for the electrical and thermal conductivities are given in Figs. 10 and 11.

Most of the points are fluctuating around 1 in an area of ±12.5% from the DFT and LM results. There are some significant deviations for the lowest densities at lower temperatures (e.g., at 0.4 g/cm^3 and $T < 200\,000$ K). The reason for the deviations from the DFT data

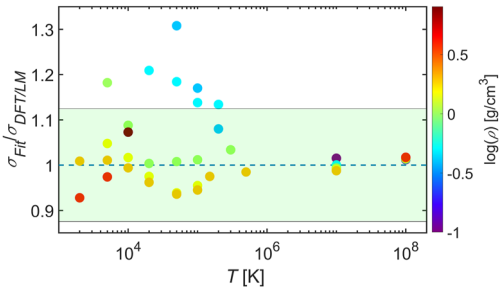

FIG. 10. Residual plot for the electrical conductivity vs temperature for different densities (color-coded). The green area represent a deviation of ±12.5% from the DFT results for $T < 10^6$ K and the LM results for $T > 10^6$ K, which is in the range of typical error estimates for transport coefficients.

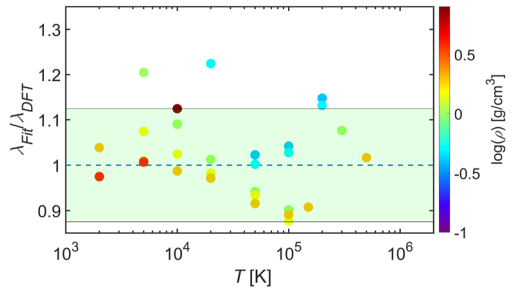

FIG. 11. Residual plot for the thermal conductivity vs temperature for different densities (color-coded). The green area represents a deviation of ±12.5% from the DFT results, which is in the range of typical error estimates for transport coefficients.

is that the system is strongly but not fully ionized under these conditions, as shown in Fig. 3. On including this ionization effect, the points are shifted downward into the green area, as one can see in Table III.

REFERENCES

[1] T. Guillot, L. N. Fletcher, R. Helled, M. Ikoma, M. R. Line *et al.*, "Giant planets from the inside-out," in *Protostars and Planets VII*, edited by S. Inutsuka, Y. Aikawa, T. Muto, K. Tomida, and M. Tamura (Astronomical Society of the Pacific Conference Series, San Francisco, 2023), pp. 947–991.

[2] M. French, A. Becker, W. Lorenzen, N. Nettelmann, M. Bethkenhagen *et al.*, "Ab initio simulations for material properties along the Jupiter adiabat," Astrophys. J., Suppl. Ser. **202**, 5 (2012).

[3] M. Preising, M. French, C. Mankovich, F. Soubiran, and R. Redmer, "Material properties of Saturn's interior from ab initio simulations," Astrophys. J., Suppl. Ser. **269**, 47 (2023).

[4] A. Becker, M. Bethkenhagen, C. Kellermann, J. Wicht, and R. Redmer, "Material properties for the interiors of massive giant planets and brown dwarfs," Astron. J. **156**, 149 (2018).

[5] S. X. Hu, B. Militzer, V. N. Goncharov, and S. Skupsky, "First-principles equation-of-state table of deuterium for inertial confinement fusion applications," Phys. Rev. B **84**, 224109 (2011).

[6] B. Militzer, F. González-Cataldo, S. Zhang, K. P. Driver, and F. Soubiran, "First-principles equation of state database for warm dense matter computation," Phys. Rev. E **103**, 013203 (2021).

[7] D. Durante, M. Parisi, D. Serra, M. Zannoni, V. Notaro *et al.*, "Jupiter's gravity field halfway through the Juno mission," Geophys. Res. Lett. **47**, e2019GL086572, https://doi.org/10.1029/2019gl086572 (2020).

[8] A. P. Ingersoll, "Cassini exploration of the planet Saturn: A comprehensive review," Space Sci. Rev. **216**, 122 (2020).

[9] J. E. P. Connerney, A. Adriani, F. Allegrini, F. Bagenal, S. J. Bolton *et al.*, "Jupiter's magnetosphere and aurorae observed by the Juno spacecraft during its first polar orbits," Science **356**, 826–832 (2017).

[10] Y. Kaspi, E. Galanti, A. P. Showman, D. J. Stevenson, T. Guillot *et al.*, "Comparison of the deep atmospheric dynamics of Jupiter and Saturn in light of the Juno and Cassini gravity measurements," Space Sci. Rev. **216**, 84 (2020).

[11] F. Bagenal, A. Adriani, F. Allegrini, S. J. Bolton, B. Bonfond *et al.*, "Magnetospheric science objectives of the Juno mission," Space Sci. Rev. **213**, 219–287 (2017).

[12] S. J. Bolton, A. Adriani, V. Adumitroaie, M. Allison, J. Anderson *et al.*, "Jupiter's interior and deep atmosphere: The initial pole-to-pole passes with the Juno spacecraft," Science **356**, 821–825 (2017).

[13] S. M. Wahl, W. B. Hubbard, B. Militzer, T. Guillot, Y. Miguel *et al.*, "Comparing Jupiter interior structure models to Juno gravity measurements and the role of a dilute core," Geophys. Res. Lett. **44**, 4649–4659, https://doi.org/10.1002/2017gl073160 (2017).

[14] U. R. Christensen and J. Wicht, "Models of magnetic field generation in partly stable planetary cores: Applications to Mercury and Saturn," Icarus **196**, 16 (2008).

[15] G. Schubert and K. M. Soderlund, "Planetary magnetic fields: Observations and models," Phys. Earth Planet. Inter. **187**, 92 (2011).

[16] C. A. Jones, "A dynamo model of Jupiter's magnetic field," Icarus **241**, 148–159 (2014).

[17] J. Wicht and U. R. Christensen, "Contributions of Jupiter's deep-reaching surface winds to magnetic field structure and secular variation," J. Geophys. Res.: Planets **129**, e2023JE007890, https://doi.org/10.1029/2023je007890 (2024).

[18] S. Kumar, A. J. Poser, M. Schöttler, U. Kleinschmidt, W. Dietrich *et al.*, "Ionization and transport in partially ionized multicomponent plasmas: Application to atmospheres of hot Jupiters," Phys. Rev. E **103**, 063203 (2021).

[19] W. Dietrich, S. Kumar, A. J. Poser, M. French, N. Nettelmann *et al.*, "Magnetic induction processes in hot Jupiters, application to KELT-9b," Mon. Not. R. Astron. Soc. **517**, 3113 (2022).

[20] P. Wulff, U. R. Christensen, W. Dietrich, and J. Wicht, "The effects of a stably stratified region with radially varying electrical conductivity on the formation of zonal winds on gas planets," J. Geophys. Res.: Planets **129**, e2023JE008042, https://doi.org/10.1029/2023je008042 (2024).

[21] B. Holst, M. French, and R. Redmer, "Electronic transport coefficients from *ab initio* simulations and application to dense liquid hydrogen," Phys. Rev. B **83**, 235120 (2011).

[22] M. French and R. Redmer, "Electronic transport in partially ionized water plasmas," Phys. Plasmas **24**, 092306 (2017).

[23] M. French, G. Röpke, M. Schörner, M. Bethkenhagen, M. P. Desjarlais *et al.*, "Electronic transport coefficients from density functional theory across the plasma plane," Phys. Rev. E **105**, 065204 (2022).

[24] C. E. Starrett, N. R. Shaffer, D. Saumon, R. Perriot, T. Nelson *et al.*, "Model for the electrical conductivity in dense plasma mixtures," High Energy Density Phys. **36**, 100752 (2020).

[25] J. M. McMahon, M. A. Morales, C. Pierleoni, and D. M. Ceperley, "The properties of hydrogen and helium under extreme conditions," Rev. Mod. Phys. **84**, 1607–1653 (2012).

[26] M. Bonitz, J. Vorberger, M. Bethkenhagen, M. P. Böhme, D. M. Ceperley *et al.*, "Toward first principles-based simulations of dense hydrogen," Phys. Plasmas **31**, 110501 (2024).

[27] W. B. Hubbard, "Studies in stellar evolution. V. Transport coefficients of degenerate stellar matter," Astrophys. J. **146**, 858–870 (1966).

[28] E. Braun, "Transport coefficients in a plasma. I. Pure gas," Phys. Fluids **10**, 731–736 (1967).

[29] E. Flowers and N. Itoh, "Transport properties of dense matter," Astrophys. J. **206**, 218–242 (1976).

[30] H. Minoo, C. Deutsch, and J. P. Hansen, "Electronic transport in dense fully ionized hydrogen," Phys. Rev. A. **14**, 840–853 (1976).

[31] L. Spitzer and R. Härm, "Transport phenomena in a completely ionized gas," Phys. Rev. **89**, 977 (1953).

[32] J. M. Ziman, "A theory of the electrical properties of liquid metals. I: The monovalent metals," Philos. Mag. **6**, 1013 (1961).

[33] S. Ichimaru and S. Tanaka, "Theory of interparticle correlations in dense, high-temperature plasmas. V. Electric and thermal conductivities," Phys. Rev. A. **32**, 1790 (1985).

[34] G. Röpke and R. Redmer, "Electrical conductivity of nondegenerate, fully ionized plasmas," Phys. Rev. A. **39**, 907–910 (1989).

[35] G. Röpke, "Quantum-statistical approach to the electrical conductivity of dense, high-temperature plasmas," Phys. Rev. A. **38**, 3001–3016 (1988).

[36] H. Reinholz, G. Röpke, S. Rosmej, and R. Redmer, "Conductivity of warm dense matter including electron-electron collisions," Phys. Rev. E **91**, 043105 (2015).

[37] W. A. Stygar, G. A. Gerdin, and D. L. Fehl, "Analytic electrical-conductivity tensor of a nondegenerate Lorentz plasma," Phys. Rev. E **66**, 046417 (2002).

[38]V. E. Fortov, V. Y. Ternovoi, M. V. Zhernokletov, M. A. Mochalov, A. L. Mikhailov *et al.*, "Pressure-produced ionization of nonideal plasma in a megabar range of dynamic pressures," J. Exp. Theor. Phys. **97**, 259 (2003).
[39]L. J. Stanek, A. Kononov, S. B. Hansen, B. M. Haines, S. X. Hu *et al.*, "Review of the second charged-particle transport coefficient code comparison workshop," Phys. Plasmas **31**, 052104 (2024).
[40]Z. A. Johnson, L. G. Silvestri, G. M. Petrov, L. G. Stanton, and M. S. Murillo, "Comparison of transport models in dense plasmas," Phys. Plasmas **31**, 082701 (2024).
[41] Y. T. Lee and R. M. More, "An electron conductivity model for dense plasmas," Phys. Fluids **27**, 1273 (1984).
[42]L. D. Landau and E. M. Lifshitz, *Physical Kinetics: Course of Theoretical Physics* (Pergamon Press, Oxford, 1981), Vol. 10, pp. 177–181.
[43]H. A. Lorentz, "Le mouvement des électrons dans les métaux," Arch. Neerl. **10**, 336 (1905).
[44]M. P. Desjarlais, "Practical improvements to the Lee-More conductivity near the metal-insulator transition," Contrib. Plasma Phys. **41**, 267–270 (2001).
[45]P. Hohenberg and W. Kohn, "Inhomogeneous electron gas," Phys. Rev. **136**, B864 (1964).
[46]W. Kohn and L. J. Sham, "Self-consistent equations including exchange and correlation effects," Phys. Rev. **140**, A1133 (1965).
[47]N. D. Mermin, "Thermal properties of the inhomogeneous electron gas," Phys. Rev. **137**, A1441 (1965).
[48]G. Kresse and J. Furthmüller, "Efficient iterative schemes for *ab initio* total-energy calculations using a plane-wave basis set," Phys. Rev. B **54**, 11169 (1996).
[49]G. Kresse and J. Hafner, "*Ab initio* molecular dynamics for liquid metals," Phys. Rev. B **47**, 558 (1993).
[50]G. Kresse and J. Hafner, "*Ab initio* molecular-dynamics simulation of the liquid-metal–amorphous-semiconductor transition in germanium," Phys. Rev. B **49**, 14251 (1994).
[51] J. P. Perdew, K. Burke, and M. Ernzerhof, "Generalized gradient approximation made simple," Phys. Rev. Lett. **77**, 3865 (1996).
[52]P. E. Blöchl, "Projector augmented-wave method," Phys. Rev. B **50**, 17953 (1994).
[53]G. Kresse and D. Joubert, "From ultrasoft pseudopotentials to the projector augmented-wave method," Phys. Rev. B **59**, 1758 (1999).
[54]M. Valiev and J. H. Weare, "The projector-augmented plane wave method applied to molecular bonding," J. Phys. Chem. A **103**, 10588 (1999).
[55]A. Baldereschi, "Mean-value point in the Brillouin zone," Phys. Rev. B **7**, 5212 (1973).
[56]S. Nosé, "A unified formulation of the constant temperature molecular dynamics methods," J. Chem. Phys. **81**, 511 (1984).
[57]W. G. Hoover, "Canonical dynamics: Equilibrium phase-space distributions," Phys. Rev. A **31**, 1695 (1985).
[58]H. J. Monkhorst and J. D. Pack, "Special points for Brillouin-zone integrations," Phys. Rev. B **13**, 5188 (1976).
[59]M. Gajdoš, K. Hummer, G. Kresse, J. Furthmüller, and F. Bechstedt, "Linear optical properties in the projector-augmented wave methodology," Phys. Rev. B **73**, 045112 (2006).
[60]R. Kubo, "Statistical-mechanical theory of irreversible processes. I. General theory and simple applications to magnetic and conduction problems," J. Phys. Soc. Jpn. **12**, 570–586 (1957).
[61] D. A. Greenwood, "The Boltzmann equation in the theory of electrical conduction in metals," Proc. Phys. Soc. **71**, 585 (1958).
[62]W. W. Focke, "Correlating thermal-conductivity data for ternary liquid mixtures," Int. J. Thermophys. **29**, 1342–1360 (2008).
[63]M. P. Desjarlais, C. R. Scullard, L. X. Benedict, H. D. Whitley, and R. Redmer, "Density-functional calculations of transport properties in the nondegenerate limit and the role of electron-electron scattering," Phys. Rev. E **95**, 033203 (2017).
[64]G. Röpke, "Electrical conductivity of charged particle systems and Zubarev's nonequilibrium statistical operator method," Theor. Math. Phys. **194**, 74–104 (2018).
[65]D. O. Gericke, M. S. Murillo, and M. Schlanges, "Dense plasma temperature equilibration in the binary collision approximation," Phys. Rev. E **65**, 036418 (2002).
[66]W. Ebeling and W. Richert, "Thermodynamic functions of nonideal hydrogen plasmas," Ann. Phys. **494**, 362–370 (1982).
[67]D. Beule, W. Ebeling, A. Förster, H. Juranek, S. Nagel *et al.*, "Equation of state for hydrogen below 10000 K: From the fluid to the plasma," Phys. Rev. B **59**, 14177 (1999).
[68]M. Ross, "Matter under extreme conditions of temperature and pressure," Rep. Prog. Phys. **48**, 1–52 (1985).
[69]M. Ross, F. H. Ree, and D. A. Young, "The equation of state of molecular hydrogen at very high density," J. Chem. Phys. **79**, 1487–1494 (1983).
[70]H. Juranek, R. Redmer, and Y. Rosenfeld, "Fluid variational theory for pressure dissociation in dense hydrogen: Multicomponent reference system and nonadditivity effects," J. Chem. Phys. **117**, 1768 (2002).
[71] D. Saumon, G. Chabrier, and H. M. van Horn, "An equation of state for low-mass stars and giant planets," Astrophys. J., Suppl. Ser. **99**, 713 (1995).
[72]D. G. Hummer and D. Mihalas, "The equation of state for stellar envelopes. I. An occupation probability formalism for the truncation of internal partition functions," Astrophys. J. **331**, 794 (1988).
[73]D. Mihalas, W. Däppen, and D. G. Hummer, "The equation of state for stellar envelopes. II. Algorithm and selected results," Astrophys. J. **331**, 815 (1988).
[74]W. Däppen, D. Mihalas, D. G. Hummer, and B. W. Mihalas, "The equation of state for stellar envelopes. III. Thermodynamic quantities," Astrophys. J. **332**, 261 (1988).
[75]D. Mihalas, D. G. Hummer, B. W. Mihalas, and W. Däppen, "The equation of state for stellar envelopes. IV. Thermodynamic quantities and selected ionization fractions for six elemental mixes," Astrophys. J. **350**, 300 (1990).
[76]V. E. Fortov, R. I. Ilkaev, V. A. Arinin, V. V. Burtzev, V. A. Golubev *et al.*, "Phase transition in a strongly nonideal deuterium plasma generated by quasi-isentropical compression at megabar pressures," Phys. Rev. Lett. **99**, 185001 (2007).
[77]F. E. Höhne, R. Redmer, G. Röpke, and H. Wegener, "Linear response theory for thermoelectric transport coefficients of partially ionized plasma," Physica A **128**, 643–675 (1984).
[78]H. Reinholz, R. Redmer, and S. Nagel, "Thermodynamic and transport properties of dense hydrogen plasmas," Phys. Rev. E **52**, 5368–5386 (1995).
[79]J. R. Adams, N. S. Shilkin, V. E. Fortov, V. K. Gryaznov, V. B. Mintsev *et al.*, "Coulomb contribution to the direct current electrical conductivity of dense partially ionized plasmas," Phys. Plasmas **14**, 062303 (2007).
[80]K. Batygin, D. J. Stevenson, and P. H. Bodenheimer, "Evolution of ohmically heated hot Jupiters," Astrophys. J. **738**, 1 (2011).
[81] M. Bethkenhagen, B. B. L. Witte, M. Schörner, G. Röpke, T. Döppner *et al.*, "Carbon ionization at gigabar pressures: An *ab initio* perspective on astrophysical high-density plasmas," Phys. Rev. Res. **2**, 023260 (2020).
[82]M. Bethkenhagen, M. Schörner, and R. Redmer, "Insights on the electronic structure of high-density beryllium from *ab initio* simulations," Phys. Rev. Res. (submitted) (2024).
[83]J. Sun, A. Ruzsinszky, and J. P. Perdew, "Strongly constrained and appropriately normed semilocal density functional," Phys. Rev. Lett. **115**, 036402 (2015).
[84]J. Heyd, G. E. Scuseria, and M. Ernzerhof, "Hybrid functionals based on a screened Coulomb potential," J. Chem. Phys. **118**, 8207 (2003).
[85]F. Lambert, V. Recoules, A. Decoster, J. Clérouin, and M. Desjarlais, "On the transport coefficients of hydrogen in the inertial confinement fusion regime," Phys. Plasmas **18**, 056306 (2011).
[86]I. M. Bespalov and A. Ya. Polishchuk, *Methods of Calculation of Transport Coeffecients of Plasmas over a Wide Range of Parameters* ([in Russian], IVTAN Preprint No. 1-257, Institute of High Temperatures, Russian Academy of Sciences, Moscow, 1988).
[87]W. Ebeling, A. Förster, V. E. Fortov, V. K. Gryaznov, and A. Y. Polishchuk, in *Thermophysical Properties of Hot Dense Plasmas*, edited by W. Ebeling, W. Meiling, A. Uhlmann, and B. Wilhelmi (Teubner Verlagsgesellschaft, Stuttgart, 1991), p. 214.

[88]S. Cassisi, A. Y. Potekhin, A. Pietrinfernie, M. Catelan, and M. Salaris, "Updated electron-conduction opacities: The impact on low-mass stellar models," Astrophys. J. **661**, 1094–1104 (2007).
[89]S. Blouin, N. R. Shaffer, D. Saumon, and C. E. Starrett, "New conductive opacities for white dwarf envelopes," Astrophys. J. **899**, 46 (2020).
[90]S. T. Weir, A. C. Mitchell, and W. J. Nellis, "Metallization of fluid molecular hydrogen at 140 GPa (1.4 Mbar)," Phys. Rev. Lett. **76**, 1860 (1996).
[91] W. J. Nellis, S. T. Weir, and A. C. Mitchell, "Minimum metallic conductivity of fluid hydrogen at 140 GPa (1.4 Mbar)," Phys. Rev. B **59**, 3434 (1999).
[92]G. Röpke, M. Schörner, R. Redmer, and M. Bethkenhagen, "Virial expansion of the electrical conductivity of hydrogen plasmas," Phys. Rev. E **104**, 045204 (2021).
[93]V. Y. Ternovoi, A. S. Filimonov, V. E. Fortov, S. V. Kvitov, D. N. Nikolaev *et al.*, "Thermodynamic properties and electrical conductivity of hydrogen under multiple shock compression to 150 GPa," Physica B **265**, 6–11 (1999).
[94]P. A. Sterne, S. B. Hansen, B. G. Wilson, and W. A. Isaacs, "Equation of state, occupation probabilities and conductivities in the average atom Purgatorio code," High Energy Density Phys. **3**, 278–282 (2007).

Appendix

A Convergence

The accuracy of the simulation data in this work depends on several convergence parameters. In the case of transport properties, the most important one is the number of atoms in the simulation box. This convergence parameter can change drastically over a wide temperature-density range. In contrast, the other convergence parameters, like energy cutoff, time step, or broadening of the delta function in the LRT, are more or less stable over the whole range, besides some exceptions. This section shows the particle convergence for hcp iron and hydrogen.

A.1 Conductivity of iron

In the case of hcp iron, particle convergence is not as easy as, e.g., in fcc iron because the anisotropy in the structure requires different atom numbers along the axes to converge the results for the different components. To test this, we used different box continuations x:y:z, which result in N = 64 (2:2:2), 216 (3:3:3), 288 (3:3:4), 360 (3:3:5), and 384 (4:4:3) atoms in the box. The results for different density temperature conditions are shown in Fig. 14. The upper

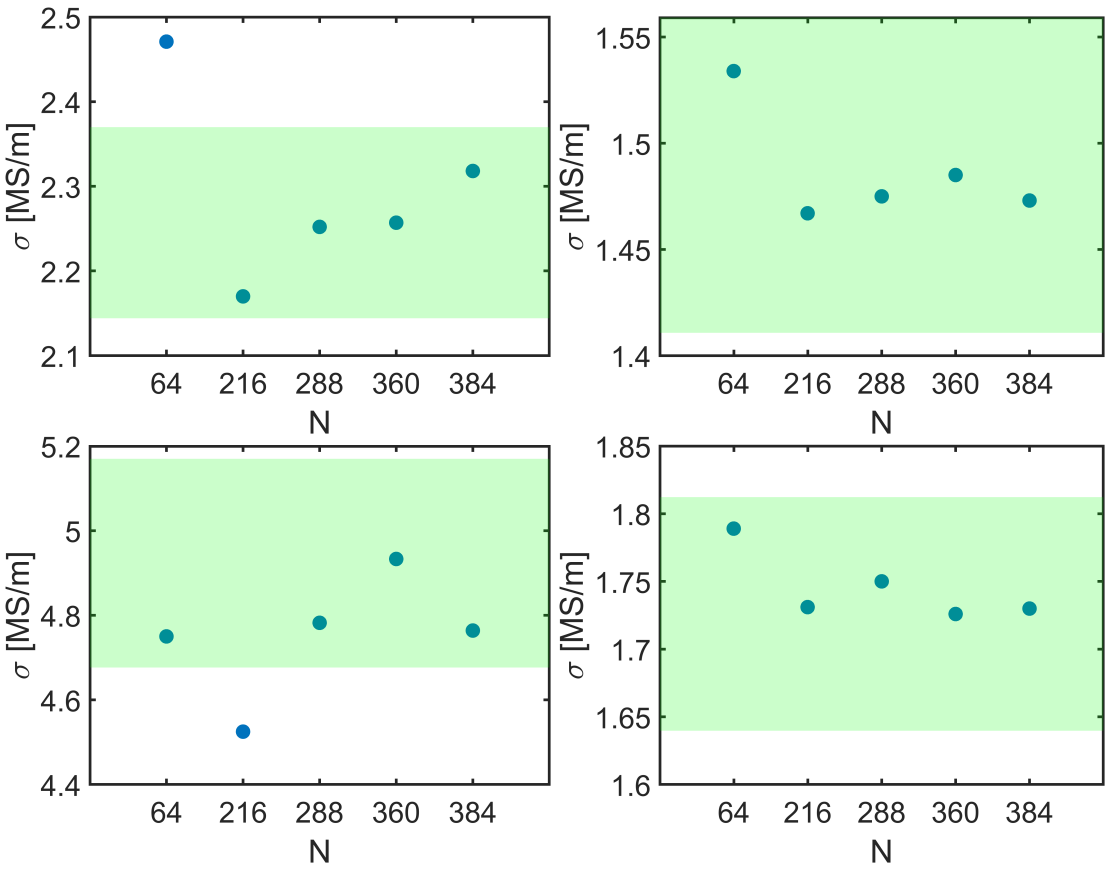

Figure 14: Electrical conductivity convergence in hexagonal iron. Upper left: ρ = 10.36 g/cm^3 and T = 1850 K; upper right: ρ = 10.36 g/cm^3 and T = 3350 K; lower left: ρ = 13.55 g/cm^3 and T = 1850 K; lower right: ρ = 13.55 g/cm^3 and T = 6350 K. The green area marks a 5 % difference from the N = 360 value.

graphs clearly show the effect of temperature. At 1850 K and 10.36 g/cm3, the conductivity is converged with 216 or 288 atoms in the box, while at 3350 K, even 64 atoms provide reasonable results, but at least 216 atoms are enough. The same effect can be seen in the lower graphs for 13.55 g/cm^3. The density effect is shown in the first column. The results for the higher density at 1850 K fluctuate strongly with the number of atoms, and a clear trend is not visible. A particle number of N = 288 is the minimum needed for good results, while smaller numbers of particles are enough for lower densities. In this work, the particle number N = 288 is chosen to get good results for all conditions.

A.2 Conductivity of hydrogen

The same trends can be seen for hydrogen as for iron. Temperature can drastically decrease the number of needed atoms in the box, and density has a strong effect at lower temperatures. For example, the results for 1 g/cm^3 and 2 g/cm^3 at 5000 K are shown in Fig. 15. For 1 g/cm3,

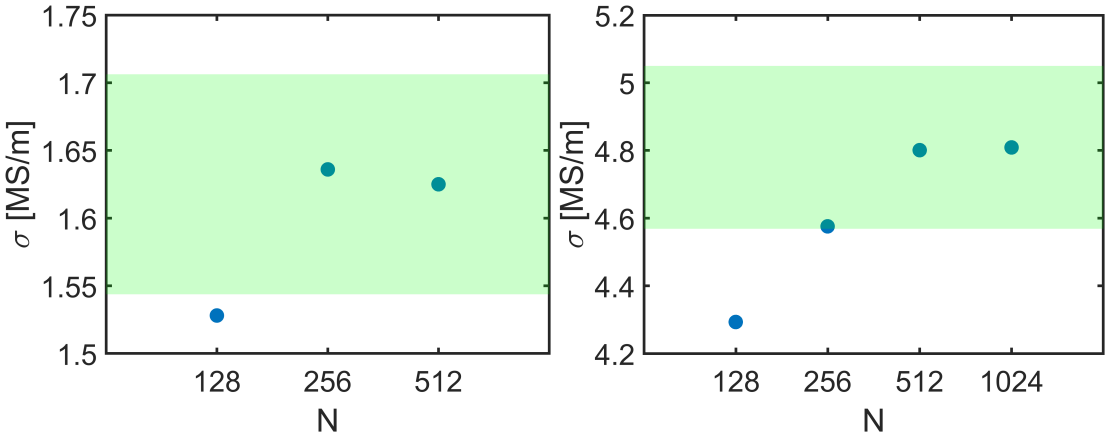

Figure 15: Electrical conductivity convergence in hydrogen. left: $\rho = 1$ g/cm^3 and $T = 5000$ K; right: $\rho = 2$ g/cm^3 and $T = 5000$ K. The green area marks a 5 % difference from the value of the highest particle number.

only 256 atoms are enough to converge the conductivity, while for 2 g/cm3, 512 atoms are needed. That means that by increasing the density by a factor of two, one needs to double the number of atoms in the box. However, this factor does not apply to all temperatures. The number of atoms decreases faster with temperature for high densities, which leads, e.g., to 256 atoms in the box at 10000 K.

B Conductivity model for high densities

The conductivity model discussed in Sec. 3.2 is based on DFT-MD data in the range of 0.1-8.0 g/cm^3. That means all results at conditions below or above this range are extrapolations from the model. As a test case, the results from the new conductivity model and the exact results from DFT-MD simulations for the electrical conductivity are shown in Fig. 16 for $\rho = 70$ g/cm^3 at $T = 17$ eV and $T = 86$ eV. First, the curves for the different atom numbers show that at least 512 atoms in the simulation box are needed to achieve good converged results. The two extrapolation methods shown here result in nearly the same DC values for the electrical conductivity. They show a slight deviation at low temperatures, but this is still in the

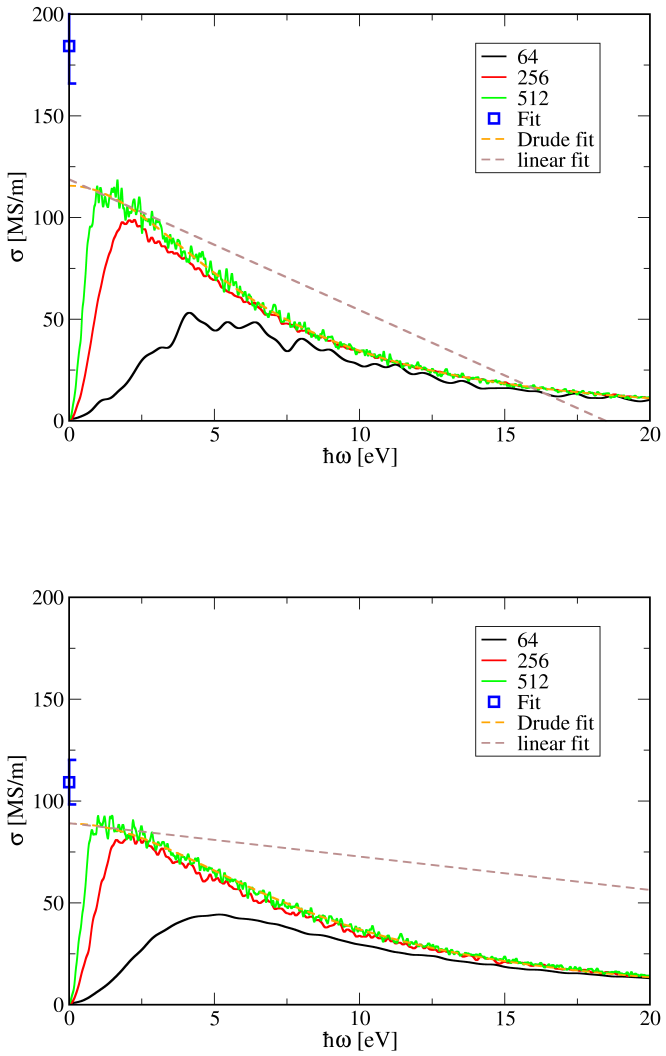

Figure 16: Dynamic electrical conductivity for dense hydrogen (ρ = 70 g/cm^3) for T = 17 eV (upper graph) and T = 86 eV (lower graph) for three different atom numbers (N = 64; 256; 512). Also shown are a Drude (orange dashed line)and linear fit (brown dashed line) for the low-frequency domain. The resulting DC conductivity from our model [179] is shown with a blue box and a 10 % error bar.

range of the uncertainty of the fits. The results for the DC conductivity provided by the new conductivity model are systematically larger than the DFT-MD data. Especially at lower temperatures, the deviation gets more vigorous, while at higher temperatures, the model nearly fits the simulation data again. These test simulations for ρ = 70 g/cm^3 show that the model deviates from the simulation at high densities and lower temperatures, which can explain the deviations shown in Fig. 10.

C Bibliography

References

[1] B. Militzer, F. González-Cataldo, S. Zhang, K. P. Driver, and F. Soubiran, "First-principles equation of state database for warm dense matter computation," *Phys. Rev. E*, vol. 103, p. 013203, Jan 2021.

[2] L. J. Stanek, A. Kononov, S. B. Hansen, B. M. Haines, S. X. Hu, P. F. Knapp, M. S. Murillo, L. G. Stanton, H. D. Whitley, S. D. Baalrud, L. J. Babati, A. D. Baczewski, M. Bethkenhagen, A. Blanchet, I. Clay, Raymond C., K. R. Cochrane, L. A. Collins, A. Dumi, G. Faussurier, M. French, Z. A. Johnson, V. V. Karasiev, S. Kumar, M. K. Lentz, C. A. Melton, K. A. Nichols, G. M. Petrov, V. Recoules, R. Redmer, G. Röpke, M. Schörner, N. R. Shaffer, V. Sharma, L. G. Silvestri, F. Soubiran, P. Suryanarayana, M. Tacu, J. P. Townsend, and A. J. White, "Review of the second charged-particle transport coefficient code comparison workshop," *Phys. Plasmas*, vol. 31, p. 052104, 05 2024.

[3] M. Bonitz, J. Vorberger, M. Bethkenhagen, M. Böhme, D. Ceperley, A. Filinov, T. Gawne, F. Graziani, G. Gregori, P. Hamann, S. Hansen, M. Holzmann, S. X. Hu, H. Kählert, V. Karasiev, U. Kleinschmidt, L. Kordts, C. Makait, B. Militzer, Z. Moldabekov, C. Pierleoni, M. Preising, K. Ramakrishna, R. Redmer, S. Schwalbe, P. Svensson, and T. Dornheim, "Towards first principles-based simulations of dense hydrogen," *Phys. Plasmas*, vol. 31, p. 110501, 2024.

[4] M. French, A. Becker, W. Lorenzen, N. Nettelmann, M. Bethkenhagen, J. Wicht, and R. Redmer, "Ab initio simulations for material properties along the Jupiter adiabat," *Astrophys. J. Suppl. Series*, vol. 202, p. 5, 2012.

[5] M. Preising, M. French, C. Mankovich, F. Soubiran, and R. Redmer, "Material Properties of Saturn's Interior from Ab Initio Simulations," *Astrophys. J. Suppl. Series*, vol. 269, p. 47, 2023.

[6] A. Becker, M. Bethkenhagen, C. Kellermann, J. Wicht, and R. Redmer, "Material properties for the interiors of massive giant planets and brown dwarfs," *Astron. J.*, vol. 156, p. 149, sep 2018.

[7] J. Xu, P. Zhang, K. Haule, J. Minar, S. Wimmer, H. Ebert, and R. E. Cohen, "Thermal Conductivity and Electrical Resistivity of Solid Iron at Earth's Core Conditions from First Principles," *Phys. Rev. Lett.*, vol. 121, p. 096601, 2018.

[8] B. Holst, M. French, and R. Redmer, "Electronic transport coefficients from ab initio simulations and application to dense liquid hydrogen," *Phys. Rev. B*, vol. 83, p. 235120, 2011.

[9] M. French and R. Redmer, "Electronic transport in partially ionized water plasmas," *Phys. Plasmas*, vol. 24, p. 092306, 2017.

[10] M. French, G. Röpke, M. Schörner, M. Bethkenhagen, M. P. Desjarlais, and R. Redmer, "Electronic transport coefficients from density functional theory across the plasma plane," *Phys. Rev. E*, vol. 105, p. 065204, 2022.

[11] C. E. Starrett, N. R. Shaffer, D. Saumon, R. Perriot, T. Nelson, L. A. Collins, and C. Ticknor, "Model for the electrical conductivity in dense plasma mixtures," *High Energ. Dens. Phys.*, vol. 36, p. 100752, 2020.

[12] J. M. McMahon, M. A. Morales, C. Pierleoni, and D. M. Ceperley, "The properties of hydrogen and helium under extrem conditions," *Rev. Mod. Phys.*, vol. 84, pp. 1607–1653, 2012.

[13] D. Durante, M. Parisi, D. Serra, M. Zannoni, V. Notaro, P. Racioppa, D. R. Buccino, G. Lari, L. Gomez Casajus, L. Iess, W. M. Folkner, G. Tommei, P. Tortora, and S. J. Bolton, "Jupiter's gravity field halfway through the Juno mission," *Geophys. Res. Lett.*, vol. 47, no. 4, p. e2019GL086572, 2020.

[14] A. P. Ingersoll, "Cassini Exploration of the Planet Saturn: A Comprehensive Review," *Space Sci. Rev.*, vol. 216, p. 122, 2020.

[15] J. E. P. Connerney, A. Adriani, F. Allegrini, F. Bagenal, S. J. Bolton, B. Bonfond, S. W. H. Cowley, J.-C. Gerard, G. R. Gladstone, D. Grodent, G. Hospodarsky, J. L. Jorgensen, W. S. Kurth, S. M. Levin, B. Mauk, D. J. McComas, A. Mura, C. Paranicas, E. J. Smith, R. M. Thorne, P. Valek, and J. Waite, "Jupiter's magnetosphere and aurorae observed by the Juno spacecraft during its first polar orbits," *Science*, vol. 356, no. 6340, pp. 826–832, 2017.

[16] Y. Kaspi, E. Galanti, A. P. Showman, D. J. Stevenson, T. Guillot, L. Iess, and S. J. Bolton, "Comparison of the Deep Atmospheric Dynamics of Jupiter and Saturn in Light of the Juno and Cassini Gravity Measurements," *Space Sci. Rev.*, vol. 216, p. 84, 2020.

[17] F. Bagenal, A. Adriani, F. Allegrini, S. Bolton, B. Bonfond, E. Bunce, J. Connerney, S. Cowley, R. Ebert, G. Gladstone, C. Hansen, W. Kurth, S. Levin, B. Mauk, D. McComas, C. Paranicas, D. Santos-Costa, R. Thorne, P. Valek, J. Waite, and P. Zarka, "Magnetospheric Science Objectives of the Juno Mission," *Space Sci. Rev.*, vol. 213, pp. 219–287, 2017.

[18] S. J. Bolton, A. Adriani, V. Adumitroaie, M. Allison, J. Anderson, S. Atreya, J. Bloxham, S. Brown, J. E. P. Connerney, E. DeJong, W. Folkner, D. Gautier, D. Grassi, S. Gulkis, T. Guillot, C. Hansen, W. B. Hubbard, L. Iess, A. Ingersoll, M. Janssen, J. Jorgensen, Y. Kaspi, S. M. Levin, C. Li, J. Lunine, Y. Miguel, A. Mura, G. Orton, T. Owen, M. Ravine, E. Smith, P. Steffes, E. Stone, D. Stevenson, R. Thorne, J. Waite, D. Durante, R. W. Ebert, T. K. Greathouse, V. Hue, M. Parisi, J. R. Szalay, and R. Wilson, "Jupiter's interior and deep atmosphere: The initial pole-to-pole passes with the Juno spacecraft," *Science*, vol. 356, no. 6340, pp. 821–825, 2017.

[19] S. M. Wahl, W. B. Hubbard, B. Militzer, T. Guillot, Y. Miguel, Y. Kaspi, R. Helled, D. Reese, E. Galanti, S. Levin, J. E. Connerney, and S. J. Bolton, "Comparing Jupiter

interior structure models to Juno gravity measurements and the role of a dilute core," *Geophys. Res. Lett.*, vol. 44, pp. 4649–4659, 2017.

[20] N. English, *Space Telescopes*. Springer Cham, 2017.

[21] J. P. Gardner, J. C. Mather, M. Clampin, R. Doyon, M. A. Greenhouse, H. B. Hammel, J. B. Hutchings, P. Jakobsen, S. J. Lilly, K. S. Long, J. I. Lunine, M. J. Mccaughrean, M. Mountain, J. Nella, G. H. Rieke, M. J. Rieke, H.-W. Rix, E. P. Smith, G. Sonneborn, M. Stiavelli, H. S. Stockman, R. A. Windhorst, and G. S. Wright, "The james webb space telescope," *Space Sci Rev*, vol. 123, pp. 485–606, 2006.

[22] J. P. Gardner, J. C. Mather, R. Abbott, *et al.*, "The james webb space telescope mission," *Publications of the Astronomical Society of the Pacific*, vol. 135, p. 068001, 2023.

[23] J. D. Landstreet, "The measurement of magnetic fields in stars," *Astronomical Journal*, vol. 85, pp. 611–620, 1980.

[24] G. Mathys, "Spectropolarimetry of magnetic stars. v. the mean quadratic magnetic field," *Astron. Astrophys.*, vol. 293, pp. 746–763, 1995.

[25] G. Schubert and K. M. Soderlund, "Planetary magnetic fields: Observations and models," *Phys. Earth Planet. Inter.*, vol. 187, p. 92, 2011.

[26] U. R. Christensen and J. Wicht, "Models of magnetic field generation in partly stable planetary cores: Applications to Mercury and Saturn," *Icarus*, vol. 196, p. 16, 2008.

[27] C. A. Jones, "A dynamo model of Jupiter's magnetic field," *Icarus*, vol. 241, pp. 148–159, 2014.

[28] J. Wicht and U. R. Christensen, "Contributions of Jupiter's deep-reaching surface winds to magnetic field structure and secular variation," *J. Geophys. Res. Planets*, vol. 129, p. e2023JE007890, 2024.

[29] C. Davies, M. Pozzo, D. Gubbins, and D. Alfè, "Constraints from material properties on the dynamics and evolution of Earth's core," *Nature Geosci.*, vol. 8, p. 678, 2015.

[30] H. Amit and P. Olson, "Lower mantle superplume growth excites geomagnetic reversals," *Earth Planet. Sci. Lett.*, vol. 414, p. 68, 2015.

[31] P. Cummins and L. R. Johnson, "Short-period body wave constraints on properties of the Earth's inner core boundary," *J. Geophys. Res.*, vol. 93, p. 9058, 1988.

[32] S. M. Tikoo and A. J. Evans, "Dynamos in the inner solar system," *Annu. Rev. Earth Planet. Sci.*, vol. 50, pp. 99–122, 2022.

[33] A. J. Roy, A. Bergermann, M. Bethkenhagen, and R. Redmer, "Mixture of hydrogen and methane under planetary interior conditions," *Phys. Chem. Chem. Phys.*, vol. 26, pp. 14374–14383, 2024.

[34] H. Gomi, K. Ohta, K. Hirose, *et al.*, "The high conductivity of iron and thermal evolution of the Earth's core," *Phys. Earth Planet. Inter.*, vol. 224, p. 88, 2013.

[35] Z. Konôpková, R. S. McWilliams, N. Gómez-Pérez, *et al.*, "Direct measurement of thermal conductivity in solid iron at planetary core conditions," *Nature*, vol. 534, p. 99, 2016.

[36] K. Ohta, Y. Kuwayama, K. Hirose, *et al.*, "Experimental determination of the electrical resistivity of iron at Earth's core conditions," *Nature*, vol. 534, p. 95, 2016.

[37] A. Hasegawa, T. Yagi, and K. Ohta, "Combination of pulsed light heating thermoreflectance and laser-heated diamond anvil cell for in-situ high pressure-temperature thermal diffusivity measurements ," *Rev. Sci. Instrum.*, vol. 90, p. 074901, 2019.

[38] A. Hasegawa, K. Ohta, T. Yagi, K. Hirose, and Y. Yamashita, "Inversion of the temperature dependence of thermal conductivity of hcp iron under high pressure," *Sci. Rep.*, vol. 14, p. 23582, 2024.

[39] N. de Koker, G. Steinle-Neumann, and V. Vlček, "Electrical resistivity and thermal conductivity of liquid Fe alloys at high P and T, and heat flux in Earth's core," *Natl. Acad. Sci.*, vol. 109, p. 4070, 2012.

[40] M. Pozzo, C. Davies, D. Gubbins, and D. Alfè, "Thermal and electrical conductivity of iron at Earth's core conditions," *Nature*, vol. 485, p. 355, 2012.

[41] M. Pozzo, C. Davies, D. Gubbins, and D. Alfè, "Thermal and electrical conductivity of solid iron and iron–silicon mixtures at Earth's core conditions," *Earth Planet. Sci. Lett.*, vol. 393, p. 159, 2014.

[42] M. Pozzo and D. Alfè, "Saturation of electrical resistivity of solid iron at Earth's core conditions," *SpringerPlus*, vol. 5, p. 256, 2016.

[43] F. Wagle and G. Steinle-Neumann, "Electrical resistivity discontinuity of iron along the melting curve," *Geophys. J. Int.*, vol. 213, p. 237, 2018.

[44] J. Korell, M. French, G. Steinle-Neumann, and R. Redmer, "Paramagnetic-to-Diamagnetic Transition in Dense Liquid Iron and Its Influence on Electronic Transport Properties," *Phys. Rev. Lett.*, vol. 122, p. 086601, 2019.

[45] W. McDonough and S. s. Sun, "The composition of the earth," *Chem. Geol.*, vol. 120, pp. 223–253, 1995.

[46] R. Trønnes, M. Baron, K. Eigenmann, M. Guren, B. Heyn, A. Løken, and C. Mohn, "Core formation, mantle differentiation and core-mantle interaction within earth and the terrestrial planets," *Tectonophysics*, vol. 760, pp. 165–198, 2019.

[47] N. Nettelmann, R. Püstow, and R. Redmer, "Saturn layered structure and homogeneous evolution models with different eoss," *Icarus*, vol. 225, pp. 548–557, 2013.

[48] R. Helled, N. Nettelmann, and T. Guillot, "Uranus and neptune: Origin, evolution and internal structure," *Space Sci. Rev.*, vol. 216, p. 38, 2020.

[49] Y. V. Ivanov, V. B. Mintsev, V. E. Fortov, and A. N. Dremin, "Electric conductivity of a non-ideal plasma," *Zh. Eksp. Teor. Fiz*, vol. 71, pp. 216–22, 1976.

[50] S. Ichimaru and S. Tanaka, "Theory of interparticle correlations in dense, high-temperature plasmas. 5. electric and thermal conductivities," *Phys. Rev. A*, vol. 32, p. 1790, 1985.

[51] Y. T. Lee and R. M. More, "An electron conductivity model for dense plasmas," *Phys. Fluids*, vol. 27, p. 1273, 1984.

[52] L. Spitzer and R. Härm, "Transport phenomena in a completely ionized gas," *Phys. Rev.*, vol. 89, p. 977, 1953.

[53] H. A. Lorentz, "Le mouvement des électrons dans les métaux," *Arch. Néerl.*, vol. 10, p. 336, 1905.

[54] M. P. Desjarlais, "Practical improvements to the lee-more conductivity near the metal-insulator transition," *Contrib. Plasma Phys.*, vol. 41, pp. 267–270, 2001.

[55] S. T. Weir, A. C. Mitchell, and W. J. Nellis, "Metallization of Fluid Molecular Hydrogen at 140 GPa (1.4 Mbar)," *Phys. Rev. Lett.*, vol. 76, p. 1860, 1996.

[56] W. J. Nellis, S. T. Weir, and A. C. Mitchell, "Minimum metallic conductivity of fluid hydrogen at 140 gpa (1.4 mbar)," *Phys. Rev. B*, vol. 59, p. 3434, 1999.

[57] G. Wiedemann and R. Franz, "Ueber die Wärme-Leitungsfähigkeit der Metalle," *Ann. Phys.*, vol. 165, p. 497, 1853.

[58] W. Ebeling, W. D. Kraeft, and D. Kremp, *Theory of Bound States and Ionization Equilibrium in Plasmas and Solids.* Akademie-Verlag, Berlin, 1976.

[59] W.-D. Kraeft, D. Kremp, W. Ebeling, and G. Röpke, *Quantum Statistics of Charged Particle Systems.* Akademie-Verlag, Berlin, 1986.

[60] D. Kremp, M. Schlanges, and W.-D. Kraeft, *Quantum Statistics of Nonideal Plasmas.* Springer, New York, 2005.

[61] R. Boehler, "High-pressure experiments and the phase diagram of lower mantle and core materials," *Rev. Geophys.*, vol. 38, p. 221, 2009.

[62] C. Cavazzoni, G. L. Chiarotti, S. Scandolo, E. Tosatti, M. Bernasconi, and M. Parrinello, "Superionic and metallic states of water and ammonia at giant planet conditions," *Science*, vol. 283, p. 44, 1999.

[63] R. Redmer, "Physical properties of dense, low-temperature plasmas," *Physics Reports*, vol. 282, pp. 35–158, 1997.

[64] A. Sommerfeld and H. Bethe, *Elektronentheorie der Metalle.* Berlin: Springer, 1967.

[65] S. Harris, *An Introduction to the Theory of the Boltzmann Equation.* Dover Books, 1971.

[66] S. Chapman and T. Cowling, *The Mathematical Theory of Non-Uniform Gases.* Cambridge University Press, Cambridge, 1971.

[67] J. M. Ziman, "A theory of the electrical properties of liquid metals. I: The monovalent metals," *Philos. Mag.*, vol. 6, p. 1013, 1961.

[68] V. Christoph and G. Röpke, "Theory of inverse linear response coefficients," *Phys. Status Solidi B*, vol. 131, p. 11, 1985.

[69] G. Röpke, "Quantum-statistical approach to the electrical conductivity of dense, high-temperature plasmas," *Phys. Rev. A*, vol. 38, pp. 3001–3016, 1988.

[70] R. Kubo, "Statistical-Mechanical Theory of Irreversible Processes. I. General Theory and Simple Applications to Magnetic and Conduction Problems," *J. Phys. Soc. Jap.*, vol. 12, pp. 570–586, 1957.

[71] D. Zubarev, V. Morozov, and G. Roöpke, *Statistical Mechanics of Nonequilibrium Processes.* Akademie-Verlag, Berlin, 1996. Band I.

[72] D. Zubarev, V. Morozov, and G. Röpke, *Statistical Mechanics of Nonequilibrium Processes.* Akademie-Verlag, Berlin, 1997. Band II.

[73] P. Hohenberg and W. Kohn, "Inhomogeneous electron gas," *Phys. Rev.*, vol. 136, p. B864, 1964.

[74] W. Kohn and L. J. Sham, "Self-consistent equations including exchange and correlation effects," *Phys. Rev.*, vol. 140, p. A1133, 1965.

[75] N. D. Mermin, "Thermal properties of the inhomogeneous electron gas," *Phys. Rev.*, vol. 137, p. A1441, 1965.

[76] J. Kohanoff, *Electronic structure calculations for solids and molecules: theory and computational methods.* Cambridge Univ. Press, 2006.

[77] W. Koch and M. C. Holthausen, *Front matter and index*, ch. A Chemist's Guide to Density Functional Theory. John Wiley & Sons, Ltd, 2001.

[78] B. J. Alder and T. E. Wainwright, "Phase transition for a hard sphere system," *J. Chem. Phys.*, vol. 27, p. 1208, 1957.

[79] B. J. Alder and T. E. Wainwright, "Studies in molecular dynamics. i. general method," *J. Chem. Phys.*, vol. 31, p. 459, 1959.

[80] D. M. Ceperley and B. J. Alder, "Ground state of the electron gas by a stochastic method," *Phys. Rev. Lett.*, vol. 45, pp. 566–569, 1980.

[81] T. Dornheim, S. Groth, and M. Bonitz, "The uniform electron gas at warm dense matter conditions," *Physics Reports*, vol. 744, pp. 1–86, 2018.

[82] S. Anzellini, *Phase diagram of iron under extreme conditions measured with time-resolved methods.* PhD thesis, Université Pierre et Marie Curie, 2014.

[83] D. Alfé, G. D. Pride, and M. J. Gillian, "Iron under earth's core conditions: Liquid-state thermodynamics and high-pressure melting curve from ab initio calculations," *Phys. Rev. B*, vol. 65, p. 165118, 2002.

[84] R. Boehler, "Temperatures in the earth's core from melting-point measurements of iron at high static pressures," *Nature*, vol. 363, p. 534, 1993.

[85] L. J. Swartzendruber, "The fe (iron) system," *Bull. Alloy Phase Diagrams*, vol. 3, p. 161, 1982.

[86] M. Ross, D. Young, and R. Grover, "Theory of the iron phase diagram at earth core conditions," *J. Geophys. Res.*, vol. 95, p. 21713, 1990.

[87] Y. Ma, M. Somayazulu, G. Shen, *et al.*, "In situ X-ray diffraction studies of iron to Earth-core conditions," *Phys. Earth Planet. Inter.*, vol. 143-144, p. 455, 2004.

[88] Y. Kuwayama, K. Hirose, N. Sata, and Y. Ohishi, "Phase relations of iron and iron–nickel alloys up to 300 gpa: Implications for composition and structure of the earth's inner core," *Earth Planet. Sci. Lett.*, vol. 273, p. 379, 2008.

[89] T. Komabayashi, Y. Fei, Y. Meng, and V. Prakapuka, "In-situ X-ray diffraction measurements of the γ-ϵ transition boundary of iron in an internally-heated diamond anvil cell," *Earth Planet. Sci. Lett.*, vol. 282, p. 252, 2009.

[90] S. Tateno, K. Hirose, Y. Ohishi, and Y. Tatsumi, "The structure of iron in earth's inner core," *Science*, vol. 330, p. 359, 2010.

[91] A. B. Belonoshko, T. Lukinov, J. Z. J. Fu, S. Davis, and S. I. Simak, "Stabilization of body-centred cubic iron under inner-core conditions," *Nat. Geosci.*, vol. 10, p. 312, 2017.

[92] A. Jayaraman, "Diamond anvil cell and high-pressure physical investigations," *Rev. Mod. Phys.*, vol. 55, pp. 65–108, Jan 1983.

[93] S. Anzellini and S. Boccato, "A practical review of the laser-heated diamond anvil cell for university laboratories and synchrotron applications," *Crystals*, vol. 10, no. 6, 2020.

[94] E. Gregoryanz, C. Ji, P. Dalladay-Simpson, B. Li, R. T. Howie, and H.-K. Mao, "Everything you always wanted to know about metallic hydrogen but were afraid to ask," *Matter Radiat. Extremes*, vol. 5, p. 038101, 2020.

[95] P. Dalladay-Simpson, R. Howie, and E. Gregoryanzv, "Evidence for a new phase of dense hydrogen above 325 gigapascals," *Nature*, vol. 529, pp. 63–67, 2016.

[96] R. T. Howie, C. L. Guillaume, T. Scheler, A. F. Goncharov, and E. Gregoryanz, "Mixed molecular and atomic phase of dense hydrogen," *Phys. Rev. Lett.*, vol. 108, p. 125501, 2012.

[97] R. T. Howie, T. Scheler, C. L. Guillaume, and E. Gregoryanz, "Proton tunneling in phase iv of hydrogen and deuterium," *Phys. Rev. B*, vol. 86, p. 214104, 2012.

[98] R. Howie, P. Dalladay-Simpson, and E. Gregoryanz, "Raman spectroscopy of hot hydrogen above 200 gpa," *Nature Mater*, vol. 14, p. 495–499, 2015.

[99] X.-D. Liu, R. T. Howie, H.-C. Zhang, X.-J. Chen, and E. Gregoryanz, "High-pressure behavior of hydrogen and deuterium at low temperatures," *Phys. Rev. Lett.*, vol. 119, p. 065301, 2017.

[100] M. D. Knudson, M. P. Desjarlais, A. Becker, R. W. Lemke, K. R. Cochrane, M. E. Savage, D. E. Bliss, T. R. Mattsson, and R. Redmer, "Direct observation of an abrupt insulator-to-metal transition in dense liquid deuterium," *Science*, vol. 348, pp. 1455–1460, 2015.

[101] P. M. Celliers, M. Millot, S. Brygoo, R. S. McWilliams, D. E. Fratanduono, J. R. Rygg, A. F. Goncharov, P. Loubeyre, J. H. Eggert, J. L. Peterson, N. B. Meezan, S. L. Pape, G. W. Collins, R. Jeanloz, and R. J. Hemley, "Insulator-metal transition in dense fluid deuterium," *Science*, vol. 361, pp. 677–682, 2018.

[102] A. Bergermann, L. Kleindienst, and R. Redmer, "Nonmetal-to-metal transition in liquid hydrogen using density functional theory and the heyd–scuseria–ernzerhof exchange-correlation functional," *J. Chem. Phys.*, vol. 161, p. 234303, 2024.

[103] G. Röpke, R. Redmer, M. Schörner, H. Reinholz, U. Kleinschmidt, and M. Bethkenhagen, "Electron-electron collisions in calculations of the electrical conductivity for warm dense matter based on density functional theory," *Phys. Rev. E*, vol. 111, p. 055201, 2025.

[104] E. Schrödinger, "Quantisierung als eigenwertproblem (erste mitteilung)," *Ann. Phys.*, vol. 79, p. 361, 1926.

[105] E. Schrödinger, "Quantisierung als eigenwertproblem (zweite mitteilung)," *Ann. Phys.*, vol. 79, p. 489, 1926.

[106] E. Schrödinger, "Quantisierung als eigenwertproblem (dritte mitteilung)," *Ann. Phys.*, vol. 80, p. 437, 1926.

[107] E. Schrödinger, "Quantisierung als eigenwertproblem (vierte mitteilung)," *Ann. Phys.*, vol. 81, p. 109, 1926.

[108] B. Hammond, W. Lester, and P. Reynolds, *Monte Carlo Methods in Ab Initio Quantum Chemistry*. Singapore: World Scientific, 1994.

[109] C. J. Nightingale, M.P.; Umrigar, *Quantum Monte Carlo Methods in Physics and Chemistry*. Springer, 1999.

[110] A. Szabo and N. Ostlund, *Modern Quantum Chemistry: Introduction to Advanced Electronic Structure Theory*. Dover Publicazions, 1996.

[111] M. Born and R. Oppenheimer, "Zur quantentheorie der molekeln," *Ann. Phys. (Leipzig)*, vol. 389, no. 20, pp. 457–484, 1927.

[112] W. Kohn, "Nobel lecture: Electronic structure of matter—wave functions and density functionals," *Rev. Mod. Phys.*, vol. 71, pp. 1253–1266, Oct 1999.

[113] R. G. Parr and W. Yang, *Density-Functional Theory of Atoms and Molecules*. Oxford University Press, 1989.

[114] R. G. Parr, "Density functional theory," *Annual Review of Physical Chemistry*, vol. 34, no. Volume 34, 1983, pp. 631–656, 1983.

[115] R. O. Jones, "Density functional theory: Its origins, rise to prominence, and future," *Rev. Mod. Phys.*, vol. 87, pp. 897–923, Aug 2015.

[116] R. Martin, *Electronic structure: basic theory and practical methods*. Cambridge Univ. Press, 2004.

[117] A. D. Becke, "Perspective: Fifty years of density-functional theory in chemical physics," *The Journal of Chemical Physics*, vol. 140, p. 18A301, 04 2014.

[118] R. M. Dreizler and E. K. U. Gross, *Density functional theory : an approach to the quantum many-body problem*. Springer, 1990.

[119] A. E. Mattsson, P. A. Schultz, M. P. Desjarlais, T. R. Mattsson, and K. Leung, "Designing meaningful density functional theory calculations in materials science—a primer," *Modelling and Simulation in Materials Science and Engineering*, vol. 13, p. R1, nov 2004.

[120] R. O. Jones and O. Gunnarsson, "The density functional formalism, its applications and prospects," *Rev. Mod. Phys.*, vol. 61, pp. 689–746, Jul 1989.

[121] E. S. Kryachko and E. V. Ludeña, "Density functional theory: Foundations reviewed," *Physics Reports*, vol. 544, no. 2, pp. 123–239, 2014. Density functional theory: Foundations reviewed.

[122] J. P. Perdew, K. Burke, and M. Ernzerhof, "Generalized gradient approximation made simple," *Phys. Rev. Lett.*, vol. 77, p. 3865, 1996.

[123] J. Sun, A. Ruzsinszky, and J. P. Perdew, "Strongly constrained and appropriately normed semilocal density functional," *Phys. Rev. Lett.*, vol. 115, p. 036402, Jul 2015.

[124] J. Heyd, G. E. Scuseria, and M. Ernzerhof, "Hybrid functionals based on a screened Coulomb potential," *J. Chem. Phys.*, vol. 118, p. 8207, 2003.

[125] V. V. Karasiev, T. Sjostrom, J. Dufty, and S. B. Trickey, "Accurate homogeneous electron gas exchange-correlation free energy for local spin-density calculations," *Phys. Rev. Lett.*, vol. 112, p. 076403, 2014.

[126] V. V. Karasiev, J. Dufty, and S. B. Trickey, "Nonempirical semilocal free-energy density functional for matter under extreme conditions," *Phys. Rev. Lett.*, vol. 120, p. 076401, 2018.

[127] V. V. Karasiev, D. I. Mihalov, and S. X. Hu, "Meta-gga exchange-correlation free energy density functional to increase the accuracy of warm dense matter simulations," *Phys. Rev. B*, vol. 105, p. L081109, 2022.

[128] A. Pribram-Jones, P. E. Grabowski, and K. Burke, "Thermal density functional theory: Time-dependent linear response and approximate functionals from the fluctuation-dissipation theorem," *Phys. Rev. Lett.*, vol. 116, p. 233001, 2016.

[129] D. I. Mihaylov, V. V. Karasiev, and S. X. Hu, "Thermal hybrid exchange-correlation density functional for improving the description of warm dense matter," *Phys. Rev. B*, vol. 101, p. 245141, 2020.

[130] J. P. Perdew, A. Ruzsinszky, J. Tao, V. N. Staroverov, G. E. Scuseria, and G. I. Csonka, "Prescription for the design and selection of density functional approximations: More constraint satisfaction with fewer fits," *The Journal of Chemical Physics*, vol. 123, p. 062201, 2005.

[131] J. Heyd and G. E. Scuseria, "Assessment and validation of a screened coulomb hybrid density functional," *The Journal of Chemical Physics*, vol. 120, pp. 7274–7280, 2004.

[132] A. V. Krukau, O. A. Vydrov, A. F. Izmaylov, and G. E. Scuseria, "Influence of the exchange screening parameter on the performance of screened hybrid functionals," *The Journal of Chemical Physics*, vol. 125, p. 224106, 2006.

[133] C. Cozza, K. Nakano, S. Howard, H. Xie, R. Helled, and G. Mazzola, "A denser hydrogen inferred from first-principles simulations challenges jupiter's interior models," *arXiv:2501.12925 [astro-ph.EP]*, 2025.

[134] V. Blum, R. Gehrke, F. Hanke, P. Havu, V. Havu, X. Ren, K. Reuter, and M. Scheffler, "Ab initio molecular simulations with numeric atom-centered orbitals," *Computer Physics Communications*, vol. 180, no. 11, pp. 2175–2196, 2009.

[135] J. M. Soler, E. Artacho, J. D. Gale, A. García, J. Junquera, P. Ordejón, and D. Sánchez-Portal, "The siesta method for ab initio order-n materials simulation," *Journal of Physics: Condensed Matter*, vol. 14, p. 2745, mar 2002.

[136] P. Giannozzi, S. Baroni, N. Bonini, M. Calandra, R. Car, C. Cavazzoni, D. Ceresoli, G. L. Chiarotti, M. Cococcioni, I. Dabo, A. Dal Corso, S. de Gironcoli, S. Fabris, G. Fratesi, R. Gebauer, U. Gerstmann, C. Gougoussis, A. Kokalj, M. Lazzeri, L. Martin-Samos, N. Marzari, F. Mauri, R. Mazzarello, S. Paolini, A. Pasquarello, L. Paulatto, C. Sbraccia, S. Scandolo, G. Sclauzero, A. P. Seitsonen, A. Smogunov, P. Umari, and R. M. Wentzcovitch, "Quantum espresso: a modular and open-source software project for quantum simulations of materials," *Journal of Physics: Condensed Matter*, vol. 21, p. 395502, sep 2009.

[137] M. D. Segall, P. J. D. Lindan, M. J. Probert, C. J. Pickard, P. J. Hasnip, S. J. Clark, and M. C. Payne, "First-principles simulation: ideas, illustrations and the castep code," *Journal of Physics: Condensed Matter*, vol. 14, p. 2717, mar 2002.

[138] G. Kresse and J. Furthmüller, "Efficient iterative schemes for ab initio total-energy calculations using a plane-wave basis set," *Phys. Rev. B*, vol. 54, p. 11169, 1996.

[139] G. Kresse and J. Hafner, "Ab initio molecular dynamics for liquid metals," *Phys. Rev. B*, vol. 47, p. 558, 1993.

[140] G. Kresse and J. Hafner, "Ab initio molecular-dynamics simulation of the liquid-metal–amorphous-semiconductor transition in germanium," *Phys. Rev. B*, vol. 49, p. 14251, 1994.

[141] X. Gonze, J.-M. Beuken, R. Caracas, F. Detraux, M. Fuchs, G.-M. Rignanese, L. Sindic, M. Verstraete, G. Zerah, F. Jollet, M. Torrent, A. Roy, M. Mikami, P. Ghosez, J.-Y. Raty, and D. Allan, "First-principles computation of material properties: the abinit software project," *Computational Materials Science*, vol. 25, no. 3, pp. 478–492, 2002.

[142] F. Bloch, "Über die quantenmechanik der elektronen in kristallgittern," *Z. Phys.*, vol. 52, p. 555, 1929.

[143] D. Marx and J. Hutter, *Ab initio molecular dynamics: basi theory and advanced methods.* Cambridge Univ. Press Cambridge, 2009.

[144] R. A. Evarestov and V. P. Smirnov, "Special points of the brillouin zone and their use in the solid state theory," *Phys. Status Solidi B*, vol. 119, p. 9, 1983.

[145] A. Baldereschi, "Mean-value point in the brillouin zone," *Phys. Rev. B*, vol. 7, p. 5252, 1973.

[146] H. J. Monkhorst and J. D. Pack, "Special points for brillouin-zone integrations," *Phys. Rev. B*, vol. 13, p. 5188, 1976.

[147] B. Holst, M. French, and R. Redmer, "Electronic transport coefficients from ab initio simulations and application to dense liquid hydrogen," *Phys. Rev. B.*, vol. 83, p. 235120, 2011.

[148] M. French and T. R. Mattsson, "Thermoelectric transport properties of molybdenum from *ab initio* simulations," *Phys. Rev. B*, vol. 90, p. 165113, 2014.

[149] G. Kresse and D. Joubert, "From ultrasoft pseudopotentials to the projector augmented-wave method," *Phys. Rev. B*, vol. 59, p. 1758, 1999.

[150] P. E. Blöchl, "Projector augmented-wave method," *Phys. Rev. B*, vol. 50, p. 17953, 1994.

[151] M. Valiev and J. H. Weare, "The projector-augmented plane wave method applied to molecular bonding," *J. Phys. Chem. A*, vol. 103, p. 10588, 1999.

[152] D. Frenkel and B. Smit, *Understanding Molecular Simulation (Second Edition).* Academic Press, 2002.

[153] M. P. Allen and D. J. Tildesley, *Coputer Simulations of Liquids.* Oxford Science Publications, 1987.

[154] D. Rapaport, *The Art of Molecular Dynamics Simulation.* Cambridge Univ. Press, 2004.

[155] H. Hellmann, *Einführung in die Quantenchemie.* Deuticke, Leipzig, 1937.

[156] R. P. Feynman, "Forces in molecules," *Phys. Rev.*, vol. 56, p. 340, 1939.

[157] S. Nosé, "A unified formulation of the constant temperature molecular dynamics methods," *J. Chem. Phys.*, vol. 81, p. 511, 1984.

[158] W. G. Hoover, "Canonical dynamics: Equilibrium phase-space distributions," *Phys. Rev. A.*, vol. 31, p. 1695, 1985.

[159] W. Lorenzen, *Phase Transitions in Hydrogen-Helium Mixtures*. PhD thesis, University of Rostock, 2012.

[160] D. J. Henderson and C. T. Rettner, "Physical chemistry," in *Encyclopedia of Physical Science and Technology (Third Edition)* (R. A. Meyers, ed.), pp. 159–176, New York: Academic Press, third edition ed., 2003.

[161] G. Röpke and R. Redmer, "Electrical conductivity of nondegenerate, fully ionized plasmas," *Phys. Rev. A*, vol. 39, pp. 907–910, Jan 1989.

[162] H. Reinholz, R. Redmer, and S. Nagel, "Thermodynamic and transport properties of dense hydrogen plasma.," *Phys. Rev. E*, vol. 52, pp. 5368–5386, 1995.

[163] L. Spitzer and R. Härm, "Transport Phenomena in a Completely Ionized Gas," *Phys. Rev.*, vol. 89, pp. 977–981, 1953.

[164] H. Reinholz, G. Röpke, S. Rosmej, and R. Redmer, "Conductivity of warm dense matter including electron-electron collisions," *Phys. Rev. E*, vol. 91, p. 043105, Apr 2015.

[165] D. A. Greenwood, "The Boltzmann Equation in the Theory of Electrical Conduction in Metals," *Proc. Phys. Soc.*, vol. 71, p. 585, 1958.

[166] M. Gajdoš, K. Hummer, G. Kresse, J. Furthmüller, and F. Bechstedt, "Linear optical properties in the projector-augmented wave methodology," *Phys. Rev. B*, vol. 73, p. 045112, 2006.

[167] M. French, *Ab-initio-Berechnung von Transporteigenschaften von warmer dichter Materie*. habilitation, Universität Rostock, 2021.

[168] G. Röpke, "Electrical conductivity of charged particle systems and Zubarev's nonequilibrium statistical operator method," *Theor. Math. Phys.*, vol. 194, pp. 74–104, 2018.

[169] W. Ebeling, V. E. Fortov, Y. L. Klimontovich, N. P. Kovalenko, W. D. Kraeft, Y. P. Krasny, D. Kremp, P. P. Kulik, V. A. Riaby, E. K. R. G. Röpke, and M. Schlanges, *Transport Properties of Dense Plasmas*. Akademie-Verlag, Berlin, 1984.

[170] N. W. Ashcroft and N. D. Mermin, *Solid State Physics*. Holt, Rinehart and Winston, New York, 1976.

[171] W. W. Focke, "Correlating thermal-conductivity data for ternary liquid mixtures," *Int. J. Thermophys.*, vol. 29, pp. 1342–1360, 2008.

[172] M. P. Desjarlais, C. R. Scullard, L. X. Benedict, H. D. Whitley, and R. Redmer, "Density-functional calculations of transport properties in the nondegenerate limit and the role of electron-electron scattering," *Phys. Rev. E*, vol. 95, p. 033203, 2017.

[173] M. Schöttler, R. Redmer, and M. French, "Low-density equation of state for water from a chemical model," *Contributions to Plasma Physics*, vol. 53, pp. 336–346, 2013.

[174] R. K. Pathria and P. D. Beale, *Statistical Mechanics, Third Edition*. Academic, Boston, 2011.

[175] M. N. Saha, "Liii. ionization in the solar chromosphere," *The London, Edinburgh, and Dublin Philosophical Magazine and Journal of Science*, vol. 40, p. 472, 1920.

[176] M. N. Saha, "On a physical theory of stellar spectra," *Proc. R. Soc. Lond. A*, vol. 99, p. 135, 1921.

[177] S. Kumar, A. J. Poser, M. Schöttler, U. Kleinschmidt, W. Dietrich, J. Wicht, M. French, and R. Redmer, "Ionization and transport in partially ionized multicomponent plasmas: Application to atmospheres of hot Jupiters," *Phys. Rev. E*, vol. 103, p. 063203, 2021.

[178] U. Kleinschmidt, M. French, G. Steinle-Neumann, and R. Redmer, "Electrical and thermal conductivity of fcc and hcp iron under conditions of the earth's core from ab initio simulations," *Phys. Rev. B*, vol. 107, p. 085145, 2023.

[179] U. Kleinschmidt and R. Redmer, "A conductivity model for hydrogen based on *ab initio* simulations," *Matter Radiat. Extremes*, vol. 10, p. 047602, 2025.

[180] K. Ohta, Y. Nishihara, Y. Sato, K. Hirose, *et al.*, "An Experimental Examination of Thermal Conductivity Anisotropy in hcp Iron," *Front. Earth Sci.*, vol. 6, p. 176, 2018.

[181] P. Saha, A. Mazumder, and G. D. Mukherjee, "Thermal conductivity of dense hcp iron: Direct measurements using laser heated diamond anvil cell," *Geosci. Front.*, vol. 11, p. 1755, 2020.

[182] D. Alfè, M. Pozzo, and M. P. Desjarlais, "Lattice electrical resistivity of magnetic bcc iron from first-principles calculations," *Phys. Rev. B*, vol. 85, p. 024102, 2012.

[183] A. B. Belonoshko, "Equation of state for ϵ-iron at high pressures and temperatures," *Condens. Matter Phys.*, vol. 13, p. 23605, 2010.

[184] Y. Zhang, M. Hou, G. Liu, *et al.*, "Reconciliation of Experiments and Theory on Transport Properties of Iron and the Geodynamo," *Phys. Rev. Lett.*, vol. 125, p. 078501, 2020.

[185] S. S. Lobanov and Z. M. Geballe, "Non-isotropic contraction and expansion of samples in diamond anvil cells: Implications for thermal conductivity at the core-mantle boundary," *Geophys. Res. Lett.*, vol. 49, p. e2022GL100379, 2022.

[186] T. Guillot, L. N. Fletcher, R. Helled, M. Ikoma, M. R. Line, and V. Parmentier, "Giant planets from the inside-out," 2022.

[187] S. X. Hu, B. Militzer, V. N. Goncharov, and S. Skupsky, "First-principles equation-of-state table of deuterium for inertial confinement fusion applications," *Phys. Rev. B*, vol. 84, p. 224109, Dec 2011.

[188] A. Zylstra, O. Hurricane, D. Callahan, and other, "Burning plasma achieved in inertial fusion," *Nature*, vol. 601, pp. 542–548, 2022.

[189] F. Lambert, V. Recoules, A. Decoster, J. Clérouin, and M. Desjarlais, "On the transport coefficients of hydrogen in the inertial confinement fusion regime," *Phys. Plasmas*, vol. 18, p. 056306, 2011.

[190] G. Röpke, M. Schörner, R. Redmer, and M. Bethkenhagen, "Virial expansion of the electrical conductivity of hydrogen plasmas," *Phys. Rev. E*, vol. 104, p. 045204, 2021.

[191] P. Sterne, S. Hansen, B. Wilson, and W. Isaacs, "Equation of state, occupation probabilities and conductivities in the average atom Purgatorio code," *High Energy Dens. Phys.*, vol. 3, no. 1, pp. 278–282, 2007.

[192] W. Dietrich, S. Kumar, A. J. Poser, M. French, N. Nettelmann, R. Redmer, and J. Wicht, "Magnetic induction processes in hot Jupiters, application to KELT-9b," *Monthly Notices of the Royal Astronomical Society*, vol. 517, p. 3113, 2022.

[193] P. Wulff, U. R. Christensen, W. Dietrich, and J. Wicht, "The effects of a stably stratified region with radially varying electrical conductivity on the formation of zonal winds on gas planets," *J. Geophys. Res. Planets*, vol. 129, p. e2023JE008042, 2024.

[194] D. Charbonneau, T. M. Brown, D. W. Latham, and M. Mayor, "Detection of planetary transits across a sun-like star," *Astrophys. J.*, vol. 529, p. L45, 2000.

[195] A. J. Poser, N. Nettelmann, and R. Redmer, "The effect of clouds as an additional opacity source on the inferred metallicity of giant exoplanets," *Atmosphere*, vol. 10, p. 664, 2019.

[196] T. Guillot, "On the radiative equilibrium of irradiated planetary atmospheres," *Astron. Astrophys. J.*, vol. 520, p. A27, 2010.

[197] M. R. Line, K. B. Stevenson, J. Bean, J.-M. D. nd J. J. Fortney, L. Kreidberg, N. Madhusuhan, A. P. Showman, and H. Diamond-Lowe, "No thermal inversion and a solar water abundance for the hot jupiter hd 209458b from hst/wfc3 spectroscopy," *Astrophys. J.*, vol. 152, p. 203, 2016.

[198] D. S. Spiegel, K.Silverio, and A. Burrows, "Can tio explain thermal inversions in the upper atmospheres of irradiated giant planets?," *Astrophys. J.*, vol. 699, p. 1487, 2009.

[199] D. Thorngren and J. J. Fortney, "Connecting giant planet atmosphere and interior modeling: Constraints on atmospheric metal enrichment," *The Astrophysical Journal Letters*, vol. 874, p. L31, 2019.

D Curriculum vitae

Geboren am 25.09.1997 in Anklam

Studium/Forschung

seit 10/2021	Promotionsstudium an der Universität Rostock
10/2021	Master of Science in Physik Masterarbeit: *Berechnung der Leitfähigkeit von festem Eisen unter Erdkernbedingungen mit Ab-initio-Rechnungen* in der Gruppe von Prof. Dr. Ronald Redmer Note: 1,6
2019 - 2021	Studium im Studiengang Physik (Master) an der Universität Rostock
09/2019	Bachelor of Science in Physik Bachelorarbeit: *Berechnung der Leitfähigkeit von partiell ionisierten H-He-Metall-Plasmen* in der Gruppe von Prof. Dr. Ronald Redmer Note: 1,9
2016 - 2019	Studium im Studiengang Physik (Bachelor) an der Universität Rostock

Schulbildung

07/2016	Abitur, Note: 1,0
2010 - 2016	Besuch des “Greifen-Gymnasiums”, Ueckermünde
2008 - 2010	Besuch der "Regionalen Schule Ernst Thälmann”, Eggsin
2004 - 2008	Besuch der “Grundschule”, Eggsin

Lehre an der Universität Rostock

SS 2022 - SS 2025	Betreuung des Versuchs *Density Functional Theory Molecular Dynamics Simulations for Carbon* im Rahmen des physikalischen Forschungspraktikums (später: Advanced Research Laboratory)
WS 2021/22 - WS 2024/25	Betreuung des Seminars zur Vorlesung Astronomie und Astrophysik: Sterne, Galaxien, Universum
SS 2024	Betreuung des Seminars zur Vorlesung Statische Physik
WS 2023/24	Betreuung des Seminars zur Vorlesung Thermodynamik
WS 2022/23	Betreuung von Versuchen im Rahmen des physikalischen Praktikums

Liste der Veröffentlichungen

- G. Röpke, R. Redmer, M. Schörner, H. Reinholz, U. Kleinschmidt und M. Bethkenhagen,
  Electron-electron collisions in calculations of the electrical conductivity for warm dense matter based on density functional theory
  Phys. Rev. E **111**, 055201 (2025)

- U. Kleinschmidt und R. Redmer,
  A conductivity model for hydrogen based on ab initio simulations
  Matter Radiat. Extremes **10**, 047602 (2025)

- M. Bonitz, J. Vorberger, M. Bethkenhagen, M. Böhme, D. Ceperley, A. Filinov, T. Gawne, F. Graziani, G. Gregori, P. Hamann, S. Hansen, M. Holzmann, S. X. Hu, H. Kählert, V. Karasiev, U. Kleinschmidt, L. Kordts, C. Makait, B. Militzer, Z. Moldabekov, C. Pierleoni, M. Preising, K. Ramakrishna, R. Redmer, S. Schwalbe, P. Svensson und T. Dornheim,
  Towards first principles-based simulations of dense hydrogen
  Phys. Plasmas **31**, 110501 (2024)

- U. Kleinschmidt, M. French, G. Steinle-Neumann und R. Redmer,
  Electrical and thermal conductivity of fcc and hcp iron under conditions of the earth's core from ab initio simulations
  Phys. Rev. B **107**, 085145 (2023)

- S. Kumar, A. J. Poser, M. Schöttler, U. Kleinschmidt, W. Dietrich, J. Wicht, M. French und R. Redmer,
  Ionization and transport in partially ionized multicomponent plasmas: Ap- plication to atmospheres of hot Jupiters
  Phys. Rev. E **103**, 063203 (2021)

Liste der Fachvorträge

- **A conductivity model for hydrogen based on ab initio simulations**, 45th International Workshop on High Energy Density Physics with Intense Ion and Laser Beams, Hirschegg (AUT) (2025)
- **Improved Conductivity model for fully and partially ionized hydrogen plasma**, 18th International Conference on the Physics of Non-Ideal Plasmas, Oxford (GB) (2024)
- **Improved conductivity model for fully ionized hydrogen plasma**, 87. Jahrestagung der DPG und DPG-Frühjahrstagung, Greifswald (GER) (2024)
- **Electrical and thermal conductivity of iron at Earth's core conditions from ab initio simulations**, 11th Joint Workshop on High Pressure, Planetary and Plasma Physics (HP4), Rostock (GER) (2023)
- **Electrical and thermal conductivity of iron at Earth's core conditions from ab initio simulations**, 28th AIRAPT (International Association for the Advancement of High Pressure Science and Technology) and 60th EHPRG (European High Pressure Research Group), Edinburgh (GB) (2023)
- **Electrical and thermal conductivity of iron at Earth's core conditions from ab initio simulations**, Workshop on transport properties at high pressure, Edinburgh (GB) (2023)
- **Electrical and thermal conductivity of fcc and hcp iron under conditions of the Earth's core from ab initio simulations**, 10th Joint Workshop on High Pressure, Planetary and Plasma Physics (HP4), Brüssel (BEL) (2022)

Liste der Posterpräsentationen

- Matter in Extreme Conditions from MATerial science to PLAnetary physics (MECMATPLA), Montgenèvre (FRA) (2024)
- Workshop: DFT Methods for Matter under Extreme Conditions, Görlitz (GER) (2022)

Danksagung

An dieser Stelle möchte ich mich bei allen Menschen bedanken, die mich während meiner Zeit in der Promotion begleitet haben. Mein besonderer Dank geht an meinen Betreuer Prof. Dr. Ronald Redmer, der mir die Möglichkeit gegeben hat, mich in dieses spannende Wissenschaftsfeld einzuarbeiten und mich dabei immer sehr gut unterstützt hat. Des Weiteren möchte ich mich bei ihm für das tolle Arbeitsklima und das immer freundliche Miteinander, auch außerhalb des Arbeitsplatzes, bedanken. Ein weiterer Dank geht speziell an Martin French, der mich schon während meiner Bachelor- und Masterarbeit betreute und einen großen Anteil an meiner Entwicklung in der Wissenschaft hat. Weiterhin bedanke ich mich bei allen aktuellen und ehemaligen Kollegen aus meiner Arbeitsgruppe, die immer ein offenes Ohr bei Problemen im wissenschaftlichen oder persönlichen Bereich hatten und durch ihre freundliche Art dafür gesorgt haben, dass ich mich jederzeit wohl bei der Arbeit gefühlt habe.
Diese Arbeit wäre niemals ohne die Bereitstellung von großer Rechenleistung möglich gewesen. Daher geht mein Dank an die Administratoren der Cluster Titan und Haumea des ITMZ und des HLRN-Verbunds.
Mein letzter Dank geht an meine Freundin, Familie und Freunde. Ohne den Rückhalt aus dem persönlichen Umfeld wäre es für mich nur schwer möglich gewesen, jeden Tag mit voller Kraft in Richtung der Promotion zu arbeiten.

Selbstständigkeitserklärung

Ich versichere hiermit an Eides statt, dass ich die vorliegende Arbeit selbstständig angefertigt und ohne fremde Hilfe verfasst habe. Dazu habe ich keine außer den von mir angegebenen Hilfsmitteln und Quellen verwendet und die den benutzten Werken inhaltlich und wörtlich entnommenen Stellen habe ich als solche kenntlich gemacht.

Rostock

(Abgabedatum)	(Vollständige Unterschrift)